

THE MICROSECOND PULSED GLOW DISCHARGE:
DEVELOPMENTS IN TIME-OF-FLIGHT MASS SPECTROMETRY
AND ATOMIC EMISSION SPECTROMETRY

By

ERIC OXLEY

A DISSERTATION PRESENTED TO THE GRADUATE SCHOOL
OF THE UNIVERSITY OF FLORIDA IN PARTIAL FULFILLMENT
OF THE REQUIREMENTS FOR THE DEGREE OF
DOCTOR OF PHILOSOPHY

UNIVERSITY OF FLORIDA

2002

Dedicated to my parents, Betty & Larry, and Paige, my love.

ACKNOWLEDGMENTS

Many individuals have contributed to the work in this dissertation. They have been not only scientific colleagues, but also good friends. First, I wish to thank my advisor, Dr. W.W. Harrison, for his continued guidance and support. His compassion and leadership have helped me grow as a scientist and as a person. Fortunately, his cynical sense of humor has made these years of growth very enjoyable.

I am also grateful that I could work closely with Dr. Jim Winefordner and his research group. Special recognition is given to Dr. Benjamin Smith, senior scientist. Dr. Winefordner and Dr. Smith always had an open door for my relentless questions, and were very important to my research progression. I would also like to thank my mentor, Dr. Chenglong Yang, for his help during my early days in the laboratory. Mike Herlevich and Dr. David Myers, who directly contributed to many of my research efforts, also deserve special recognition. I also thank Dr. Fred King, my undergraduate research advisor, who supported my early research endeavors at West Virginia University and who is responsible for my pursuit of graduate research.

I would like to extend appreciation to all members of the Harrison and Winefordner groups whom I have had the privilege to meet. Dr. Kristofor Ingeneri and Dr. Matthew Mohill, my predecessors in the Harrison group, deserve special recognition. I also mention my close friends, Nathan Pixley and Dimitri Pappas, who provided an endless source of amusement in the laboratory.

I would like to mention two visiting scientists, Dr. Arne Bengtson and Dr. Volker Hoffmann, for their helpful discussions and insightful suggestions.

A special word of gratitude goes to my family. I would certainly not be the person that I am today without the continued love and support of my parents, Betty and Larry. I have been blessed with their compassion throughout life's endeavors, and for this I am indebted forever. I owe special thanks to my love, Paige, for bestowing her incessant love and support. I honor all three of you with this dissertation.

This research has been supported by LECO Corporation and the United States Department of Energy, Basic Energy Sciences.

TABLE OF CONTENTS

	<u>page</u>
ACKNOWLEDGEMENTS.....	iii
ABSTRACT.....	ix
CHAPTERS	
1 INTRODUCTION.....	1
Introduction.....	1
Solid Sample Elemental Analysis.....	4
Glow Discharge.....	6
The Pulsed Glow Discharge.....	7
Dissertation Scope.....	10
2 THE GLOW DISCHARGE.....	13
Introduction.....	13
General Discharge Characteristics.....	14
Glow Discharge Spatial Regions.....	17
Cathode Dark Space.....	19
Negative Glow.....	21
Faraday Dark Space.....	23
Glow Discharge Processes.....	23
Cathodic Sputtering.....	23
Sputtering process.....	25
Sputter rate.....	27
Sputter yield.....	28
Collisional Phenomena.....	29
Electron behavior.....	30
Sputtered species excitation and ionization.....	30
Excitation.....	31
Ionization.....	34
3 GLOW DISCHARGE MODES.....	36
Introduction.....	36
Source Configurations.....	36
Hollow Cathode Geometry.....	37
Diode (Coaxial) Geometry.....	39
Grimm Geometry.....	42
Operational Modes.....	45
Direct Current.....	45

Radio Frequency.....	48
Pulsed.....	50
Microsecond Pulsed Glow Discharge Advantages.....	52
Additional Control Parameters.....	52
Enhanced Sputtering Rates.....	53
Enhanced Ionization and Emission.....	54
Temporal Resolution.....	54
Pulsed Glow Discharge Spectroscopies.....	55
Atomic Fluorescence/Absorption Spectrometry.....	57
Atomic Emission Spectrometry.....	57
Time-of-Flight Mass Spectrometry.....	59
 4 QUANTITATIVE DEPTH ANALYSIS USING MICROSECOND PULSED GLOW DISCHARGE ATOMIC EMISSION SPECTROMETRY.....	 64
Introduction.....	64
Experimental.....	65
Instrumentation.....	65
Sample Material.....	68
Sputter rate protocol.....	68
Additional samples.....	69
Results and Discussion.....	70
Optimization of Conditions.....	70
Effect of voltage and pressure.....	71
Effect of pulse width and pulse frequency.....	75
Effect of sputtering time.....	75
Sputtering Rates and Penetration Rates.....	78
Calibration Curve Correction.....	82
Quantification Overview.....	84
Principle of Quantification.....	88
Concluding Remarks.....	96
 5 INTRODUCTION TO THE GRIMM-TYPE GLOW DISCHARGE AXIAL TIME-OF-FLIGHT MASS SPECTROMETER SYSTEM.....	 97
Introduction.....	97
Time-of-Flight Mass Spectrometry Background.....	98
Operating Characteristics.....	98
Basic Principles.....	99
Design Considerations.....	104
Sampling geometry.....	104
Ion optics.....	104
Detector.....	105
The Grimm-type glow discharge source and Renaissance time- of-flight mass spectrometer.....	107
Grimm-type Glow Discharge Source.....	108

Source description.....	108
Source operation.....	111
Renaissance Time-of-Flight Mass Spectrometer.....	112
Mass spectrometer description.....	112
Mass spectrometer modifications.....	115
Overall Operation.....	116
Performance of the Glow Discharge Time-of-Flight Mass Spectrometer.....	116
Ion Detection.....	120
Sensitivity.....	122
Resolving Power.....	124
Linear Dynamic Range.....	124
Isotopic Accuracy.....	127
Signal-to-Noise Considerations.....	127
 6 ION TRANSPORT DIAGNOSTICS IN A MICROSECOND PULSED GRIMM-TYPE GLOW DISCHARGE TIME-OF-FLIGHT MASS SPECTROMETER.....	 131
Introduction.....	131
Experimental.....	133
Glow Discharge Source and Time-of-Flight Mass Spectrometer.....	133
Sample Material.....	133
Results and Discussion.....	134
Background.....	134
Parametric Study.....	135
Gas flow rate.....	135
Pressure.....	139
Other operating parameters.....	142
Source Design.....	142
Initial source design.....	142
Gas directing sleeve design.....	149
Sampler/Sleeve combination design.....	153
Application of Temporal Resolution.....	156
Concluding Remarks.....	161
 7 DIRECT PIN SAMPLE ANALYSIS USING A CONVENTIONAL GRIMM- TYPE GLOW DISCHARGE SOURCE AND TIME-OF-FLIGHT MASS SPECTROMETER.....	 162
Introduction.....	162
Experimental.....	166
Glow Discharge Source and Time-of-Flight Mass Spectrometer.....	166
Pin Sample Holder.....	166
Sample Material.....	169
Results and Discussion.....	170
Sample Holder Design.....	170

Source/Plasma Configuration.....	170
Sputtering Rate Comparison.....	171
Matrix Ion Signal.....	174
Detection Limit and Isotope Ratios.....	177
Molecular Interferences.....	179
Temporal Resolution.....	186
Pin Length.....	189
Pin Sample Application.....	191
Concluding Remarks.....	197
 8 THIN FILM ANALYSIS WITH A MICROSECOND PULSED GLOW DISCHARGE TIME-OF-FLIGHT MASS SPECTROMETER.....	 198
Introduction.....	198
Experimental.....	200
Glow Discharge Source and Time-of-Flight Mass Spectrometer.....	200
Sample Material.....	201
Results and Discussion.....	202
Sample Fabrication.....	202
Gold Thickness.....	202
Scanning electron microscope.....	202
Weight measurements.....	204
Parametric Studies.....	206
Pulse voltage.....	206
Source pressure.....	208
Pulse frequency.....	210
Pulse width.....	211
Thickness Limit.....	211
Calibration Curve.....	216
Quantitative Conversion.....	216
Simultaneous Mass Spectra Collection.....	218
Multiple Sample Layers.....	222
Additional Application.....	226
Concluding Remarks.....	227
 9 CONCLUDING REMARKS.....	 229
 REFERENCES.....	 233
 BIOGRAPHICAL SKETCH.....	 242

Abstract of Dissertation Presented to the Graduate School
of the University of Florida in Partial Fulfillment of the
Requirements for the Degree of Doctor of Philosophy

THE MICROSECOND PULSED GLOW DISCHARGE:
DEVELOPMENTS IN TIME-OF-FLIGHT MASS SPECTROMETRY
AND ATOMIC EMISSION SPECTROMETRY

By

Eric Oxley

August 2002

Chair: Willard W. Harrison
Major Department: Chemistry

The focus of this dissertation is the study of the microsecond pulsed glow discharge (GD) source through developments with time-of-flight mass spectrometry (TOFMS) and atomic emission spectroscopy (AES). The GD is an electrical plasma long known for its ability to convert solid samples directly into the atomic state for subsequent analysis. Applying a transient pulse to a GD source provides exciting new features and applications that can be evaluated. The microsecond pulsed GD shows great potential as an ion source for mass spectrometry (MS) and as a photon source for atomic emission (AE) measurements. New directions for these atomic techniques have been evaluated and will be described throughout this dissertation.

After successfully completing a microsecond pulsed GD-AES depth profiling project, research efforts were shifted to MS studies. The conversion of a commercial inductively coupled plasma (ICP) time-of-flight mass spectrometer to a GD-TOFMS system is described. A Grimm-type GD ion source was chosen, which has found limited use for mass spectrometric applications, despite its effectiveness as an AE source. The sluggish development of the Grimm-source for mass spectrometry is attributed to its inherent ion transport complexity. The performance of this GD-TOFMS, including ion transport efficiency, is reported.

A limitation of the Grimm configuration is its lack of versatility - only flat samples that can mount externally on the source are possible. Non-flat samples, such as pins and wires, require a probe-type configuration. A sample holder has been developed that allows pin sample analysis directly on a Grimm-type source. Easy sample interchange and reproducible sample placement - inherent advantages of the Grimm source - are conserved with this sample holder.

Depth profiling is an important feature of GD-AES studies, but has not been considered a practical application for GDMS. The feasibility of Grimm GD-TOFMS depth profiling is determined by establishing operating conditions that simultaneously afford sufficient ion transport and well-defined craters. This was achieved by merging our established ion transport conditions with operating parameters yielding good depth resolution. Samples consisting of very thin layers, as well as multi-layered samples, were analyzed with our GD-TOFMS.

CHAPTER 1 INTRODUCTION

Introduction

Mass spectrometry is an analytical technique in which gaseous ions are separated based on their mass-to-charge ratios. The versatility of this technique makes it one of the most widely applicable tools available to an analytical chemist. Indeed, mass spectrometry has significantly evolved since its initial development by Aston¹ and Dempster,² who made the first measurements of ionic masses and abundances. These experiments followed developments by Thomson, who demonstrated the existence of elemental isotopes by measuring intense streams of particles, which he termed positive rays.³ These pioneering endeavors in mass spectrometry gave impetus to probe the isotopic composition of many types of samples. Resulting mass spectra displayed only single lines at characteristic mass-to-charge (m/z) values, which proved less complex than convoluted atomic emission spectra. The analysis of petroleum-based samples was a driving force of mass spectrometry at this time, and the spectral simplicity of isotopic spectra gave reason to actively pursue mass spectrometry research - eventually resulting in the eventual fabrication of the sophisticated mass spectrometers that are available today.

Many types of mass spectrometers have evolved from the pioneering experiments by Thomson. Present day mass spectrometers can be separated

based on their means of mass selection: dispersion, filtration, and trapping. Sector-based mass spectrometers,^{4,5} which were developed from Aston's prototype instrument,¹ employ an electromagnetic and electrostatic field to disperse different mass-to-charge ions spatially. Today, these devices have evolved into high-resolution, yet expensive, devices. Quadrupole mass spectrometers^{6,7} use a band-pass principle to select ions of a particular mass window, and have made tandem mass spectrometry experiments possible.⁸ Ion trap mass spectrometers^{9,10} selectively store ions prior to their measurement. Ion cyclotron mass spectrometers,^{11,12} which also utilize a trapping mechanism to store ions, have achieved ultra-high resolution measurements. Finally, time-of-flight mass spectrometers,^{13,14} which are based on a dispersion-in-time phenomenon, have developed into a leading form of mass spectrometry due to (1) the soaring popularity of biological mass spectrometry research and (2) improvements in the speed and quality of electronic devices.

Improving these mass spectrometric devices has coincided with the development of sophisticated ion sources. The current popularity in biological mass spectrometry has shifted attention from atomic ionization sources to sources capable of producing intact molecular species. Two of the most popular molecular-based ion sources include electrospray injection (ESI)¹⁵ and matrix-assisted laser desorption mass spectrometry (MALDI).¹⁶ These ion sources are generally credited with bringing mass spectrometry to the forefront of analytical research.

Developing ion sources that are capable of producing atomic species is certainly also important for analytical measurements, particularly mass spectrometric research. These sources provide a wealth of information about samples, including elemental quantitation, ionic speciation, isotopic composition, and spatial distribution.¹⁷ Samples exist in a wide variety of types (i.e., matrices), complicating the choice of an appropriate atomic ionization source. Ion sources, particularly those capable of analyzing solid samples, have been plagued by problems that arise with the production of atomic vapor from solid samples. However, solid sample analysis is crucial for many divisions of science, including geological and environmental studies, which is why sample introduction methods continue to be at the forefront of spectrochemical research.

Solid samples can be treated in several ways prior to analysis by mass spectrometry. Some ionization sources, such as the inductively coupled plasma (ICP),¹⁸ require sample digestion and extraction prior to analysis. Indeed, these added steps can be tedious and time-consuming. Since sample turnaround time is of prime importance for many production laboratories, this added step can be a concern. Sample digestion is typically accomplished through dissolution in an acidic solution, which dilutes the concentration of the analyte and can result in the introduction of contaminants. Surface chemistry studies are also negated with dissolution steps since the sample is physically converted to aqueous form.

Solid Sample Elemental Analysis

Despite a wealth of sample preparation methods available, the ability to directly analyze solid samples is a substantial advantage since contamination and dilution concerns are avoided. Some examples of atomic ionization sources that can directly analyze solid samples include secondary ion bombardment, laser ablation, and plasma-based processes. All of these are capable of converting solid samples into gaseous ions for subsequent analysis by mass spectrometry; however, all of them suffer from inherent limitations.

Secondary ion mass spectrometry (SIMS) utilizes a beam of ions to analyze sample surfaces, such as metals, alloys, and semiconductors.¹⁹ Primary ions, such as argon and cesium ions, are generated by an electron impact ion gun and then accelerated to the sample surface at approximately 5 - 20 keV. The collision of these ions with the sample surface leads to sample removal through a phenomenon termed sputtering. While the sputtered sample material is primarily composed of sample atoms, only a small portion (~1%) of the ejected sample material is in ionic form (i.e., secondary ions). SIMS is capable of probing lateral and depth resolution of the sample surface and is characterized by high sensitivities; however, matrix effects and sensitivity variations are common limitations.²⁰

Laser ablation techniques, such as laser induced breakdown spectroscopy (LIBS), utilize a laser beam focused onto a sample surface to ablate material for subsequent analysis.^{21,22} The impinging laser energy, usually originating from an excimer or pulsed Nd:Yag laser, is transferred to the sample surface, resulting in

the ejection of molecules, atoms, and ions. While laser ablation is a versatile technique capable of analyzing conductive and insulating materials with little sample preparation, this technique suffers from poor precision and severe interference effects.

Laser-based sources have also been coupled to inductively coupled plasma mass spectrometers (ICPMS) to eliminate dissolution steps required for solid sample ICP analysis.^{23,24} In laser ablation inductively coupled plasma mass spectrometry (LA-ICPMS), the sample material is ablated from the sample surface and transported to the ICP plasma and subsequently analyzed. The use of LA-ICPMS allows sample introduction and sample ionization steps to be optimized independently, affording better control of the analysis. While this independent control can be an advantage, it can also contribute to the poor accuracy and precision of the technique.²⁵ Future research in sample transport efficiency and sample ionization may help resolve these problems.

Another means of converting solid samples into gaseous ions for mass spectrometry is the use of plasma sources. Spark sources were among the first plasma-type sources coupled to mass spectrometry.²⁶ This source converts solid samples into atomic constituents by applying a high-potential (~30 kV) between two electrodes that are typically fabricated from the sample material. A repetitive high current discharge forms on the sample surface and electron bombardment releases sample material for subsequent mass spectral analysis. Spark sources are highly sensitive, yet erratic sampling devices. This erratic behavior hinders the precision of the source, and renders it unable to perform depth-profiling of the

sample surface. Also, a spark produces a large kinetic energy distribution of ions, which can be difficult to focus in mass spectrometry applications.

Glow Discharge

Another plasma-based technique capable of directly producing atomic species from solid samples is the glow discharge (GD). The desire to develop better means of solid elemental analysis by mass spectrometry has resulted in a growing interest in glow discharge research. This versatile source lends itself to a range of analytical possibilities, including bulk metal and alloy analysis, depth-resolved analysis, and non-conductive sample analysis. While GD devices have many inherent advantages, stability and reproducibility are considered their best attribute compared to other competitive sources.²⁷

Also adding to the versatility of the GD is its ability to produce representative atomic populations of the sample, as well as excited state and ionic populations of those atoms. Since Coburn and colleagues demonstrated the analytical utility of the GD source in 1970s,^{28,29} this versatile source has seen application in atomic emission spectrometry (GD-AES),^{30,31} atomic absorption spectrometry (GD-AAS),^{32,33} atomic fluorescence spectrometry (GD-AFS),^{34,35} and mass spectrometry (GDMS).^{36,37}

A glow discharge plasma is formed when a sufficiently high voltage is applied between two electrodes that are immersed in a gaseous environment, such as argon. Typically, the cell is arranged so that high voltage is applied directly to the sample (cathode), while the anode is held at ground potential. The

potential difference between the two electrodes causes breakdown of the argon atoms (Ar^0), forming argon ions (Ar^+) and free electrons (e^-). Acceleration of the argon ions toward the sample surface leads to sputter removal of surface atoms (M^0). A simple glow discharge, along with characteristic phenomena of this device, is represented in Figure 1-1.

The Pulsed Glow Discharge

Although most glow discharge devices are operated in a continuous, direct current (dc) mode, aspects of operating a GD in a pulsed mode have been examined.³⁸ Supplying a pulsed voltage to the sample material generates "packets" of sample atoms that expand as they diffuse across the cell with each pulse, as shown in Figure 1-2. Advantages are obtained when this transient pulse is applied to a GD, such as enhanced sputtering, excitation, and ionization; fewer problems with thermal effects; and temporal discrimination of analytical signals through gated detection.

One method of operating a glow discharge is to operate it in the microsecond-pulsed regime. In this mode, a voltage up to 3.0 kV can be applied to the sample for approximately 10 to 20 microseconds at a frequency between 100 and 1000 Hz. The highly energetic plasma formed during the application of this transient, high voltage yields more excited and ionized sample atoms than are produced by a dc source. Signal increases from 10- to 100-fold have been reported using the pulsed mode of operation.³⁸

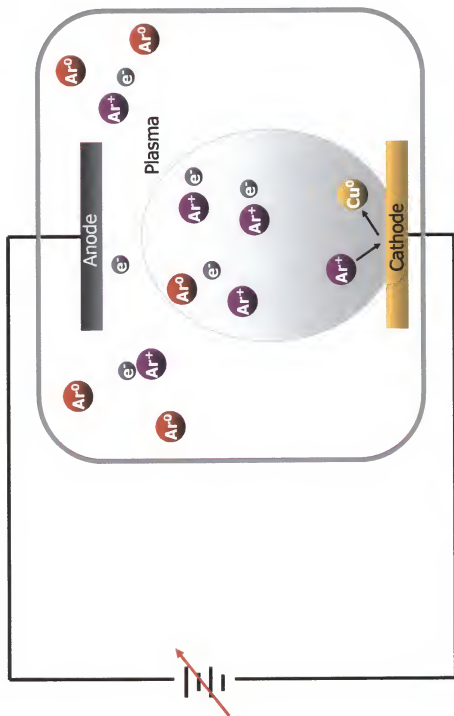


Figure 1-1. Simple glow discharge device.

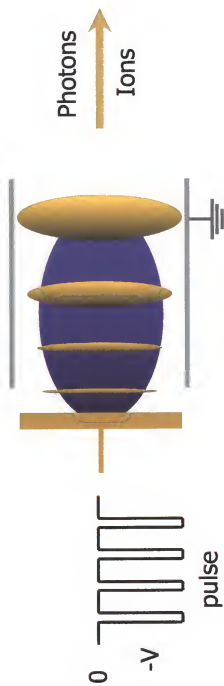


Figure 1-2. Pulsed glow discharge producing 'pulse packets' of sample material.

Dissertation Scope

The research endeavors described in this dissertation focus on developments of the microsecond pulsed glow discharge source. This research encompasses experiments in both glow discharge atomic emission spectrometry (GD-AES) and glow discharge mass spectrometry (GDMS). Fundamental studies, such as ion transport diagnostics, as well as applications, such as depth profiling, of the microsecond pulsed GD source are shown. This work is separated in five distinct, yet related, sections.

The first project undertaken was an evaluation of the microsecond pulsed GD source for performing depth profiling measurements. This experiment was performed on a commercial atomic emission spectrometer (SA-2000 Surface Analyzer, LECO Corporation, St. Joseph, MI, USA), which was modified for our pulsed GD work. The pulsed mode of operation afforded the analysis of thin sample layers that are difficult to examine using a dc source. Optimal conditions of the glow discharge source, including voltage, pressure, pulse width, and pulse frequency were utilized. The analysis of thin coatings of varying depths of copper deposited on a steel substrate is shown.

After successful completion of the AES depth profiling project, research efforts shifted to microsecond pulsed glow discharge mass spectrometry studies. The conversion of a commercial inductively coupled plasma (ICP) time-of-flight mass spectrometer (TOFMS) to a GD-TOFMS system is described. A Grimm-type GD source was designed and coupled to the modified TOFMS. The software was also modified for pulsed-source compatibility, allowing the

instrument to trigger the power supply and synchronize timing events between the mass spectrometer and the glow discharge source. This new GD-TOFMS system was evaluated, and its figures of merit, such as mass resolving power, are shown.

The next project describes a fundamental study employing the GD-TOFMS system. Ion transport from the source to the mass spectrometer, an inherent limitation of a Grimm source and mass spectrometer combination, was evaluated. Fundamental studies of ion transport are described, and methods of improving this transfer are shown. Some operating conditions of the source were found to significantly alter the efficiency of the transfer step. The configuration of the Grimm-type source was also a significant factor in maximizing ion transport. An example shown in this dissertation is the ability to identify trace amounts of magnesium from background ions using an optimized source configuration.

After establishing conditions that yield sufficient ion transport, applications of the GD-TOFMS were evaluated. A limitation of the Grimm configuration is its lack of versatility – only flat samples that can mount externally on the source are possible. Non-flat samples, such as pins and wires, typically require a probe-type configuration. A sample holder has been designed that allows pin sample analysis directly on a Grimm-type source. Easy sample interchange and reproducible sample placement - inherent advantages of the Grimm source - are conserved with this sample holder. An evaluation of this sample holder for pin sample analysis is shown.

The final project undertaken was a depth profiling application similar to the initial AES project described above. Although depth profiling is an important feature of GD-AES, it has not been considered a practical application for GDMS. This section describes the establishment of operating conditions that simultaneously afford sufficient ion transport and well-defined craters for successful depth profiling with our GD-TOFMS system. Conditions were chosen by merging our previously established conditions for sufficient ion transport (TOFMS) with those that yielded good depth resolution (AES). Shown is depth profiling of thin gold films on silicon wafers, as well as samples consisting of multiple layers, such as spent computer hard discs.

CHAPTER 2 THE GLOW DISCHARGE

Introduction

A glow discharge cell consists of two electrodes immersed in a gaseous medium, typically argon. The gas is insulating by nature, but becomes conductive when sufficient potential is applied across the electrodes. Atoms of the gas break down electronically into argon ion-electron pairs, allowing current to flow through the system. The resultant glow discharge is a cool plasma that attains temperatures up to approximately 800 K.³⁹

An electrical discharge, such as a glow discharge, consists of many complex processes involving electrons, atoms, and ions of a wide range of energies. Collisions account for a significant portion of the chaotic processes that occur within a glow discharge. Sputtering, for example, is a collisional event that converts sample material into gaseous atoms. These diffusive sample atoms can collide with other energetic species, resulting in the production of photons or ions that can provide information about the plasma. Spatial zones of a glow discharge plasma are formed (or collapsed) through collisional events. The processes within a glow discharge are complex, and understanding them has been a goal of researchers for many decades.

This chapter will describe the most fundamental processes that comprise a glow discharge, and will be divided into the three separate, but related

sections. The first segment will deal with general discharge characteristics and their formation; the next section will discuss the spatial zones that comprise a glow discharge; and the final portion will treat the major species within a plasma and the processes responsible for their formation.

General Discharge Characteristics

Different types of glow discharge can be attained by altering the applied voltage and current. Discharges are generally separated into four classifications based on their voltage-current characteristics: Townsend discharge, normal glow discharge, abnormal glow discharge, and the arc discharge.⁴⁰ For analytical purposes, the discharge in the abnormal region is the most important. This region will be the central focus of this dissertation, though insight can be gained about the glow discharge by examining other regions as well.

Consider the example of a potential dropped across two electrodes submerged in an argon medium. An electrical discharge will result when the potential is applied, given the proper operating conditions. The type of discharge that forms is largely dependent on these operating conditions, as illustrated in Figure 2-1.⁴⁰ This figure shows the voltage-current characteristics of the discharge, where U_b is the breakdown voltage and U_n is the normal operating voltage.

The left-most region in Figure 2-1, the Townsend discharge regime (A-B), is generally operated at low pressures (sub-millitorr). Only a small number of ions and free electrons are produced at the breakdown voltage (U_b); hence, this regime is characterized by a low operating current and is not self-sustaining. An external

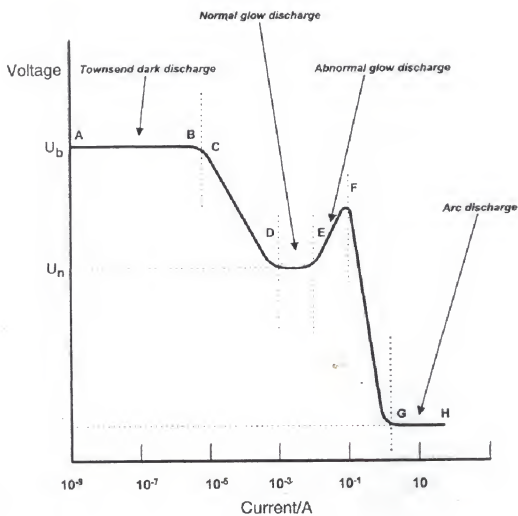


Figure 2-1. Voltage-current characteristics of a glow discharge.⁴⁰

source, such as X-rays and ultraviolet light, is needed to facilitate free electron and ion production that is needed for sustaining the plasma. The small number of collisional processes within the Townsend discharge leads to little photon production and subsequently low luminosity.

A transition region (*C-D*, Figure 2-1) is encountered when the operating voltage is increased beyond the Townsend threshold. Increased collisions in the transition region result in large energy exchanges, and subsequently higher currents.¹⁷ The potential then remains nearly constant for large variations in current, which is termed the normal discharge region (*D-E*). The discharge in this region forms only on a small portion of the cathode, and subsequently only small current fluctuations are found. This glow discharge region is noted for its luminous glow resulting from strong visible light emission.

In the abnormal glow discharge (*E-F*), the plasma begins to encompass the entire sample surface, and the current begins to increase. Sustaining the abnormal discharge requires that the applied voltage be increased as a function of current. For analytical applications requiring an emission or ion source, the information-rich abnormal region is generally chosen owing to its high population of sample atoms and ions.^{17,40}

If the current is increased beyond the abnormal region, the discharge enters a second transition region (*F-G*), which is marked by a large drop in resistance. The discharge voltage abruptly decreases and establishes high currents, even for small operating voltages. Increasing the current beyond this transition region can result in severe heating of the cathode as a result of elevated current densities. Extreme

currents are a result of intense gas bombardment and subsequent thermal vaporization of the cathode. This region, termed the arc discharge (*G-H*), currently finds limited application in analytical spectroscopy.⁴¹⁻⁴³ The spectrometrists wishing to use a glow discharge for analysis is often dismayed at the sight of an arc discharge and its erratic, unstable nature.

Glow Discharge Spatial Regions

The abnormal glow discharge, hereafter called simply the glow discharge, comprises several alternating dark and luminous regions, as shown in Figure 2-2.^{17,40,44} The formation of these regions is dependent on the configuration of the glow discharge cell employed, particularly the distance separating the electrodes. For long electrode distances, a highly luminescent positive column region is most prominent; however, it is not required to sustain a glow discharge. This region contracts as the distance between the electrodes is decreased, until eventually collapsing. Other regions of the discharge are also diminished by decreasing the electrode separation, with exception to the cathode dark space, which must exist to sustain a glow discharge. Since most analytical glow discharge devices employ short electrode distances, they generally exhibit only the cathode dark space and negative glow regions. An obstructed glow,⁴⁵ a discharge in which most of the regions have collapsed, occurs when the electrode separation is only a few times larger than the thickness of the cathode dark space.^{40,46} Further decreasing the electrode separation yields a distorted dark space region and an unstable, or extinguished, plasma. For brevity, only the three prominent regions of the glow

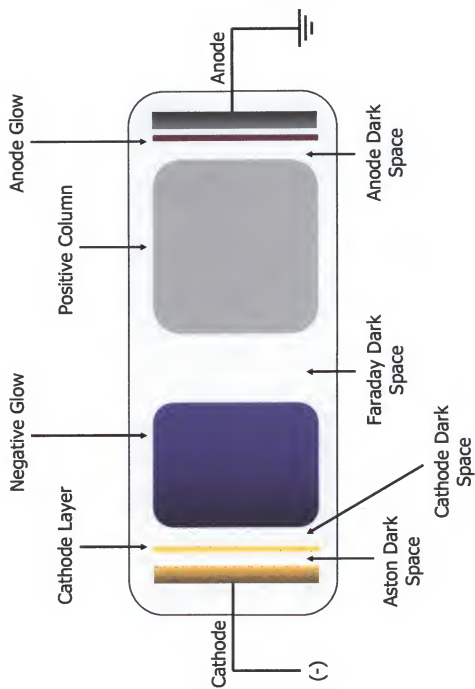


Figure 2-2. Spatial regions of a simple glow discharge device.

discharge will be discussed in the following sections: the cathode dark space, negative glow, and Faraday dark space regions.

Cathode Dark Space

The cathode dark space is a region of low luminosity that appears adjacent to the cathode (sample) surface, as depicted in Figure 2-2. Electrons are repelled away from this region due to the negative cathode potential. This electron repulsion creates a positive space, where most of the potential difference between the two electrodes is dropped.⁴⁷ Hence, the cathode dark space is often called the cathode fall region.

Figure 2-3 shows a profile of potential distribution as a function of electrode distance for the three major regions of the glow discharge. The large potential fall inherent of the cathode dark space region is represented in this figure. Electrons are accelerated away from this region and consequently have too much energy for excitation reactions. Indeed, an excitation cross-section shows a dip at these high energies,^{48,49} which accounts for the low luminosity exhibited by the cathode dark space.

Despite the lack of excitation and ionization processes occurring within the cathode dark space, a glow discharge cannot exist without this region. Electrons that are accelerated away from this region are responsible for ionizing the fill gas (Ar) in other regions of the discharge. The electrons created from these collisions may cause further ionization, while the resulting argon ions are attracted to the cathode. The continuous cycle of these complex processes leads to a self-

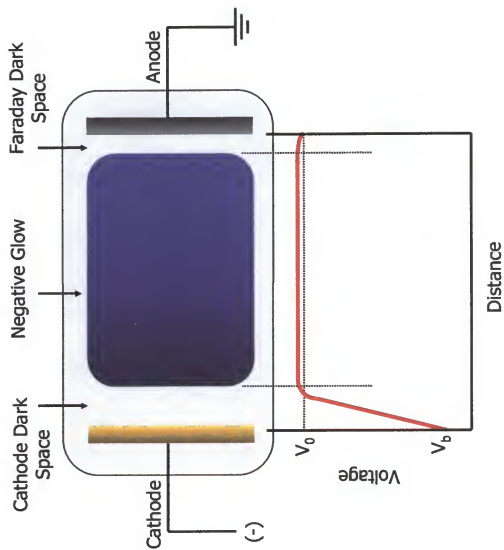


Figure 2-3. Voltage distribution for the prominent regions of a glow discharge.

sustaining discharge, which originated with the acceleration of electrons in the cathode dark space region.

Negative Glow

The negative glow region is the most visually striking region of the glow discharge. This large, bright region is adjacent to the cathode dark space and is analytically the most important region of the glow discharge. Two types of electrons enter the negative glow: fast, highly energetic electrons and slow, thermal electrons.

Fast secondary electrons are those that have fortuitously traversed the cathode dark space without losing significant energy due to collisions. These electrons, typically called group I electrons, are only capable of ionizing collisions due to their inherent high energies. Electrical (Langmuir) probe experiments show that group I electrons attain electron temperatures of $\sim 20 - 25$ eV and number densities on the order of 10^6 cm^{-3} in the negative glow region.⁵⁰

Low-energy electrons, often termed thermal electrons, are separated into two groups. Group II electrons are secondary electrons of gas-phase ionization collisions that have electron temperatures of $\sim 2 - 10$ eV, and number densities of approximately $10^7 - 10^8 \text{ cm}^{-3}$.⁵⁰ Group III electrons are actually electrons from group I or group II that have experienced several elastic and inelastic collisions within the plasma. These electrons typically have electron temperatures of only $0.05 - 0.6$ eV, and number densities in the range of $10^9 - 10^{11} \text{ cm}^{-3}$.⁵⁰ Unlike their energetic counterparts, group II and group III electrons may either excite atomic species or ionize excited state species.

The number of electrons in the negative glow is generally matched by a similar number of positive ions.⁴⁷ The combination of these free ions and electrons results in an essentially field-free region, as represented in the potential distribution of Figure 2-3 by a linear segment just above ground potential (V_0). Langmuir probe experiments have demonstrated that plasma potentials within the negative glow region vary less than 1 V for discharge voltages between 800 and 1000 V.⁵¹ Electrons are not significantly accelerated in this field-free region, and as such are capable of causing excitation collisions, resulting in a bright 'glow.' The color of this glow is largely dependent on the fill gas and to a lesser degree on the sample material.

The size of the negative glow region is affected by the discharge pressure and the distribution of electron energies. High operating pressures tend to increase the number of collisions within the discharge, which compresses the spatial distribution of the negative glow. Conversely, a wide range of electron energies can extend the length of this region.

The largest population of electrons exists at the interface between the cathode dark space and the negative glow - a result of electron multiplication by ionization processes. Accordingly, the greatest emission intensity is seen at this edge of the negative glow, which fades as a function of cathode distance. Mass spectrometers are typically configured to sample the high population of ions that exist at this negative glow interface.

Faraday Dark Space

The Faraday dark space region is found just beyond the anode end of the negative glow region. Electrons comprising the Faraday dark space are thermal electrons that have lost most of their energy due to excitation and ionization collisions.⁴⁷ In many cases, the separation between the cathode and anode is so small that this region of low luminosity is not observed.

Glow Discharge Processes

The glow discharge is a deceptively simple analytical device full of chaotic processes involving different species of varying energy. An overview of these basic processes will be beneficial to understanding the experimental results in subsequent chapters. The present section will describe an overview of the mechanisms within the spatial regions described in the previous section. For brevity, complex processes, such as multi-body collisions and sputtered clusters, will not be treated. Readers wanting a detailed description of plasma processes should consult other discussions,^{40,44,47} some of which are based on computer modeling results.⁵²⁻⁵⁵ The fundamental processes that will be described in this section, such as sputtering, excitation, and ionization, are summarized in Figure 2-4.

Cathodic Sputtering

An energetic particle that strikes a solid surface can result in an initiation of many processes. This phenomenon, termed sputtering, is a large contributor to the analytical utility of the glow discharge. Atomization of the sample occurs through ion

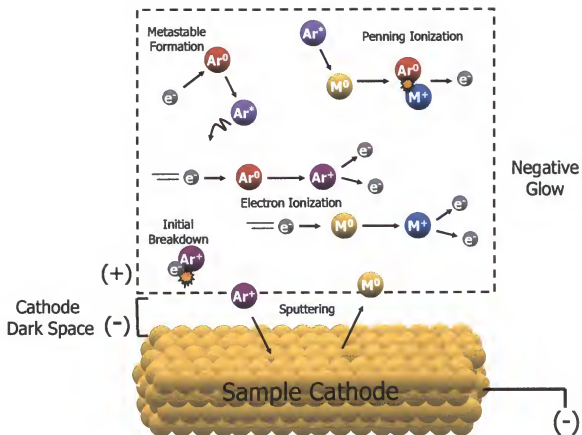


Figure 2-4. Major processes that occur in a glow discharge.

bombardment of the sample surface, and provides an atomic population for subsequent excitation and ionization processes.⁴⁷ This section gives an overview of the sputtering process, as well as quantitative principles for characterizing sputtering.

Sputtering process. The impact of a particle can lead to considerable damage to the sample through atom rearrangement or particle implantation, as illustrated in Figure 2-5. The sputtering process illustrated in this figure is simplified, as the incident argon ion typically undergoes several charge exchange reactions with neutral gas atoms before impacting the cathode surface.⁵⁶ Therefore, argon atoms can also contribute to the sputter yield, to a certain degree. Upon impact, the kinetic energy of the incident particle (e.g., Ar^+) is transferred to the sample (M) through collisional events, while the potential energy of the particle results in electron ejection. The incident argon ion is either backscattered from the sample surface or penetrates the sample and transfers its energy to the surface. If the impinging ion has sufficient velocity (>30 eV), material may be sputtered (i.e., ejected) from the sample surface in the form of atoms or molecules in neutral (M^0) or ionized states (M^+ or M^-), or electrons may be ejected.⁴⁷ Sputtered particles generally possess low energies (few eV) and can be ejected at many possible angles.

Positively charged ions (M^+), which make up approximately 1% of the total sputtered particle flux, are redeposited back onto the sample surface, as dictated by the negative cathode potential.⁵⁷ Negative ions (M^-), conversely, are accelerated

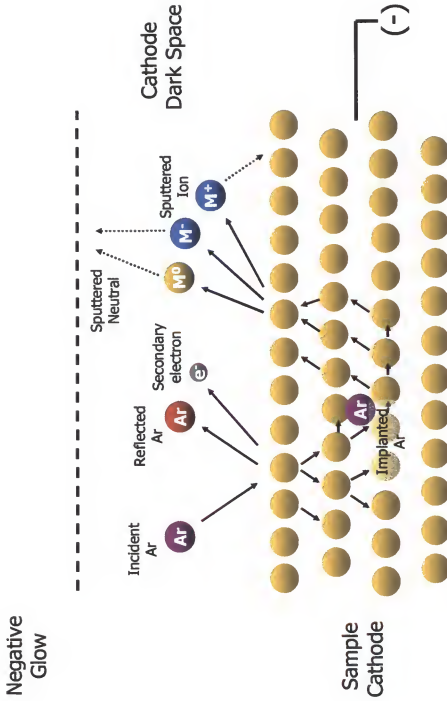


Figure 2-5. Cathodic sputtering in a glow discharge.

away from the cathode surface. Neutral sample atoms comprise the majority of the ejected material, and typically possess kinetic energies approximately 5 – 10 eV.⁵⁸ Upon ejection, most of these sample atoms lose their momentum to elastic collisions with discharge species due to the small mean free paths at the cathode surface (~0.1 mm for pressures of 0.1 – 10 torr). Weight loss studies by Harrison and Bruhn have shown that up to 95% of these atoms may be deposited back onto the cathode surface.⁵⁹ The atoms that are not redeposited can diffuse into the negative glow region and undergo excitation or ionization processes, which are essential for atomic emission and mass spectrometry measurements, respectively.

Sputter rate. The amount of sample ejected for a given analysis time is defined as the sputter rate (q – ng/s):

$$q = \Delta W / t \quad (\text{Eqn. 2-1})$$

where ΔW (ng) is the amount of sample lost due to sputtering and t (s) is the total time of sputtering. Typically, Equation 2-1 is termed the net sputtering rate for glow discharge since it recognizes that the glow discharge inherently involves redeposition of sputtered material.⁶⁰

Sputtering rates vary as a function of many parameters, including voltage, current, and pressure of the discharge. The type of fill gas may also affect sputtering, since the mass of the sputtering agent will depend on the fill gas. The type of sample can also alter the sputtering rate; multi-component alloys of the same matrix exhibit sputtering rates that are dependent on the concentration of other minor constituents comprising the sample. For example, pure copper has a

measured sputtering rate of approximately 0.67 ng/pulse for a microsecond pulsed glow discharge source.⁶⁰ Adding a constituent to the sample with a different sputtering rate, such as zinc (1.74 ng/pulse), can affect the overall sputtering rate. Weight loss measurements show that brass (70% copper and 30% zinc) has a sputtering rate of approximately 0.83 ng/pulse, which is higher than pure copper.⁶⁰

Ideally, all elements (and alloys made of the same matrix) would exhibit the same sputtering rates. However, sputtering rates vary from element to element, which can adversely affect calibration curves. One way to correct an erroneous calibration curve is to normalize it based on established sputtering rates.⁶⁰ This procedure will be described in more detail in Chapter 4.

Sputter yield. Another way to characterize the sputtering efficiency of a sample is to calculate sputter yield. The sputter yield (S – atoms/ion) of a sample is defined as the number of sputtered atoms per incident sputtering particle.⁴⁰ Boumans has experimentally developed an expression for the sputter yield:⁶¹

$$S = (1 \times 10^{-6} \cdot q \cdot N \cdot e) / (M \cdot i^+) \quad (\text{Eqn. 2-2})$$

where, q (ng/sec) is the sputtering rate, N (mole^{-1}) is Avogadro's number, e (C) is the charge of an electron, M (no units) is the atomic weight, and i^+ (A) is the ion current. The bombarding ion current is related to the total discharge current by:

$$i^+ = i / (1 + \gamma) \quad (\text{Eqn. 2-3})$$

where, i (A) is the total discharge current, and γ is the number of secondary electrons ejected by one ion.

Collisional Phenomena

Collisions account for many of the processes within the glow discharge, and contribute to the self-sustaining nature of the plasma. Collisions that occur within the glow discharge can be broadly separated into two types, elastic and inelastic.

Elastic collisions are the simplest collisions, in that kinetic energy is conserved. Excitation and ionization processes within the plasma are generally not attributed to these types of collisions, since energy is not transferred. For excitation or ionization to occur, an impinging electron must have more energy than the energy needed to remove an electron from the atom (called the ionization energy). If the energy of the electron is insufficient, it will be deflected from the atom. Since electrons and atoms have significantly different masses, the energy transfer function suggests that the amount of energy transferred for an electron-atom elastic collision is negligible.⁴⁴ Despite their inability to cause ionization, elastic collisions serve to redistribute the kinetic energy and help to thermalize the plasma.⁶²

The other type of collision within a glow discharge plasma is an inelastic collision. This type of collision, which involves energy transfer between plasma species, is responsible for (1) forming species of analytical interest and (2) maintaining the self-sustaining nature of the plasma. Since inelastic collisions comprise many of the processes that occur in the glow discharge, this section will be separated into three parts. A general description of electron behavior will be discussed first, followed by the collisional processes leading to the excitation of sputtered sample atoms. A discussion about the ionization of these sputtered sample atoms will conclude the section.

Electron behavior. Electrons within a glow discharge are accelerated away from the cathode and may eventually collide with gas atoms and cause ionization. However, many of the electrons that are formed from collisional processes are lost due to recombination.⁴⁰ Electrons can also impart their energy to an atom, thereby raising the internal energy of the atom to an excited state. When this excited atom relaxes to a ground state, a photon is released which contributes to the characteristic glow of the discharge. These photons also prove analytically useful for probing optical characteristics of the discharge.

Electrons are typically accelerated with enough kinetic energy (up to 2000 eV at 2 kV) to ionize atoms within the discharge. Argon, for example, has an ionization energy of 15.76 eV, and is primarily ionized by collisions with electrons. This process, called electron ionization, is illustrated in Figure 2-4. Electron ionization is a key process within the discharge, as evidenced by the detection of doubly charged argon (Ar^{+2}) ions by mass spectrometry; only electrons have enough energy to form these ions, which have an ionization energy of 27.63 eV.⁶²

Sputtered species excitation and ionization. Atomization of a sample in a glow discharge is accomplished by sputtering the surface with argon ions (and atoms). Atoms ejected from the sample surface can diffuse into the negative glow region of the discharge where they may undergo a series of collisions with electrons, metastable atoms, and other ions. These collisions are responsible for excitation and ionization of the sample material. For excitation and ionization to occur, however, there must be an inelastic collision between an atom and a particle with

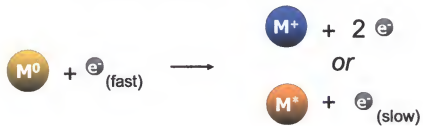
kinetic or potential energy. Table 2-1 lists the three most probable excitation and ionization mechanisms that can occur in the negative glow region. The role of these processes is largely dictated by operating conditions of the discharge.

Excitation. Generally, electrons in the virtually field-free negative glow region possess low kinetic energy. These thermal electrons have lost a considerable amount of their energy due to multiple collisions. The number of energetic electrons can be shown as an electron energy distribution function (EEDF), as illustrated in Figure 2-6. The abundance of thermal electrons will likely result in excitation mechanisms that preferentially involve energy transfer to levels $\leq 3\text{--}4$ eV above ground state.⁵⁰ These ground state transitions are primarily responsible for the atomic transitions that occur in the ultraviolet-visible region, and are responsible for the emission (i.e., glow) from the negative glow. The photons that are released can be measured by glow discharge atomic emission spectrometry (GD-AES).

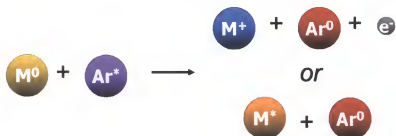
Electronic excitations involving electron impact are also credited with populating argon metastable atoms. Argon has two long-lived (approximately one millisecond) excited states with energies of 11.55 and 11.72 eV, respectively. Collisions between these metastable gas atoms and sample atoms may lead to energy transfer and subsequent excitation of the sample atom, termed a Penning collision.⁶³ This process is illustrated in Table 2-1. A third possible excitation mechanism within the negative glow region is asymmetric charge exchange.^{64,65}

Table 2-1. Common excitation and ionization processes in the glow discharge.

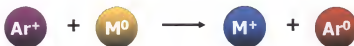
Electron Ionization / Excitation



Penning Collisions



Charge Exchange



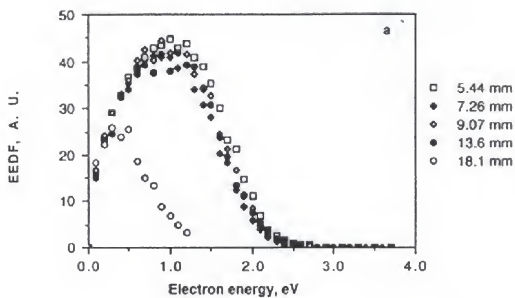


Figure 2-6. Electron energy distribution as a function of distance from the cathode.⁴⁷

Most researchers have found that this excitation mechanism is too selective to contribute significantly to excitation processes.⁶³

Ionization. The excitation mechanisms described in the previous section are also responsible for ionization mechanisms within the negative glow region. Once ions are formed they can be detected with a number of mass spectrometric techniques. The goal of an atomic mass spectrometrists is to produce (and detect) a maximum number of these ions with as much elemental uniformity as possible.⁴⁷

Electron ionization is not considered the dominant ionization mechanism, but does account for a small portion of ionization within the negative glow. This mechanism, which is shown in Table 2-1, is essentially unselective since any atom can be ionized by an electron with sufficient energy. The cross-section curve for electron ionization is similar in shape and magnitude for all elements of the periodic table.^{52,66} However, based on the EEDF shown in Figure 2-6, few electrons will have sufficient energy to ionize metals with ionization energies between 5 – 10 eV. Therefore, it is unlikely that electron ionization accounts for a significant portion of ionization within a glow discharge.

Penning ionization is generally considered the dominant ionization mechanism in the glow discharge. This form of ionization consists of a collision between an argon metastable atom and a sputtered atom, as shown in Table 2-1. The argon metastable atom should be able to sufficiently ionize most elements based on its energies (e.g., 11.55 and 11.72 eV). Like electron ionization, Penning ionization is unselective for elements with lower ionization energies than the

metastable atom energy. Separate experiments by Harrison and Coburn have demonstrated that Penning ionization is the dominant ionization mechanism in the glow discharge.⁶⁷⁻⁶⁹ Elemental quantitation studies have suggested that Penning ionization accounts for approximately 50 to 95% of sample ionization in the discharge.⁷⁰

Asymmetric charge exchange is another mechanism that may ionize sample atoms in the negative glow region, as shown in Table 2-1. However, this highly selective, and controversial process, is not credited with being a significant ionization mechanism. Asymmetric charge exchange occurs when an electron is transferred from a sputtered atom to an argon ion, and is likely only if the difference in energy between the two species is small.

CHAPTER 3 GLOW DISCHARGE MODES

Introduction

A subtle advantage of the glow discharge is its operational simplicity. One must only apply to the cathode a sufficient voltage to establish a discharge. The combination of sputtering, excitation, and ionization of the sample constituents leads to photon and ion production, which can be measured by appropriate techniques. The simplicity of the glow discharge has led many researchers to develop source configurations and modifications for particular applications. There is also a growing interest in testing alternative power sources to drive the glow discharge. This chapter will discuss the range of glow discharge configurations, as well as the operational modes, that have found analytical utility. Often, the sample characteristics (e.g., type, shape, etc.) dictate the selection of a particular source configuration and operational mode. One specific operational mode, the microsecond pulsed GD, offers special opportunities and advantages, which will be described. A discussion of analytical methods that probe the sample atoms and ions produced with a microsecond pulsed glow discharge will conclude the chapter.

Source Configurations

The diverse applications of the glow discharge have led to the development of a variety of source configurations. All of these configurations have the ability to

efficiently analyze different sample shapes, ranging from cylindrical wire samples to large metal alloys, collectively making them well-suited for a range of applications. The glow discharge configurations that will be described in this section include the hollow cathode, diode, and Grimm design. Emphasis will be placed on the latter configuration (i.e., Grimm-type design) since it is the central aspect to many of the research investigations described in the following chapters. Each configuration has its own strengths and weaknesses, which are summarized in Table 3-1.⁷¹ While many configurations have been successfully implemented, an optimum configuration that can efficiently analyze all sample types still has yet to be developed.

Hollow Cathode Geometry

The hollow cathode discharge is the oldest glow discharge configuration, dating back to the 1930s.⁷² Hollow cathode sources have enjoyed reasonable success for atomic emission measurements (e.g., hollow cathode lamps), but hollow cathode sources designed for mass spectrometric applications are rarely implemented.⁷³ The plasma in a hollow cathode is confined to a hollow cavity within the sample, which forces sputtering to occur on the sides of the cavity walls. Highly energetic atoms and electrons are trapped within this hollow, and extended residence times led to enhanced excitation and ionization of the sample atoms. Hollow cathode configurations have demonstrated detection limits down to the subnanogram range, owing to efficient ionization capabilities.⁷⁴ Typical operating conditions for a hollow cathode configuration are voltages between 200 - 500 V, currents of 10 - 100 mA, and argon pressures between 0.1 - 10 torr.⁷⁵

Table 3-1. Comparison of the glow discharge configurations.⁷¹

Source	Advantages	Disadvantages
Hollow Cathode	<ul style="list-style-type: none"> •Efficient excitation and ionization processes •Great sensitivity •High sputter rate •Amenable to powders 	<ul style="list-style-type: none"> •Ion extraction difficult •Complicated sample geometry •Sample alteration required
Coaxial Cathode	<ul style="list-style-type: none"> •Amenable to pins, wires, discs, etc. •Ion extraction easy •Ionization dominated by Penning process 	<ul style="list-style-type: none"> •Depth profiling difficult •Sample placement imprecise •Powders require conversion
Grimm Source	<ul style="list-style-type: none"> •Depth profiling possible •External sample mounting •Fast sample turnaround •Precise sample placement •Compacted powders possible 	<ul style="list-style-type: none"> •Non-flat samples difficult •Ion transport difficult

The high population of ions formed within the cavity provided impetus to design a hollow cathode source for mass spectrometry.⁷⁶ A hollow cathode configuration that has been designed exclusively for mass spectrometry applications is shown in Figure 3-1. This figure also demonstrates the confined nature of a hollow cathode plasma. While the confined plasma does provide an enhanced population of sample atoms and ions, the intrinsically confined plasma does present a concern. For mass spectrometry applications, the ions must be extracted from the hollow well and transported to the sampling region; these additional steps can prove intricate. However, the potential advantages for hollow cathode mass spectrometry studies, such as enhanced detection limits, do provide justification for developing methods to circumvent these concerns.

.

Diode (Coaxial) Geometry

The most popular glow discharge configuration for mass spectrometry, though typically not used for atomic emission, is the diode geometry.^{77,78} This design, typically called a "pin-type" source, is capable of analyzing sample types (e.g., pins, wires, discs, etc.) that can be mounted on the end of a direct insertion probe (DIP). The probe and sample assembly is introduced into the glow discharge chamber through a vacuum interlock, as illustrated in Figure 3-2. The discharge forms on the end of the sample, and ions are extracted from the negative glow region of the plasma. Diode geometries typically employ conditions of 500 – 1000 V, 1 – 5 mA, and 0.4 – 2.0 torr Ar pressures.⁷⁵ The diode configuration is arranged so that the sample serves as the cathode, while the surrounding discharge chamber

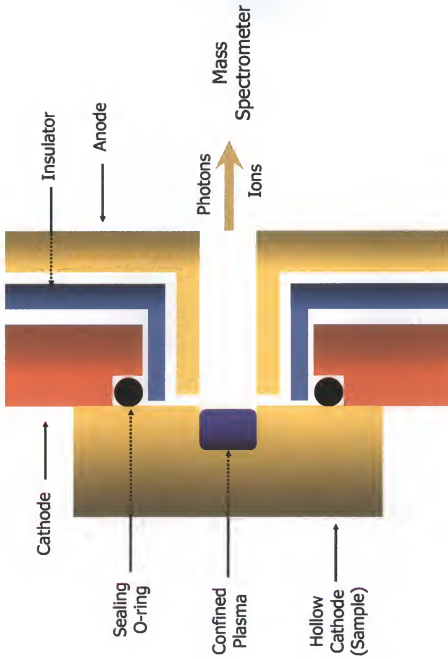


Figure 3-1. Hollow cathode glow discharge source for mass spectrometric applications.

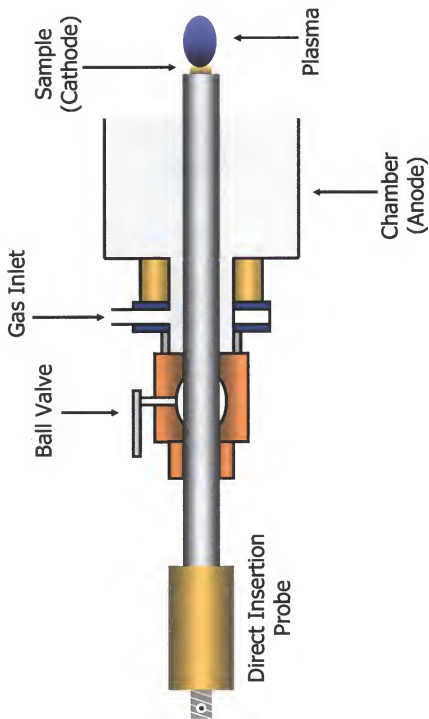


Figure 3-2. Diode (coaxial) glow discharge source.

becomes the grounded anode. The only commercially available glow discharge mass spectrometer, a VG 9000 double focusing spectrometer,⁹ employs a probe configuration for sample introduction. Limitations of this geometry include problems with sample placement, thermal effects, and redeposition on source components.¹ Further, glow discharge applications that require layer analysis, such as depth profiling, are difficult using a probe configuration.

Grimm Geometry

A source that is widely employed for atomic emission measurements and is gaining popularity for mass spectrometry applications is the Grimm-type configuration. This source design, which employs a flat cathode geometry rather than a probe assembly, was introduced by Grimm as an atomic emission source in the late 1960s.⁸⁰ The sample is pressed against an O-ring on the flat cathode plate, which ensures adequate sealing and proper vacuum conditions, as shown in Figure 3-3. This type of source utilizes a constricted plasma, in which the discharge is laterally restricted to the sample surface and confined to the size of the surrounding anode. Restriction of the plasma to the sample surface is achieved by maintaining a distance between the anode tip and sample that is smaller than the mean free path of the electrons.⁸¹ The plasma is also confined in circumference by the cylindrical anode, which allows planar sputtering of the sample. Typical operating conditions of the Grimm-type source are approximately 500 – 1500V, 3 – 30 mA, and 2 - 6 torr Ar.⁷⁵

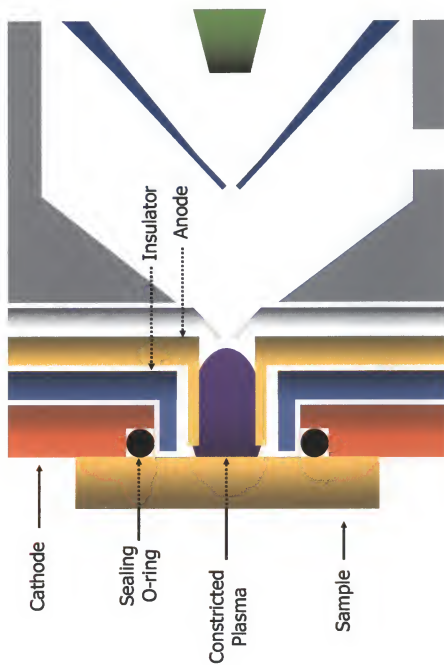


Figure 3-3. Grimm-type glow discharge configuration.

The easy sample interchange provided by the Grimm source is a significant advantage over other source configurations.⁸²⁻⁸⁵ Samples are mounted externally on the source, affording quick sample turn-around time and precise sample placement. Sample positioning concerns, which can plague probe-type configurations, are avoided with the Grimm-type source.^{80,86} Another well established feature of the Grimm configuration is its ability to obtain surface and in-depth analysis by properly controlling the discharge parameters to obtain planar sputtering.^{60,87,88} The ability of the Grimm-type source to analyze thin sample layers with pulsed operation has been demonstrated,^{60,89,90} and is described for atomic emission and mass spectrometry in Chapter 4 and Chapter 8 of this dissertation, respectively.

One of the aforementioned features of the Grimm-type configuration - its ability to analyze flat samples - can also be a concern. A flat, smooth sample surface is required to ensure adequate sealing. Other sample shapes, such as pins and wires that have a smaller diameter than the diameter of the anode, are less adaptable. Another limitation of the Grimm configuration, at least for mass spectrometric applications, is ion transport. Transport efficiency, which is crucial to the success of mass spectrometry, is difficult to optimize with this flat cathode geometry. Methods of circumventing these two limitations (i.e., ion transport and sample adaptability) have been studied, and will be described in Chapter 6 and Chapter 7, respectively.

Operational Modes

The electrical characteristics of a glow discharge largely determine its performance, and the diverse applications of the glow discharge have led to the development of many operation modes. The glow discharge may be powered by direct current (dc), radio frequency (rf), or pulsed operation. Emphasis will be placed on the microsecond pulsed mode since it is the central aspect to many of the studies described in the following research chapters. Not surprisingly, all of these operational modes have inherent benefits, such as the ability to temporally separate analytical signals or the ability to analyze non-conductive samples. The operational mode of choice largely depends on the nature of the sample to be analyzed.

Direct Current

The direct current (dc) mode is unquestionably the preferred method of powering the glow discharge. The inexpensive power supplies that drive these continuous discharges are dependable, rugged, and easy to operate. A glow discharge operated with a dc voltage creates a constant supply of sputtered atoms that diffuse through the glow discharge chamber, as depicted in Figure 3-4.³⁸ The discharge is self-cleaning due to the inherent sputtering mechanism. Atmospheric exposure and human contact can deposit impurities (e.g., oxide layers, water vapor, etc.) on the sample surface. However, these contaminants are automatically removed via the sputtering process. Often, the discharge is unstable during the first few moments after ignition due to the electrical nature of these contaminants. An induction period, called a pre-burn, is used to clean the surface and stabilize the

discharge prior to signal collection. This pre-burn time can range from seconds to minutes depending on the sample and experimental conditions.

After the pre-burn period, the dc discharge provides a stable plasma with a steady-state production of sample atoms, as shown in Figure 3-4. A sputtered atom gradient is produced, as shown by the concentration contour. Despite the steady-state nature of the plasma, the number densities of the species comprising the plasma can vary significantly.⁶² The number densities of these species have been predicted mathematically and have shown good correlation with experimental data.⁹¹ The results of these modeling studies show that electron impact and Penning ionization are the dominant ionization mechanisms of the dc GD.⁹²⁻⁹⁴

Since the glow discharge establishes a stable concentration gradient, reproducible results can be obtained by consistently sampling the same region of the discharge. For atomic emission measurements, the negative glow region of the discharge is probed because of its high photon population. Absorption and fluorescence measurements, however, are sampled in the dark space which provides a low emission background.⁶² Mass spectrometry measurements require physical transport of ions to the mass analyzer, which can limit their means of sampling.

The direct current mode of operation has two significant disadvantages: power limitations and conductivity requirements. The dc glow discharge is operated at approximately 1 kV with currents less than 50 mA. This yields operating powers that are generally lower than ten watts.⁶² Conversely, techniques such as laser ablation, inductively coupled plasma (ICP), and electrothermal vaporization (ETV),

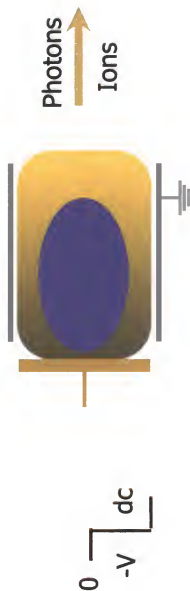


Figure 3-4. Representation of a direct current glow discharge.³⁸

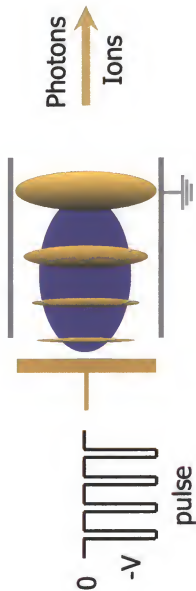


Figure 3-5. Representation of a pulsed glow discharge.³⁸

operate in the kilowatt power regime. Some samples require the use of high power, which is not provided by the cool plasma formed by the glow discharge.

The electrical nature of the sample also presents a concern for a GD operated in the dc mode – only conductive samples are amenable. This is a significant disadvantage compared to techniques such as laser ablation that can readily produce atom populations of insulating materials.²⁴ The conductivity requirement of the dc glow discharge is not a problem for the metallurgical industry, but many samples of analytical interest, such as glasses, soils, and ceramics, are inherently nonconductive. Two methods have been proposed to circumvent this limitation. One method is to incorporate a conducting matrix within the sample. The insulating sample is crushed into a powder and mixed with a conductive matrix.⁹⁵ This method, however, adds a time-consuming sample preparation step and can introduce impurities into the sample. A secondary conductive cathode can also be employed to analyze non-conductive samples with a dc GD source. In this technique, a conductive ring is placed above the non-conductive sample surface, leading to sample sputtering.⁹⁶

Radio Frequency

The inability of the dc source to directly analyze nonconductive samples provided impetus to develop the radio frequency (rf) glow discharge. This source, originally proposed by Wehner,⁹⁷ uses a rapid oscillating power at typically 13.5 MHz to produce a net bias voltage that induces sputtering on insulating samples. Matching networks are needed to couple the rf power to the sample surface.

The response attained when a dc source is used to analyze an insulating surface is analogous to charging a capacitor. When a negative voltage is applied to an insulating sample, the potential on the surface initially drops, but then decays rapidly to more positive potentials due to ion neutralization reactions on the sample surface.⁹⁸ A discharge formed on the sample surface will indeed be short-lived. The rapid oscillating power of the rf discharge, however, provides a source of electrons for ion neutralization while maintaining a negative potential on the cathode.^{97,98}

Sample thickness is an important consideration for rf-operated GD sources, unlike other modes of operation. The thicknesses of an insulating sample can affect the amount of power that is coupled to the sample. Non-coupled (i.e., reflected) power can hinder the efficiency of an rf plasma. Reflected power can also turn the rf GD source into a radio transmitter, which can cause considerable electronic pickup if the source and other components are not properly shielded.

Radio frequency sources are able to analyze conductive samples, adding versatility to this mode of operation. The sputtered atom profile is similar to that of a dc source, which was represented in Figure 3-4. One disadvantage, however, is that the sputtering efficiency of an rf discharge is often less than obtained with a dc-operated source. The rf source yields less sputtering, and subsequently fewer sample photons and ions, than a dc-operated source for the analysis of conductive samples. While the reasons for this sputtering deficiency are not completely understood, it may be attributed to a lower average dark space potential, which draws argon ions onto the cathode (sample) surface.⁹⁹ The sputter rate for insulating samples is typically an order of magnitude less than the corresponding

sputtering rate for a conductive sample.⁹⁹ Additionally, the mechanisms responsible for excitation and ionization within the rf discharge are not fully understood. The cost and complexity of the rf source, in addition to its reduced analytical signals, are responsible for its minimal commercial application.

Pulsed

The previous operational modes have employed a continuous power regime; a steady-state discharge is formed, producing an continuous gradient of sputtered atoms, as shown in Figure 3-4. These techniques are limited by the power level that can be tolerated by the sample.⁹⁹ A sample being analyzed *via* glow discharge must efficiently dissipate heat that is produced during the sputtering process. A steady-state source may not allow proper heat dissipation under extreme operating conditions. Small samples such as pins and wires can overheat, leading to thermal effects, such as melting.

One method of extending the glow discharge to higher power levels is by applying a transient voltage to the sample. Indeed, one thrust for developing a pulsed source was to combat the thermal effects that are encountered with steady-state sources. Pulsing an analytical source is not novel; laser and NMR devices are well-established pulsed sources that have inherent advantages. Likewise, the glow discharge can benefit from operating with a duty cycle, by gaining the ability to employ elevated potentials. The application of high transient voltages is possible only if the power is not supplied too long as to alter the sample. Piepmeir first reported enhanced emission intensities by pulsing a hollow cathode device.¹⁰⁰ This

initial foray paved the way for future pulsed glow discharge experiments by Harrison and colleagues in the mid-1970s.¹⁰¹

The principle of a pulsed glow discharge source is shown in Figure 3-5.³⁸ A high voltage, negative pulse is applied to the sample, resulting in a sputter release of atoms. The voltage is terminated and then applied again some microseconds later, producing another 'packet' of sample atoms. As these packets diffuse across the discharge chamber, they collide with other species, causing them to slow and diffuse. In a manner similar to the dc mode, the resulting photons and ions can be detected via optical emission and mass spectrometric techniques, respectively. The benefits of pulsing a glow discharge will be described in the next section of this chapter.

Concerns about applying a pulsed voltage to a sample may arise in the reader's mind. For example, the application of this intermittent power could lead to the formation of multiple unstable plasmas. However, the individual plasmas formed are just as robust as a steady-state plasma, given the proper operating conditions. Accordingly, the analytical signal produced by each pulse is reproducible. Indeed, some limitations of the pulsed glow discharge are encountered. Pulse generators are more complex and expensive than dc sources, and special equipment is needed to gate and collect transient signals. In summary, the advantages that are gained by pulsing a GD significantly offset the trivial disadvantages inherent with this exciting technique.

Microsecond Pulsed Glow Discharge Advantages

Operating a glow discharge with a transient voltage, as shown in Figure 3-5, affords advantages compared to continuous discharges. One advantage already described is reduced sample heating through heat dissipation during the off-time of the plasma. However, this solitary advantage is probably not sufficient to justify the additional requirements of a pulsed GD, such as pulsed high voltage supplies and gated electronics. Luckily, many other advantages are found with the pulsed mode of operation, which will be described in this section.

Two pulsed modes, the millisecond-^{102,103} and microsecond-regime,^{13,104} have been successfully implemented for GD application. Both regimes offer significant advantages compared to continuous operation, but the smaller duty cycle of the microsecond pulsed mode provides additional opportunities. Despite being a technique in its infancy, the microsecond pulsed GD has demonstrated advantages and possibilities that have propelled it to the forefront of glow discharge research in our laboratory. The pulsed advantages described in this section will consider only the microsecond pulsed regime; also, reference to the 'pulsed mode' hereto will refer only to the microsecond pulsed mode.

Additional Control Parameters

The operating conditions of the glow discharge that must be controlled, regardless of the power mode, are voltage, current, and pressure. Two additional control parameters are available to a GD operated in the pulsed mode: pulse width and frequency. The pulse width is the time (in μs) for which the voltage is applied to

the sample. Typical pulse widths are between 10 and 30 μs . The frequency at which the intermittent voltage is applied to the sample is termed the pulse frequency. Pulse frequencies are chosen between 100 and 1000 Hz. Higher frequencies can be applied, though frequencies less than 100 Hz typically yield unstable plasmas.

The ability to control these two parameters offers an advantage for the microsecond pulsed mode. The sample removal rate can be altered by controlling the applied pulse width and frequency, while depth resolution is unaffected. For the analysis of thin films or multiple-layered samples, the ability to control the rate of sputtering is a significant advantage. Thin films that would be removed immediately with dc operation show extended sputter removal times with a microsecond pulsed glow discharge source and properly chosen conditions.^{60,89,90} The ability to control the sample removal rate for thin film analysis is demonstrated in Chapter 4.

Enhanced Sputtering Rates

The intermittent nature of the pulsed GD allows higher operating voltages than with a continuous, dc GD. This added benefit is a result of the reduced sample heating inherent of a pulsed discharge. Typical voltage thresholds are 600 to 1200 V and 1000 to 3000 V for a dc and microsecond pulsed glow discharge, respectively. Likewise, current levels are considerably higher for a pulsed discharge with nominal values from tens to hundreds of milliamps, compared to only tens of milliamps for comparable dc methods.

The application of higher voltages can result in an enhanced production of electrons, which in turn, increases the amount and efficiency of ionization, leading to

elevated ion signals. The higher potential also enhances the acceleration of impinging argon ions that are responsible for sputtering the sample surface, yielding enhanced sputter rates. The pulsed glow discharge has shown 14-fold enhancements in sputtering rates over the dc discharge when the time scale is normalized.^{62,83} The average sputtering rate, however, will be lower for the pulsed system when factoring in the duty cycle of the pulse.

Enhanced Ionization and Emission

The pulsed glow discharge not only creates a higher population of sputtered atoms than a dc discharge, but also leads to higher energy species. The combination of these two factors can yield enhanced excitation and ionization processes, producing more photons and ions for atomic emission and mass spectrometry, respectively. Emission signals from glow discharges and hollow cathode lamps using the pulsed mode have displayed enhancements up to 3 orders of magnitude over their dc operated counterparts.¹⁰⁵ Similarly, GD mass spectrometry experiments have shown ion signal enhancements by employing a transient source.³⁷

Temporal Resolution

Advantages of the pulsed discharge described thus far have given substantial reason to operate a glow discharge in a transient mode. Enhancements in (1) heat dissipation, (2) sputtering control, and (3) atomic and ion signals are all noteworthy

benefits. However, the most significant advantage of a pulsed glow discharge source is the ability to achieve time-resolved measurements.

An intermittent GD consists of repetitive, high-voltage pulses that create a cascade of physical and chemical interactions with each pulse. As voltage is applied to the cell, argon atoms break down electrically, yielding sputtering agents (i.e., Ar^+ and Ar^0) that convert the solid sample into a gaseous mixture. A delay separates the initial formation (and detection) of these argon atoms and ions, and sputtering of the sample atoms and subsequent ionization. Typically, an induction period of 0.5 – 1 ms is found between the measurement of argon species and the initial measurement of sputtered species.³⁸ This induction period results in special temporal responses for different elements. Analytical advantages can be obtained by delaying the detection of these diverse temporal responses for each element. Temporal advantages have been obtained for atomic emission techniques and mass spectrometry, both of which are described in the next section.

Pulsed Glow Discharge Spectroscopies

The temporal elemental differentiation resulting from time-dependent phenomena of the pulsed glow discharge can be beneficial for a variety of analytical techniques. Figure 3-6 illustrates analytical methods that have been used in conjunction with the pulsed glow discharge source. All of these techniques benefit from the pulsed glow discharge source to some degree. In the case of atomic

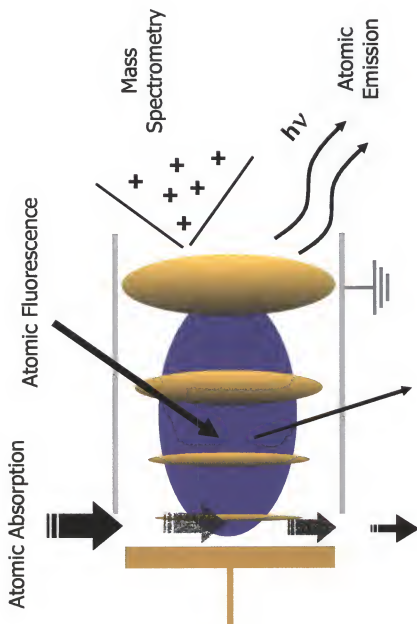


Figure 3-6. Pulsed glow discharge analytical techniques.

emission, the advantages are small, but potentially useful. For mass spectrometry, however, the gain is substantial.

Atomic Fluorescence/Absorption Spectrometry

Few sputtered sample atoms travel far from the cathode within a nominal pulse width of 10 or 20 μ s, as collisions serve to impede their progression across the glow discharge cell. These atoms can achieve long lifetimes, often in the millisecond regime, as a result of these collisional events.³⁸ At this extended time-scale most of the non-sputtered species, such as electrons and argon ions, have been reduced, providing a minimal background for spectroscopic measurements in the post-pulse period. Atomic fluorescence measurements have shown signal-to-background improvements by measuring the sputtered atoms after pulse termination.¹⁰⁶ Likewise, atomic absorption measurements can benefit by taking measurements within the dark period of the plasma.

Atomic Emission Spectrometry

The use of a pulsed glow discharge offers potential advantages for atomic emission measurements. Figure 3-7 shows a representation of the temporal responses for various elements that are produced with a pulsed glow discharge, and illustrates the temporal resolution possible with an atomic emission spectrometer.³⁸ The initial emission response corresponds to the discharge gas, argon, which is detected early due to its photon release immediately after the plasma voltage is applied and the gas is broken down electrically. Emission from the sputtered sample

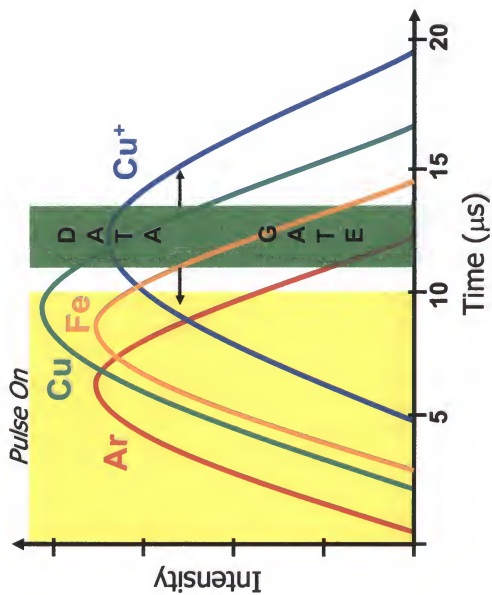


Figure 3-7. Time-resolved profiles from a microsecond pulsed glow discharge and atomic emission spectrometer.³⁶

atoms (e.g., copper and iron) appear later due to the time required for sputtering and excitation of these sample atoms. Emission from metal ions (e.g., copper ion) is detected last, since these species require additional time to undergo ionization prior to detection.

The temporal response for pulsed discharges have been employed for obtaining enhancements in the signal-to-background for selected elements in iron samples.⁸² In these studies by Bengtson and Yang, nitrogen emission originating from the samples was preferentially detected, while background nitrogen emission from the discharge gas was discriminated. This temporal detection was achieved by positioning a collection window (i.e., data gate), at an extended delay in which emission responses originate from the sample atoms and ions, as shown in Figure 3-7. The high instantaneous powers of the pulsed discharge also yielded a two-fold signal-to-background enhancement.⁸²

Time-of-Flight Mass Spectrometry

Operating a glow discharge in the pulsed regime offers the biggest rewards for mass spectrometry. Temporal advantages have been shown for the a millisecond pulsed discharge source coupled to a quadrupole mass spectrometer, in which calcium was detected in the presence of argon through time-gated detection.¹⁰² However, the largest benefit of a pulsed source can be obtained by coupling a microsecond pulsed GD to a time-of-flight mass spectrometer (TOFMS). A TOFMS requires a pulsed introduction of ions and forms individual mass spectra based on a duty cycle of these pulsed events. The ion packets produced by a

microsecond pulsed GD are well-suited for the duty cycle of a time-of-flight, and the time-dependent events offer special opportunities.^{14,38}

Figure 3-8 shows the time-resolving principle that is possible with the combination of a microsecond pulsed GD and TOFMS. Argon ions, shown as red spheres in Figure 3-8, are formed first in a discharge, followed by the production of sample ions. After being sampled and skimmed, the ions are focused by ion lenses and enter a repelling region. This region redirects ions into the time-of-flight by applying a high positive voltage (typically 1 kV) to the back plate of the repeller. Extraction is unselective – any ions in the repelling region during the voltage on-time may be sampled and detected. Controlling the repeller pulse timing allows discrimination of certain ions based on their temporal characteristics. Typically, argon ions are measured between delay times of 10 and 100 μs , while sample ions are detected between 80 and 250 μs . The magnitude of the delay time depends on the operating conditions and configuration of the GD source. Temporal resolution is achieved by operating at conditions that maximize the separation between the argon ions and sample ions as they enter the repelling region.

Figure 3-9 represents the time resolved spectra that can be obtained by varying the delay between the application of the repeller voltage and the plasma voltage.³⁸ Within the first 100 μs , ions extracted are representative of the background gas ions (e.g., argon, water, etc.). Analyte ions have yet to reach the sampling orifice due to the time required for diffusion after the sample is sputtered. As the delay time is increased beyond 100 μs , analyte ions

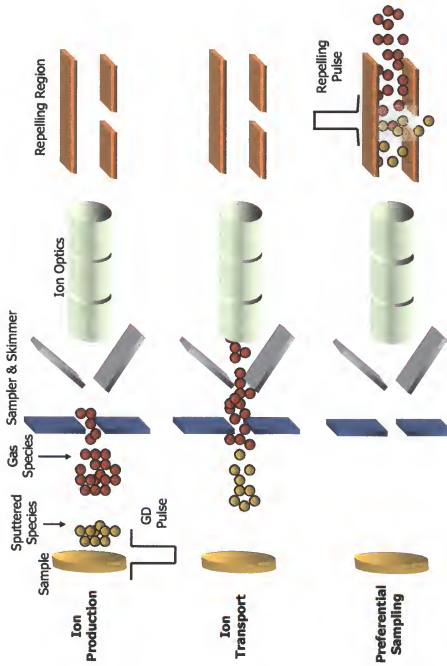


Figure 3-8. Principle of temporal separation using a microsecond pulsed glow discharge and time-of-flight mass spectrometer.

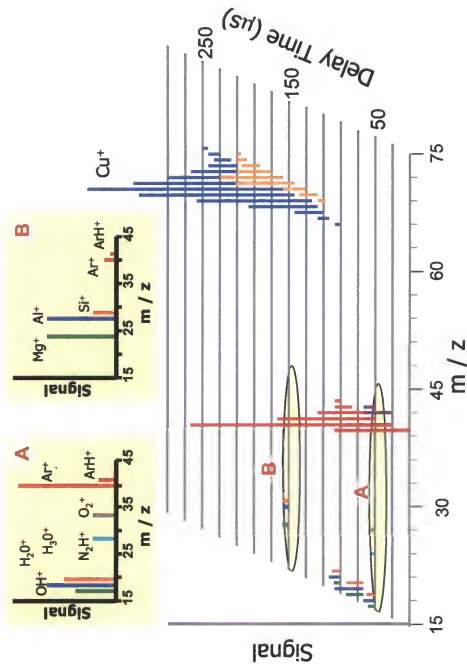


Figure 3-9. Time resolved spectra from a microsecond pulsed glow discharge and time-of-flight mass spectrometer.³⁸

(e.g., copper ions) begin to arise while discharge gas ions disappear. Typically, mass spectra are collected at optimum delay times to preferentially detect sample ions while potentially interfering gas species are discriminated. This ability is particularly important for low-mass elements, as shown in the subsets of Figure 3-9, which are prone to interferences from background contaminants.^{37,38}

CHAPTER 4 QUANTITATIVE DEPTH ANALYSIS USING MICROSECOND PULSED GLOW DISCHARGE ATOMIC EMISSION SPECTROMETRY

Introduction

Glow discharge atomic emission spectrometry (GD-AES) is a mature spectroscopic technique, dating back approximately 100 years. However, modern glow discharge spectrometry is generally associated with the development of the Grimm source design in 1968.⁸⁰ A common application of this technique, surface and depth profile analysis, first done in 1973 by Belle and Johnson,¹⁰⁷ employed the Grimm-type glow discharge, the most commonly used GD emission source today.

Successful glow discharge depth profile analysis has been shown using both direct current (dc) and radio frequency (rf) sources, including quantitative analysis comparisons.^{108,109} While rf sources have the advantage of being responsive to conducting and nonconducting samples, the majority of depth profile work has been performed using dc sources. A third type of source is the pulsed glow discharge source, which has certain potential analytical advantages over a steady-state dc source, including enhanced control of sputtering rate, increased emission intensities, and possible temporal factors.

Because the sputtering process can be altered by controlling the pulse frequency and pulse width, extension of the pulsed technique to depth profiling affords more flexibility in thin layer analysis. Layers of a few atomic distances can be removed over an extended time scale by using a lower duty cycle that provides a

slower sputtering process. This research shows the application of a microsecond pulsed glow discharge for quantitative depth profile analysis of thin foils. The quantification method is based on a similar method done by Bengtson and colleagues with a dc GD source, a technique applied here to the pulsed GD source.

Experimental

Instrumentation

A standard Grimm GD source (LECO Corp., St. Joseph, Michigan, USA) was used for all experiments. The tubular-shaped anode (4 mm i.d.) of the source extends to approximately 0.2 mm from the sample. The spectrometer was a slightly modified LECO SA-2000 direct reader, which uses a 0.4 m direct-reading spectrometer with a 2400-groove holographic grating. A picture and schematic of the microsecond pulsed Grimm GD-AES is shown in Figure 4-1 and Figure 4-2, respectively.

The Grimm glow discharge was operated in the pulsed mode using a high-voltage pulsed power supply (Model: M3k-20-N, IRCO, Columbia, Maryland, USA). This power supply is capable of internal pulsed operation, but for greater flexibility, a separate pulse generator (Model: 8003A, Hewlett-Packard, Palo Alto, California, USA) was used to trigger both the pulse power supply and the boxcar integrators to synchronize the firing of the discharge and resultant signal collection. A pulse counter (Model: 5740, Data Precision Corp., Wakefield, Massachusetts, USA) was added to monitor the number of pulses from the power supply. The signal readout and data system of the LECO spectrometer was altered to permit incorporation of



Figure 4-1. Photo of the microsecond pulsed Grimm glow discharge atomic emission spectrometer.

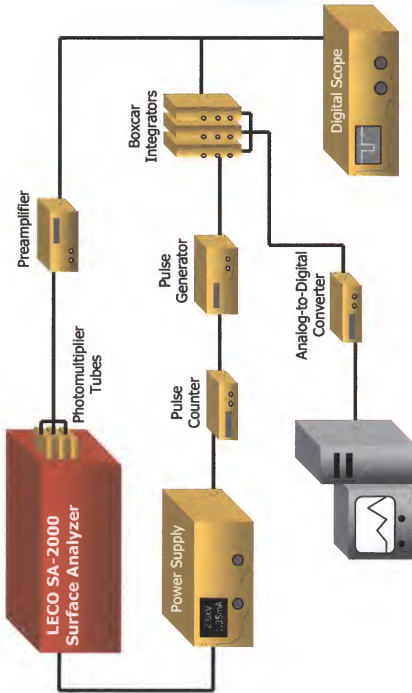


Figure 4-2. Schematic diagram of the pulsed Grimm glow discharge atomic emission spectrometer and gated detection system.

the microsecond pulsed signal. The output currents of the photomultiplier detectors were converted to voltages by dropping the signal across a 66.3 k Ω resistor. The signals were processed in two ways. The first system consisted of a 2 Gsa/s, 400 MHz, four-channel digital oscilloscope (Hewlett Packard, Palo Alto, California, USA). The output signal, discharge voltage and discharge current were displayed simultaneously on the oscilloscope, which afforded plasma stability monitoring. The voltage was attenuated through a 1000:1 voltage probe, while the discharge current was determined by calculation from the peak voltage dropped across a 5.1 Ω carbon resistor.

The second readout system consisted of gated boxcars and a computer. The signals from the photomultiplier tubes were temporally gated and processed with a boxcar integrator (Model: SR250, Stanford Research Systems, Sunnyvale, California, USA), and then sent to a computer *via* an analog-to-digital converter (Model: SR245, Stanford Research Systems, Sunnyvale, California, USA). The timing diagram of the system involves a waveform generator to control both the pulsed power supply and the boxcar integrators.

Sample Material

Sputter rate protocol. Samples used for obtaining sputter rates were high purity elemental foils approximately 0.1 mm thick (Puratronic, Alfa AESAR, Ward Hill, Massachusetts, USA). Samples were cut into small discs just larger in diameter than the O-ring surrounding the anode, approximately 15 mm, and weighed using an analytical microbalance (Model M2P, Sartorius Corp., Edgewood, New York, USA)

prior to analysis. The thin nature of the films necessitated sample cooling, which was achieved using a cooling puck option that was available on the LECO spectrometer. The foils of lead and tin required modification prior to sputtering. These samples were so soft that, once put under vacuum, contact was made with the anode, thereby shorting out the discharge. This was overcome by adhering the sample disc to a less malleable sample, e.g., a copper disc of equal size, prior to analysis.

The samples were sputtered for 40 minutes and then re-weighed to determine the weight difference due to sputtering. Although sputtering rates could be determined using the net "sputter time," it was typically more precise and more accurate to measure the number of pulses from the power supply *via* a pulse counter. Each sample was analyzed three times, using a new sample for each run.

Additional samples. Additional samples were employed in the quantification study. Bulk materials used in generating the calibration curve were iron standard samples (spectrometric reference materials, cast Iron C18.8, CKD232-239, Research Institute CKD, Prague, Czech Republic) as well as NIST 1107, 1110, and 1113 brass standard samples (National Institute of Standards and Technology, Gaithersburg, Maryland, USA). Samples used to show the quantification method were pure copper films deposited on polished iron substrates and were prepared in the Department of Materials Science and Engineering, University of Florida. Copper and iron were the only elements of significant mass fraction in the sample; the purities are 99.5% copper and 99% iron, respectively.

Results and Discussion

Optimization of Conditions

Glow discharge quantitative depth profiling depends on the sample material being removed uniformly layer by layer across the area exposed to sputtering by argon ions and fast atoms. Modeling of excitation processes have shown that both operating voltage and pressure are responsible for erosion uniformity, while the discharge current determines the number density of bombarding particles and the sputtering rate. Sputter induced effects, such as surface roughening and sample mixing, are common to all surface techniques employing sample erosion for depth analysis, including glow discharge atomic emission spectrometry and secondary ion mass spectrometry.

The formation of crater curvature by non-uniform erosion due to poorly chosen parameters tends to degrade measured intensity-time curves and consequently decreases the accuracy of the quantitative measurement of film thickness. The depth resolution is limited largely by the curvature of the sputtered crater and its roughness. In the case of secondary ion mass spectrometry, the surface roughness can be improved by rastering the ion beam across the sample surface; however, rastering is not possible with glow discharge analyses. Therefore, it is important to use optimum experimental conditions that sharpen the intensity-time profiles, thereby enhancing the depth resolution. The literature shows reports regarding the influence of operating parameters on crater shape for both the dc GD¹¹⁰⁻¹¹³ and the rf GD.¹¹⁴ More recently, our group has studied this influence using the microsecond pulsed Grimm glow discharge,⁹⁰ which shows some significant

deviations from the characteristics of a dc GD. For example, the depth resolution of micron sample layers analyzed via dc GD sources is not significantly affected by surface roughness. Conversely, the analysis of sub-micron sample layers, such as via our pulsed glow discharge, requires that the crater curvature and surface roughness be carefully controlled.

Effect of voltage and pressure. For the case of the microsecond pulsed glow discharge, we see that high operating pulse voltages and pressures yield an increased sputtering rate, while low voltages and pressures yield decreased sputtering rates. Therefore, controlling the discharge power is critical to the crater shape and depth resolution. Figure 4-3 shows the effects of three different operating powers on crater profiles.⁹⁰ The respective peak discharge settings were: (a) a low power regime of 100 W (800 V, 0.12 A, 3 torr); (b) a medium power regime of 270 W (1200 V, 0.22 A, 4 torr); and (c) a high power regime of 680 W (2000 V, 0.35 A, 3 torr). The sputtering time of the three trials was slightly varied to normalize the depth of sputtering.

As shown in Figure 4-3 (a), concave crater shapes, those that have an inherent dip in the middle of the profile, result from sputtering at low power (voltage). Conversely, convex crater shapes, which have a bulge in the middle, are the result of employing high power (voltage), as shown in Figure 4-3 (c). Only a mid-range pulse voltage yields a relatively flat crater bottom, which is indicated in Figure 4-3 (b). For example, the optimum pulse voltage is between 1200 V and 1400 V for a 3 torr argon gas discharge. The same trend between power and crater shape was

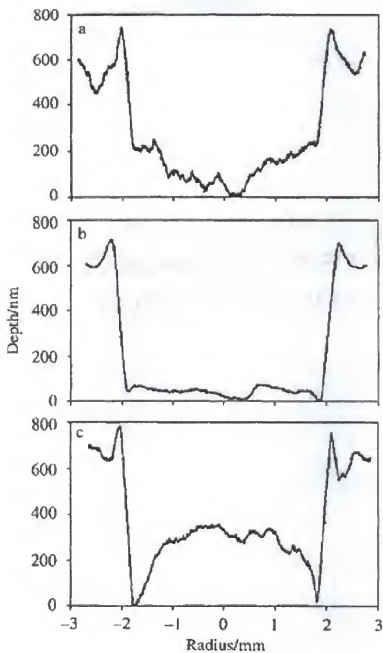


Figure 4-3. Crater profiles for different operating conditions: (a) 100 W; (b) 270 W; (c) 680 W.⁹⁰

observed with a dc discharge,¹¹⁰ except the range of voltages is higher in the pulsed mode. A possible explanation for this trend is that the crater shape results from the electric field focusing or defocusing the bombarding ions responsible for sputtering.⁹⁰

Figure 4-4 shows the effect operating voltage can have on crater profiles.⁹⁰ Figure 4-4 (a) is a magnified digital image of a sputter pattern of a copper layer on steel at low voltage (800 V, 3 torr, 10 μ s pulse width, 200 Hz). The image has been digitally altered to enhance the contrast between the copper and steel layers. The dark circular region in Figure 4-4 (a) marks the edge of the deep sputter erosion area. The lighter surface represents the copper top layer, whereas the gray center region illustrates the exposed steel layer. The low power conditions result in a concave crater, as shown in Figure 4-3 (a), and also a small emission intensity due to a lower sputtering rate.

At high pulse voltages (e.g., 2000 V), the sputter rate and emission intensity are increased. However, the crater shape shows the underlying layer to be exposed asymmetrically at the edge of the crater first. Figure 4-4 (b) is a digital image of a sputter region under the same operating conditions as in Figure 4-4 (a), except at a higher pulse voltage (i.e., 1800 V). A contribution from the underlying layer is observed early, while significant amounts of the top layer are still present in the center of the discharge area, as shown in Figure 4-3 (c). This awkward crater shape extends the signal overlap of the two layers, rather than the desired sharp transition. Observing the sample crater under a simple optical microscope, the contrast between the copper and iron layers can be clearly followed as a function of discharge conditions. Since both high and low voltage discharges produce higher

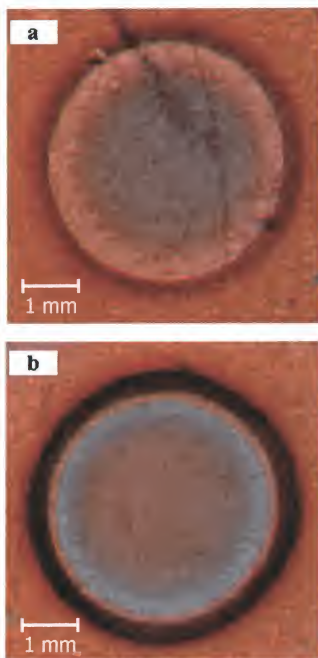


Figure 4-4. Images of burn spots for a copper layer on a steel substrate: (a) low voltage at 800 V; (b) high voltage at 1800 V.⁹⁰

sputtering in one localized region and reduced sputtering in another, the signals from each are correspondingly unsatisfactory. The cause of poor depth resolution is the non-uniform erosion under very high or very low operating power.

Effect of pulse width and pulse frequency. Pulse widths and pulse frequencies had little influence on crater shapes, as long as the pulse voltage and gas pressure conditions remained constant. The effect of pulse width and pulse frequency on the sputter rate of a brass sample is shown in Figure 4-5 and Figure 4-6, respectively. The results show that depth resolutions at different pulse widths and frequencies are essentially constant under the conditions used.

The main advantage of these two pulse parameters lies in their ability to increase or decrease the sputtering rate without altering the depth resolution. Because of the reduced duty cycle of the pulsed source, less material can be removed per unit time. Thus, a wide range of layers from several nanometers to tens of micrometers can be analyzed. The optimum pulse width and pulse frequency conditions for microsecond pulsed depth profiling of the samples involved in this research were 10 μ s and 400 Hz, respectively. These conditions were chosen because they allow a significant amount of sample material to be sputtered for the given analysis time.

Effect of sputtering time. The final parameter to be studied was the time allowed for the sample to sputter. In theory, time should have no influence on sputtering rates of pure samples since sputtering will simply penetrate deeper into a

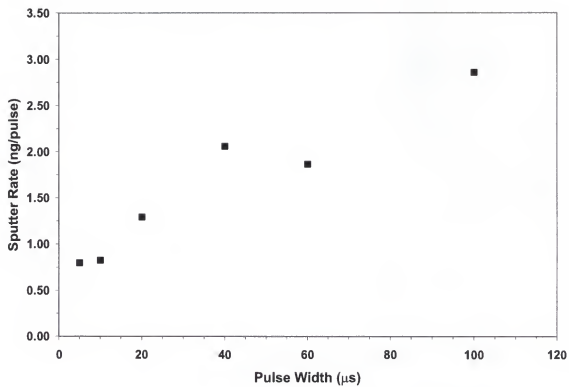


Figure 4-5. Effect of pulse width on sputter rate (brass sample, 1.4 kV, 3 torr Ar, 400 Hz pulse frequency, 20min.).

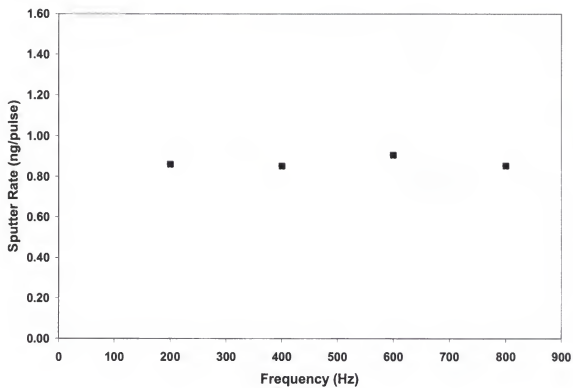


Figure 4-6. Effect of pulse frequency on sputter rate (brass sample, 1.4 kV, 3 torr Ar, 10 μ s pulse width, 20 min.).

sample with longer analysis times. However, if the increasing depth should affect net diffusion of atoms from the surface, then calculated sputter rates could be affected. Figure 4-7 shows a plot of the sputtering rate dependence on time using a brass sample consisting of 70% copper and 30% zinc (Alfa AESAR, Ward Hill, Massachusetts, USA). No significant change in sputtering rate with increased analysis times is observed, as shown in this figure. Uncertainty measurements were obtained through triplicate analysis for each sputter time and plotting the standard deviations. It is possible that longer analysis times could degrade the quality of the crater profiles due to differential sputtering of the crater sides with respect to the bottom of the crater. For the current study a fixed time of 40 minutes has been used for all sputter data studies. Also, it should be noted that other sample types, such as pure copper and pure zinc foils, have been shown to yield similar parametric trends as those reported above for a brass thin film.⁹⁰

Sputtering Rates and Penetration Rates

The net sample sputter rate q (ng/pulse), as described in Chapter 2, can be calculated for a GD using:

$$q = \Delta W / (t * f) = \Delta W / p_N \quad (\text{Eqn. 4-1})$$

where ΔW (ng) is the amount of sample lost due to net sputtering, t (s) is the sputter time, f (Hz) is the pulse frequency. If sputtering time is measured, the first part of Equation 4-1 is used in which the number of pulses must be calculated. However, a pulse counter can be used to directly monitor the number of pulses (p_N - pulses) from the power supply, making the second part of Equation 4-1 applicable. Furthermore,

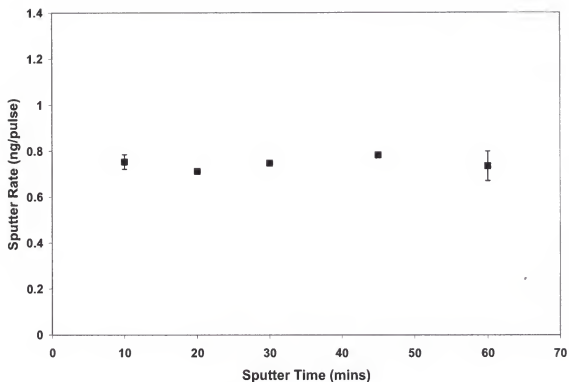


Figure 4-7. Sputtering rate dependence as a function of total sputtering time (brass sample, 1.4 kV, 3 torr Ar, 10 μ s pulse width, 400 Hz pulse frequency). Error analysis (standard deviation) obtained through triplicate measurements.

using a pulse counter should yield a more accurate and precise sputtering rate due to limitations of measuring sputter time, since some fractional time in each pulse is required for the plasma to stabilize, making it difficult to measure the “true” sputter time.

To obtain a quantitative depth profile it is necessary to determine concentration as a function of depth. This can be accomplished by converting the sputtering rate of the sample to its penetration rate (w - nm), which is the amount of sample eroded per unit time and is dependent on the density of the sample. As described by Boumans,⁶¹ the penetration rate has units of distance per time ($\mu\text{m}/\text{sec}$). However, in the present study, the units are changed to distance per pulse (nm/pulse) to account for the use of a pulsed glow discharge source. The penetration rate can be shown quantitatively by:

$$w = q / (A * \rho) \quad (\text{Eqn. 4-2})$$

where ρ (g/cm^3) is the density of the target material, and A (cm^2) is the sputtered area, πr^2 , where r (cm) is the radius of the Grimm anode (typically 2 mm). Sputtering rate values and corresponding penetration rates for the various pure elements studied in this project can be found in Table 4-1. The values in this table are based on three trial runs with the standard deviation included to show uncertainty.

As seen in Equation 4-2, the penetration rate has a direct dependence on the density of the material being analyzed. This dependence does not present a problem for determining the penetration rate of pure elements. However, determining the sputtering depth of a multi-layered sample presents a concern. As one layer of the sample is sputtered away and the next layer is exposed, the

Table 4-1. Sputtering rates and corresponding penetration rates for thin films of brass and various pure elements. Based on three sample runs with the standard deviation included to show uncertainty. Sputtering conditions: 1400 V, 3 torr, 10 μ s pulse width, 400 Hz frequency, and a sputtering time of 40 min.

Element	Sputtering rate (q) / ng per pulse	Penetration rate (w) / nm per pulse
Brass	0.83 ± 0.01	0.0078 ± 0.0001
Iron	0.12 ± 0.02	0.0012 ± 0.0002
Nickel	0.268 ± 0.006	0.00239 ± 0.00005
Copper	0.67 ± 0.01	0.0059 ± 0.0001
Zinc	1.74 ± 0.01	0.0194 ± 0.0001
Silver	2.06 ± 0.03	0.0157 ± 0.0002

interface involves a change in density of the pure element comprising the first layer to that of the density of a second layer, along with changes in sputtering rate and concentration of the two elements. If the transition from one layer to the next were instantaneous, this concern would not exist. However, in the interface between layers, sample material from both layers is being removed, and the sample will take on multi-element characteristics, rather than acting as separate pure layers. Hence, a quantification method must take into account this interface concern.

Calibration Curve Correction

A variety of bulk reference standards is used to quantify a depth profile because large concentration ranges in different matrices are typically required. For example, when analyzing a layered sample, the element of interest must be calibrated over the full concentration (0 to 100%), because of the concentration range created during the transition. However, sputter rates are unique due to matrix differences, producing a different calibration curve for each family of materials. To correct for this, the sputter rate for each standard can be used to correct for inherent differences, permitting a single calibration curve. The method of quantification described in this dissertation requires accounting for these sputtering rate differences, which makes this correction step crucial to the overall quantification method.

An intensity-concentration diagram for copper (copper II 219.227 nm emission) is shown in Figure 4-8. The copper II 219.227 nm emission line was chosen due to the self-absorbing nature of the copper I 327.396 atom line. Figure 4-

8 is a calibration curve for 12 copper samples, 8 in an iron matrix, 3 in a zinc matrix, and one a pure copper sample. A non-linear response of copper intensities is shown, resulting from matrix-dependent sputtering rates. The resultant calibration slope (Figure 4-8) would yield erroneous copper concentrations based on the uncorrected intensities. The quantification method in this dissertation relies on correction of these intensity differences.

The procedure used for correcting intensity differences due to varying sputtering rates has been previously reported,¹¹⁵ and requires the use of a variety of calibration samples, each having different sputtering rates. In this previous publication, which is based on the Swedish Institute of Metals Research (SIMR) calibration model (described below), the intensity correction relies on determining the sputtering rates of an iron alloy. In the current research, intensity correction employs the sputtering rate of pure iron, which can be directly determined through weight loss measurements. As long as the calibration for each element is normalized to the same reference sputtering rate, the reference sample (i.e., pure iron or an iron alloy) will not result in a discrepancy. Intensity correction in the current research is done by multiplying the measured intensities of each calibration sample by a factor equal to the ratio of the sputtering rate of the reference material to that of the sample. Mathematically this relationship is given by:

$$I_{norm} = I * (q_{ref} / q_s) \quad (\text{Eqn. 4-3})$$

where I_{norm} is the normalized intensity, I is the "raw" intensity, and q_{ref} and q_s refer to the sputtering rates of the reference material (e.g., iron) and sample, respectively.

Figure 4-9 shows a sputter rate-corrected calibration plot, using the results of Equation 4-3, for the non-linear copper calibration curve shown previously in Figure 4-8. Using this corrected calibration curve affords better estimations of unknown copper concentrations based on intensity measurements. A similar study was done using nickel alloys, with comparable results being obtained, as shown in the uncorrected calibration curve of Figure 4-10 and sputter-rate corrected curve of Figure 4-11, respectively. A marked advantage of this calibration procedure lies in the fact that bulk standard materials can be used, not requiring high-cost, less readily available layered samples. Also, the analytical procedure is simplified by only requiring one reference sputtering rate to be determined, rather than multiple reference material sputtering rates. After a linear calibration curve is obtained, the information can be used for the subsequent quantification procedure.

Quantification Overview

When performing depth analysis, the data obtained typically represents intensity-time profiles. However, the information desired is in the form of depth-concentration profiles since more detailed information can be extracted from such a plot. An example of this added information is that, for a given sample, the concentration of a thin layer in the sample can be monitored at varying depths of the sample. The time to depth conversion procedure involves knowledge of the sputtering rates for each element and calibration of the instrument from a series of standard samples. This qualitative to quantitative conversion gives a better estimation of the true depth profile.

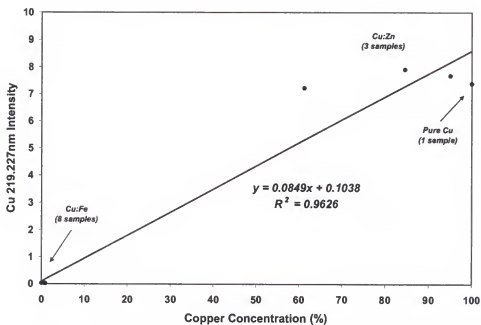


Figure 4-8. Plot of uncorrected calibrated data for various copper samples (Cu 219.227 nm emission) in different matrices.

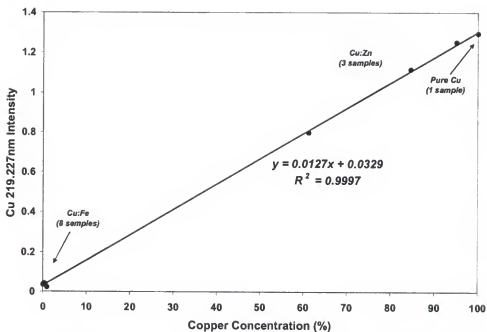


Figure 4-9. Plot of sputter rate-corrected copper calibration data of Figure 4-8.

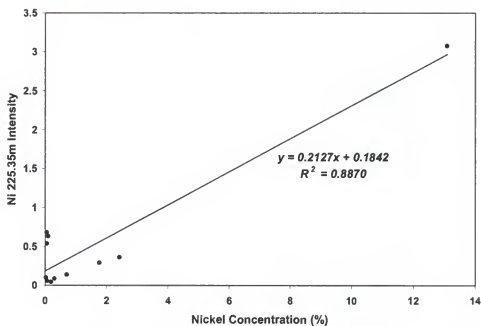


Figure 4-10. Plot of uncorrected calibrated data for various nickel samples (Ni 225.35 nm emission) in different matrices.

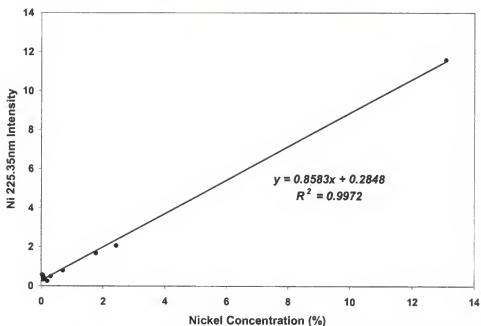


Figure 4-11. Plot of sputter rate-corrected nickel calibration data of Figure 4-10.

Two prominent quantification techniques have been described in the literature; the IRSID (Institut de la Recherche Siderurgie) method and the SIMR (Swedish Institute for Metals Research) method. The IRSID method, first introduced by Pons-Corbeau in France,^{116,117} uses the emission yield concept as a basis for quantification of depth profiles. This method relies on the assumption that the integrated intensity from one element is proportional to the sputtered mass of that element, which in turn implies that the emission yield, defined as the emitted light per unit sputtered mass of an element, is independent of the sample matrix provided that the excitation conditions remain at least nearly constant.⁸⁶ Most researchers now believe that this assumption is valid at least to a first approximation.

Another quantification method was developed by SIMR.¹¹⁵ Unlike the IRSID method, the SIMR quantification method is not directly based on the emission yield concept. Rather, it is based on a sputtering rate-intensity proportionality. Essentially, the difference between the quantification techniques lies in the fact that in the SIMR method, the concentration, instead of the sputtered mass of each element, appears in the calibration function, making the SIMR method similar to standard techniques for bulk analysis. Measurements are based on a calibration at pre-determined levels of voltage and current, referred to as the reference excitation condition. One of the main goals of the SIMR quantification method is a calibration procedure that resembles a standard bulk analytical method.

In both quantification methods a steady-state dc glow discharge was employed. However, the pulsed glow discharge in our work adds two additional parameters, pulse width and pulse frequency, that offer additional control over the

sputtering process. As described previously, extension of the pulsed technique to depth profiling should increase performance by allowing thin sample layers of a few atomic distances to be measured more easily by selecting a slower sample removal rate. Furthermore, reduced sample heating by the pulsed discharge compared to dc operation allows certain thin layer samples to be analyzed. Since these two additional parameters are inherent in the pulsed glow discharge, the quantification method must be modified to incorporate them. The quantification method chosen for this research is based on the SIMR method, though it should be noted that slight modifications to this model have been made, such as the use of different reference sputtering rates.

Principle of Quantification

The first step in the quantification method, after acquiring sputtering rates and calibrating the instrument, is to collect a raw intensity plot from the layered sample. An intensity-time plot of a 50 nm layer of copper deposited on a steel substrate can be seen in Figure 4-12. This plot shows the intensity of the copper II 219.227 nm ion line, as well as the Fe I 371.993 atom line. The data in this plot only show intensity as a function of time. Therefore, quantitative results, such as depth, cannot be extracted from the plot as it is shown.

The next step in the quantification method involves determining the selected elements' concentrations. This is done by converting the intensity measurements shown in Figure 4-12 to concentrations using the sputter rate-corrected calibration

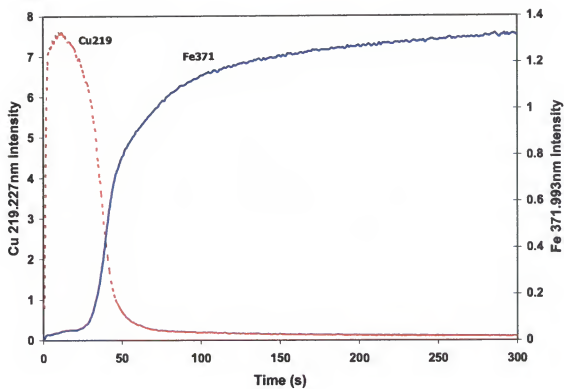


Figure 4-12. Intensity-time plot of a 50 nm layer of copper deposited on a steel substrate.

curve of the bulk standards shown in Figure 4-9. These concentrations are then normalized to 100%, as shown in Figure 4-13.

The third step in the method is to determine the composite sputter rate and composite density as a function of time from the normalized concentrations. The composite sputter rate is simply a summation of each element's percent contribution of the reference material's sputtering rate over all the elements in the sample. Similarly, the composite density is a summation of each element's percent contribution of the reference material's density over all elements in the sample.

After the composite sputtering rates and composite densities have been determined, they can be used in collaboration with the previously determined sputter area and sputter time to obtain the penetration depth (d). The sputtered depth increment (Δd_i) at a given point in time can be obtained by multiplying the penetration rate (Equation 4-2) at this point by the number of pulses per sampling point:

$$\Delta d_i = w_i * p_N \quad (\text{Eqn. 4-4})$$

where, Δd_i (nm) is the sputtered depth increment, w_i (nm/pulse) is the penetration rate at that point, and p_N (pulses) is the number of pulses per sampling point. The overall penetration depth (d) can be obtained by summing all sputtered depth increments (Eqn. 4-4) for each sampling point over the entire sampling range:

$$d = \sum_{i=0}^n \Delta d_i \quad (\text{Eqn. 4-5})$$

Based on Equations 4-4 and 4-5, the time axis (s) of Figure 4-13 can be converted to depth (nm) for the entire sampling depth (150 nm). Therefore, the final

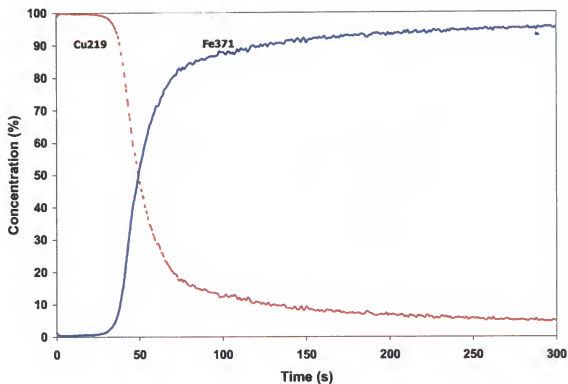


Figure 4-13. Normalized concentration-time plot from Figure 4-12 of a 50 nm copper layer on steel base.

form of the data now reveals concentration as a function of depth. Figure 4-14 illustrates the quantified result of the copper layer on a steel substrate shown originally in Figure 4-12 as a raw intensity-time plot. Experimental results obtained using the quantitative method predict a depth of 54 ± 2.1 nm, which is in accord with the nominal depth of copper reported for this sample. Furthermore, concentration-depth plots provide more valuable information than the intensity-time plots, since the former allows the concentration of multiple layers to be monitored as the sample is being sputtered.

Additional samples of copper deposited on steel, varying only in copper deposition depth, were quantified in single measurement fashion as well. Other nominal depths analyzed include layers of 150 nm, 250 nm, and 500 nm of copper. Based on the quantification method, the estimated thickness for each layer is 148 nm, 254 nm, and 519 nm, respectively, indicating that the method can be applied to a range of foils. It should be noted that one sample was prepared at the extreme limit of deposition confidence, with a nominal copper depth of approximately 10 nm, for which our model predicted a copper depth of 19 nm. At these layered depths, uncertainties in the uniformity of deposition must also be considered.

The quantification technique was also extended to multiple layered samples. Figure 4-15 shows an intensity-time plot of a $1.3 \mu\text{m}$ zinc layer and a $1.6 \mu\text{m}$ nickel layer, respectively, deposited on a steel substrate. Using the sputter-rate corrected calibration curve shown in Figure 4-11, the intensity-time plot of Figure 4-15 was quantified in a single measurement fashion. The quantified result of this sample is shown in Figure 4-16.

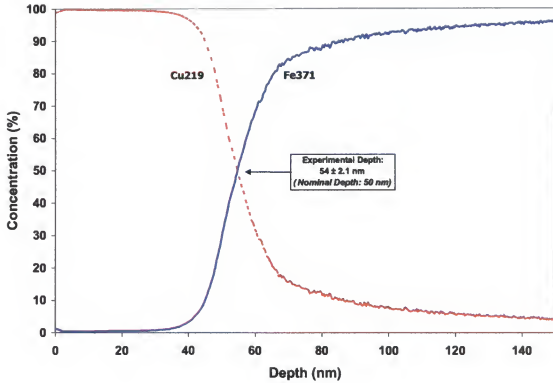


Figure 4-14. Concentration-depth plot from Figure 4-13 of a 50 nm copper layer on steel base.

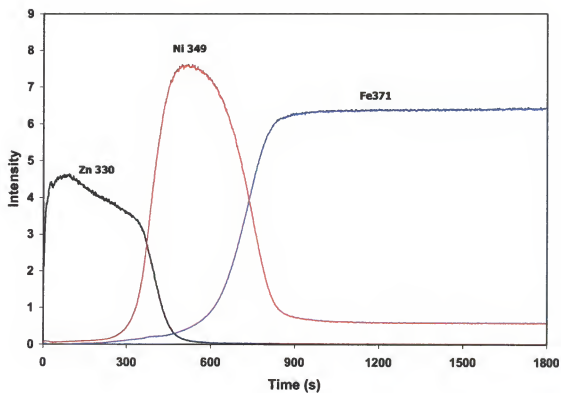


Figure 4-15. Intensity-time plot of a 1.3 μm layer of zinc and 1.6 μm layer of nickel deposited on a steel substrate.

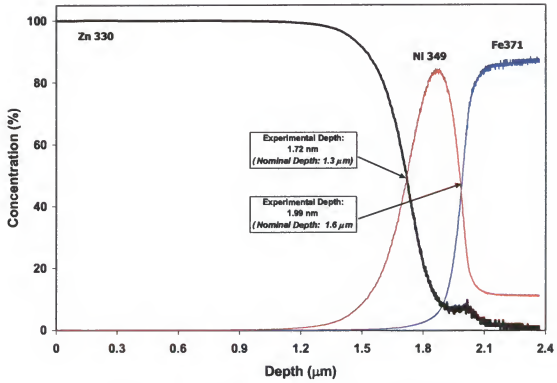


Figure 4-16. Concentration-depth plot from Figure 4-15.

Concluding Remarks

This chapter has shown the application of the microsecond pulsed glow discharge for quantitative depth profiling using a method similar to that developed for dc depth profiling. Using the pulsed glow discharge provides better control of the removal rate due to the added parameters of pulse width and pulse frequency. The method was tested by performing a quantitative conversion of layers including 10, 50, 150, 250, and 500 nm of copper deposited on a steel substrate. Results indicate that the quantitative method gave a copper deposition depth in accord with the nominal depths, with the exception of the 10 nm copper layer. This outlier could result from a limitation in the quantification method, as well as an error in the uniform deposition of such a small amount of sample. A multiple layered sample, consisting of a thin zinc and nickel layer deposited on a steel substrate, was also quantified with this technique. A computer program for computation would be an asset for the quantification of multiple layers. Also, the sputtering rates and penetration rates for additional elements should be added to our database in order to quantify more complex thin layer samples.

CHAPTER 5

INTRODUCTION TO THE GRIMM-TYPE GLOW DISCHARGE AXIAL TIME-OF-FLIGHT MASS SPECTROMETER SYSTEM

Introduction

The ability of the glow discharge (GD) source to generate an analyte population directly from solid samples makes it an attractive ion source for elemental mass spectrometry. The GD can readily form an ion population representative of the sample composition, and the mass spectrometer (MS) can convert these sample ions into an information-rich mass spectrum. Harrison and Magee first examined the feasibility of GDMS in the mid-1970s by coupling a direct current GD source to a quadrupole MS.¹¹⁸ Today, the GD has been interfaced to all types of mass spectrometers – each providing unique advantages. Since our initial foray with quadrupole GDMS we have shifted our focus to another mass analyzer – time-of-flight mass spectrometry (TOFMS). For almost a decade now, our group has been actively evaluating TOFMS for GD applications. We have discovered that the microsecond pulsed GD source provides special opportunities for TOFMS applications, which will be described throughout this chapter.

Our first GD-TOFMS system entailed a probe-type GD source (e.g., direct insertion probe) that was orthogonally interfaced to an in-house designed TOFMS.^{14,37,119} We have since obtained a commercial axial TOFMS, which we have interfaced to a microsecond pulsed Grimm-type GD source. This latter GD-TOFMS

system will be the focus of the remainder of this dissertation. This chapter will first describe basic operating principles and design considerations of TOFMS. The next section will describe details of the in-house designed GD source and commercial TOFMS, and will then conclude with a discussion of the operating performance of our GD-TOFMS.

Time-of-Flight Mass Spectrometry Background

Operating Characteristics

The time-of-flight mass spectrometer (TOFMS) has become a valuable tool for inorganic mass analysis. Numerous TOF applications have been shown using the inductively coupled plasma (ICP)^{120,121} and GD source,^{14,37} owing to the advantages of TOFMS for atomic analysis.

For inorganic analysis, the largest benefit of the TOFMS is its ability to determine simultaneously all mass-to-charge (m/z) values within a mass range of interest. This is accomplished without moving parts or scanning fields, which avoids limitations of sequentially scanning instruments (e.g., quadrupole MS). A TOFMS does not record all masses truly *simultaneously*, since a finite time difference (e.g., ns) separates the detection of adjacent masses. However, all masses are sampled into the mass spectrometer simultaneously and an entire mass spectrum is generated from each injection pulse.

The simultaneous sampling of TOFMS gives it unparalleled analysis speed, producing full mass spectra in tens to hundreds of microseconds. This rapid duty cycle generates thousands of complete mass spectra every second, which demands

powerful, high-speed electronics. Averaging these spectra (i.e., integrating) can improve the signal-to-noise ratio (S/N).

Also unique to TOFMS is its theoretically unlimited mass range, which has become invaluable for the analysis of large biomolecules, such as proteins. Since ions are separated based on flight time, the detection of these ions should theoretically be unlimited. However, electronics limit the number of events that can be recorded in time, placing a disclaimer on this advertised advantage. It should be noted that this unlimited mass range of the TOFMS is not utilized in inorganic analyses, which generally only require mass ranges up to 300 AMUs.

Basic Principles

A TOFMS operates on the basis of a 'dispersion-in-time' principle.¹²² Ions produced by the source (e.g., GD) are accelerated by an electric field pulse, typically 10^3 to 10^4 V. The ions are accelerated to an energy that is governed by the fundamental kinetic energy (KE) equation:

$$KE = \frac{1}{2} mv^2 \quad (\text{Eqn. 5-1})$$

where, m (g) is the mass of an object in motion (e.g., ion), and v (m/s^2) is the velocity of that object. Since the ions are ideally accelerated to the same KE, they will have a different velocity as a function of their mass. Assuming the ions achieve the same KE, they can be separated according to their velocity, which is characteristic of the mass-to-charge ratio (m/z). This velocity can be shown mathematically by:

$$v = (2KE / m)^{1/2} \quad (\text{Eqn. 5-2})$$

which is a rearrangement of Equation 5-1. A mass spectrum is compiled by measuring the time it takes for an ion to traverse a flight path within the TOFMS. Low-mass ions will reach the detector before high-mass ones, assuming both are accelerated with the same KE. This mass separation principle (i.e., dispersion-in-time) is illustrated in Figure 5-1.

The time required for an ion of mass (m) to travel the path length, L (m), can be calculated from:

$$t = (m / 2zeV)^{1/2} * L \quad (\text{Eqn. 5-3})$$

where z is the number of charges on the ion, e (C) is the charge of an electron, and V (V) is the accelerating voltage. The time required for ions to traverse the flight path is generally between 10,000 ns for low-mass elements (e.g., carbon) and approximately 45,000 ns for high-mass elements (e.g., lead). A flight time spectrum is shown in Figure 5-2, which represents intermediate flight times corresponding to tin. A mass spectrum is obtained by converting the flight time to m/z and plotting ion intensity versus m/z , as shown in Figure 5-3. Worth noting is that ion flight times do not show a linear relationship with m/z , but rather a squared dependence, as shown in Figure 5-4

To produce a mass spectrum based on flight time, all ions must enter the acceleration region at nearly the same time. This transient nature by which a TOFMS accepts ions is an important characteristic, and is a special opportunity for our microsecond pulsed GD source. As the sample is atomized and ionized by successive pulses of the GD, ion packets are sampled into the TOFMS, providing

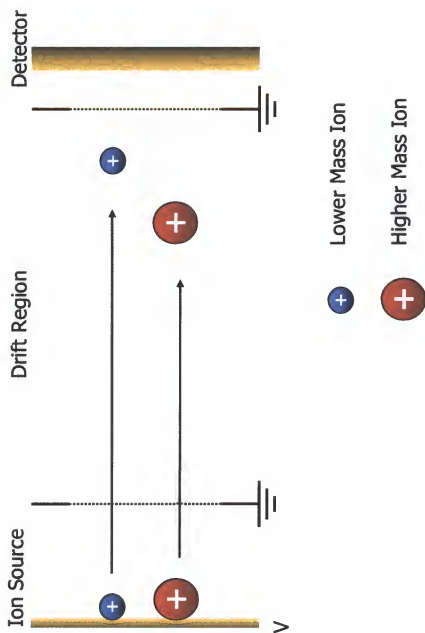


Figure 5-1. Dispersion-in-time principle of the time-of-flight mass spectrometer.¹²²

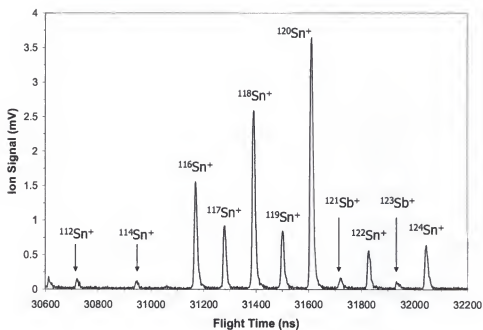


Figure 5-2. Spectrum showing ion intensity versus flight time for a brass sample. Operating conditions: 2.0 kV, 1.3 mA, 3.6 torr, 200 mL/min, 400 Hz, 20 μ s PW, -2500 V detector voltage, 3 s integration time. Sample: NIST 494 brass standard.

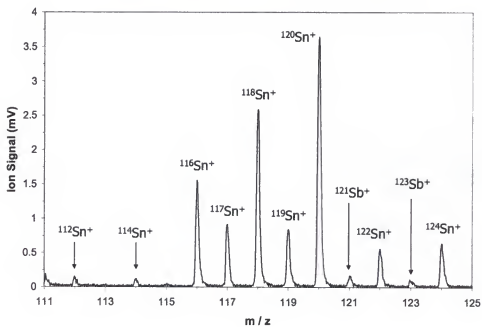


Figure 5-3. Mass spectrum as converted from the ion intensity versus flight time spectrum in Figure 5-2. Operating conditions as in Figure 5-2.

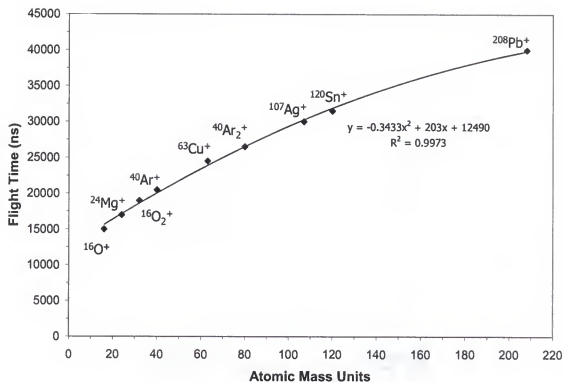


Figure 5-4. Non-linear dependence of flight time and mass. Mass spectrometer operating conditions as in Table 5-1.

maximum ion sampling efficiency. Optimization of these pulse timing events (e.g., delay time) allows time resolved measurements, as described in Chapter 3.

Design Considerations

Sampling geometry. Two geometries have been employed to introduce ions into a TOF: axial and orthogonal.^{14,123} Both of these configurations use a pulsed extraction field to sample ions from the source and accelerate them into the flight tube. The drift tube of a TOFMS in an axial arrangement is located coaxial with the incoming ion beam. Ions are accelerated into the flight tube by applying a rapid sequence of positive and negative voltages within a modulation region. The operation of the axial geometry, which is employed in our TOFMS, will be described later in this chapter.

The other TOFMS configuration, an orthogonal geometry, samples ions from the plasma into the flight tube at a right angle. A transient voltage applied to a repelling region accelerates the ions into the flight tube, as shown previously in Chapter 3 (see Figure 3-8).

Ion optics. Efficient ion transport is crucial to the success of a TOFMS analysis. Focusing optics, such as Einzel lenses, are used to direct ions in the proper path for maximum ion throughput. Early TOF instruments employed ion electrodes consisting of tiny wire grids for ion focusing. Voltages were placed across these grids, thereby focusing the ions into a tight profile. However, two main factors, intricate machining and transmission losses, often compromised the use of

these grids.¹²⁴ To avoid these limitations, gridless ion optics have been developed, which use a series of ring electrodes at escalating voltages to focus ions.

The reflectron is an ion focusing optic in TOFMS that deserves special attention. This device was first proposed by Mamyrin and colleagues in the 1970s, and has been invaluable to TOF research since its inception.¹²⁵ Essentially, this device affords better resolution through compensation for different flight times of ions with somewhat dissimilar kinetic energies. Figure 5-5 is an illustration of a TOF instrument employing the reflectron principle. After traversing the first stage of the flight tube, ions enter a retarding field and are reflected through a second stage of the flight tube. An ion with a higher energy will penetrate the retarding field more deeply and will spend more time in this field, allowing it to approximate the velocity of a slower ion (of the same mass) so that both reach the detector nearly simultaneously.

Detector. Minimal mass bias, non-stringent vacuum requirements, resistance to poisoning, and long lifetime are a few important characteristics of general MS detectors. In addition to these, a detector employed in TOFMS must possess excellent temporal response in order to distinguish between ion flight times that may vary by only nanoseconds.¹²⁴

Two general types of detectors have exhibited the criteria listed above, including the microchannel plate (MCP) and electron multiplier. For many TOFMS applications, the MCP is the detector of choice because of its large active area and high gain. The MCP also has excellent response times, routinely on the order of

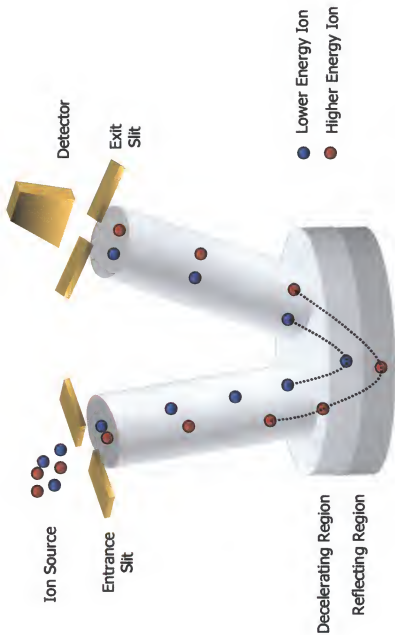


Figure 5-5. Time-of-flight mass spectrometer showing reflectron focusing.

picoseconds.¹²⁴ Enhanced ion gains (e.g., 10^6) can be achieved by employing a chevron arrangement, in which two MCPs are oriented back-to-back. For example, the high field strengths within the channels of the MCP can ionize residual gas molecules in the vacuum chamber, creating an avalanche effect that can destroy portions of the MCP. Also, despite their excellent response to single ion collections, MCPs have high resistances that prevent them from recharging quickly. Often, this recharge time is in the millisecond regime,¹²⁴ which limits the gain available after detection of an intense mass-spectral peak (e.g., matrix signal).

The other type of detector typically employed in TOMFS applications is the discrete-dynode electron multiplier (DDEM). The dynamic range, stability, and single-ion detection capability of the DDEM are similar to those inherent with the MCP. However, DDEM detectors do not suffer from severe saturation problems and extended recharging times that plague their MCP counterparts. DDEMs, though, do not possess the large active areas that are available in MCP devices.

The Grimm-type Glow Discharge Source and Renaissance Time-of-Flight Mass Spectrometer

This section describes the source and mass spectrometer employed in the projects described throughout the remainder of this dissertation. The first section will describe the initial design of the Grimm-type GD source, followed by characteristics and operation of the TOFMS. The chapter will conclude with a brief discussion of the basic operation and performance of this GD-TOFMS.

Grimm-type Glow Discharge Source

The source chosen for these studies was the Grimm-type GD configuration, which was described in Chapter 3. Even though the Grimm configuration has enjoyed success as a source for atomic emission measurements, little research has been done to establish this configuration as a viable source for mass spectrometry. The lack of application is mainly attributed to the inherent ion transport difficulty for a Grimm GD source and TOFMS. Despite this limitation, we have decided to forego the use of a conventional probe-type source (e.g., DIP), and have opted to evaluate the Grimm design as a TOFMS source.

Source description. A schematic and photo of the Grimm-type source is shown in Figure 5-6 and Figure 5-7, respectively. The configuration shown in Figure 5-6 was an initial design, though improved iterations have since evolved, which will be described in Chapter 6. The cathode block and anode, machined of brass, are isolated from one another by a Macor plate. The tip of the cylindrical anode (4 mm i.d.) extends to approximately 0.25 mm from the sample surface. A flat sample is placed on the cathode block and sealed via an O-ring. A stainless steel sampling ring is mounted coaxially outside the anode. The skimmer cone, also machined of stainless steel, has an internal orifice diameter of 0.7 mm and a total sampling distance (i.e., source-to-cone orifice) of approximately 13 mm. All source components except the cathode block are maintained at ground potential.

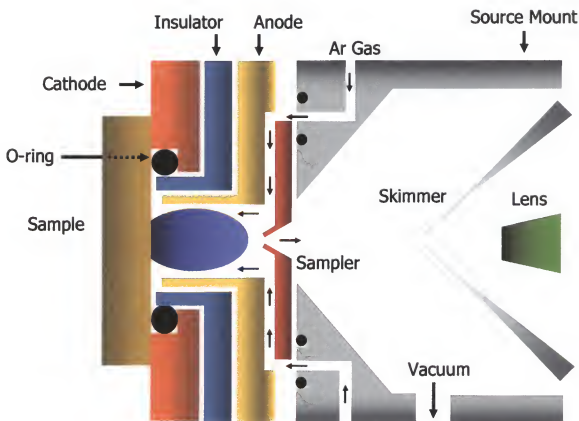


Figure 5-6. Schematic of the Grimm-type source coupled to the Renaissance time-of-flight mass spectrometer.

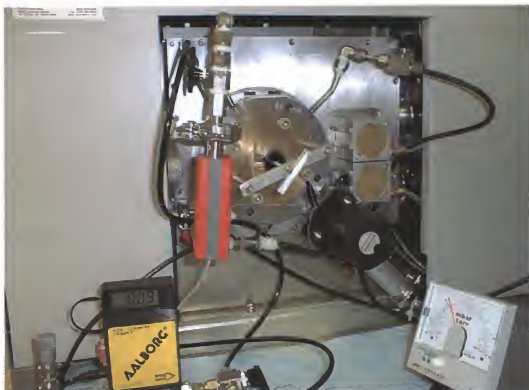


Figure 5-7. Photo of the microsecond pulsed Grimm-type glow discharge source.

Source operation. Power was supplied to the source using a high-voltage pulsed power supply (Model: M3k-20, Instrument Research Company, Maryland, USA), which allowed changes of the pulse width and pulse frequency. Voltage and current profiles of the plasma, displayed on a 500 MHz digital oscilloscope (Model: TDS-724D, Tektronix, Inc., Beaverton, Oregon, USA), allow peak voltage and current measurement and afford plasma stability monitoring. The average voltage and current values were displayed directly on the power supply.

A 3.9 L/s mechanical pump (Model: RV12, BOC Edwards, Wilmington, Massachusetts, USA) was the auxiliary pump for the source. Ultra-high purity (99.9999%) argon was used as the plasma gas (The BOC Group Inc., Murray Hill, New Jersey, USA) for all experiments. The flow rate of the plasma gas was controlled *via* a needle valve (Model SS-22RS4, Whitey Company, Highland Heights, Ohio, USA) and was measured with a 0 - 500 mL/min gas flow meter (Model: GFM171, Aalborg, Orangeburg, New York, USA). The source pressure was measured with a Pirani gauge (Model: APG-M-NW16, BOC Edwards, Wilmington, Massachusetts, USA) and shown on an active gauge display (Model: AGD, BOC Edwards, Wilmington, Massachusetts, USA). Installation of a diaphragm valve (Model: SP25K, BOC Edwards, Wilmington, Massachusetts, USA) in the vacuum line of the first stage allowed independent control of flow rate and pressure.

Renaissance Time-of-Flight Mass Spectrometer

The mass spectrometer employed in these studies is a commercial time-of-flight instrument (Renaissance, LECO Corporation, St. Joseph, MI, USA), which is shown in Figure 5-8. The instrument was developed for inductively coupled plasma (ICP) measurements, but was modified to accept our in-house designed GD source. The operation of this spectrometer, as well as the modifications made, will be described in the next section.

Mass spectrometer description. A schematic of the major components within the TOFMS is shown in Figure 5-9. Ions are formed within the source (Figure 5-6) and are extracted by the first ion lens of the mass spectrometer (Figure 5-9). The second ion lens serves to transfer ions to the modulation region of the TOFMS. The modulation optic is a cylinder responsible for selecting an ion packet (nominally 1.5 cm long) from the ions introduced into the spectrometer. The selected ion packet is then transferred to the acceleration region of the TOFMS by applying a negative voltage to the modulation electrode. After a packet of ions is selected, it is accelerated by switching the modulation to a positive potential, which prevents other ions from entering the drift region. The selected ion packet then travels to the repeller electrode, where a positive voltage is applied and remains for a fixed time (nominally 1 μ s), which sends the ions into the dc acceleration region of the TOFMS. This acceleration region gives the ions their final kinetic energy. After being accelerated, the ions are focused by an Einzel lens and then horizontally



Figure 5-8. Photo of the microsecond pulsed Grimm-type glow discharge and time-of-flight mass spectrometer.

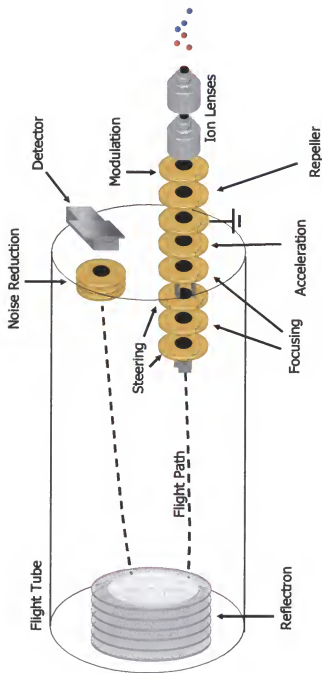


Figure 5-9. Schematic of the Renaissance time-of-flight mass spectrometer.

focused by the first steering plate (i.e., Y-steering plate). The ions are then are focused by a second Einzel lens, and then focused vertically by an X-steering plate.

Upon reaching the X-steering plate, ions that may saturate the detector can be removed by applying a time-dependent potential to the X-steering plate at a certain delay with respect to the repeller pulse. Those ions between the plates at the time of the pulse will be accelerated normal to the flight path, removing them from the flight path. This selective removal is beneficial when dealing with a large number of matrix ion species. Indeed, these deflecting pulse voltages must have fast rise and fall times ($<10 - 20$ ns) to allow unimpeded passage of the previous and subsequent masses.¹²⁴

After traversing the flight tube, ions encounter a reflectron, which is utilized to lengthen the flight of the ions and focus their energy spreads. After reflection, the ions begin their final trek towards the detector. The ions must pass a noise reducing grid prior to detection, which consists of a small positive potential for discrimination against low energy ion noises. Ions that penetrate this noise reduction region are finally detected by a discrete dynode electron multiplier (EPT Scientific, Austin, Texas, USA).

Mass spectrometer modifications. The software (LECO Renaissance version 1.16, LECO Corporation, St. Joseph, MI, USA) provides control of the mass spectrometer conditions and allows real-time monitoring of the pressure within the three mass spectrometer stages. The software likewise controls isolation valves that protect the high vacuum system from the atmosphere during sample interchange, as

shown in the vacuum diagram in Figure 5-10. Since this instrument was originally designed for ICP measurements, the software had to be modified to accept the microsecond pulses from our GD source. Also, a repeller delay option was added to allow the ion sampling time to be altered so that temporal resolution measurements could be achieved.

Overall Operation

A schematic of the source and mass spectrometer components is shown in Figure 5-11. The Renaissance TOFMS triggers the microsecond pulsed power supply, which in turn applies a transient voltage to the Grimm source. A digital oscilloscope synchronized with the pulsed power supply allowed plasma stability monitoring. After the ions are created within the source, they traverse the flight tube and are detected by the EEDM. The electrical signal output from the detector is converted to a mass spectrum and displayed on a personal computer (Dell Computer Corporation, Round Rock, Texas, USA). Typical operating conditions of the system are shown in Table 1.

Performance of the Glow Discharge Time-of-Flight Mass Spectrometer

After successfully coupling the Grimm-type source to the TOFMS, the operating performance of the system was assessed. This section will detail the critical factors of the TOF instrument, such as resolving power and linear dynamic range.

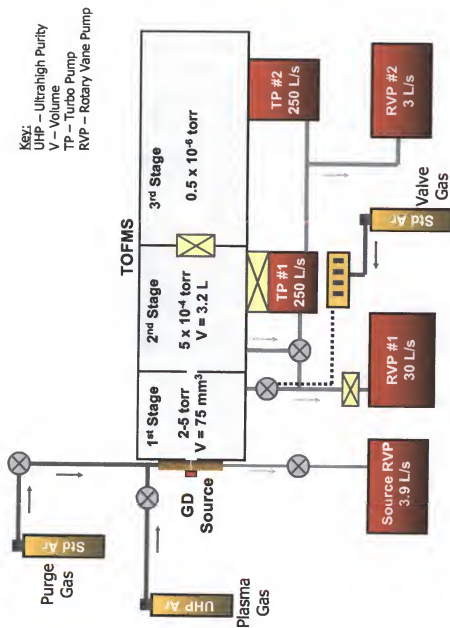


Figure 5-10. Schematic of the vacuum system of the time-of-flight mass spectrometer.

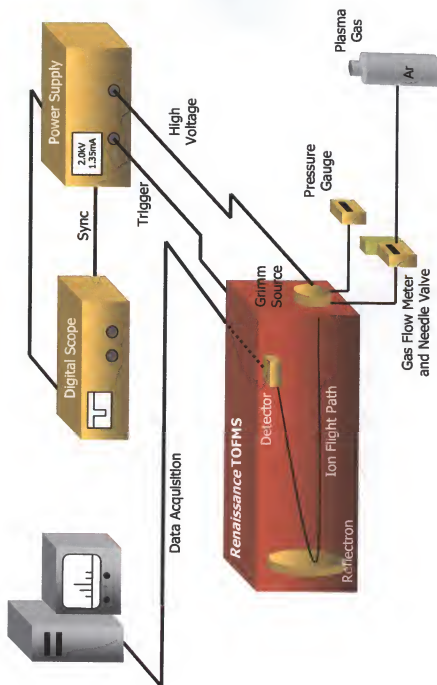


Figure 5-11. Schematic of the glow discharge time-of-flight mass spectrometer and other components.

Table 5-1. Typical operating conditions of the glow discharge time-of-flight mass spectrometer.

Microsecond Pulsed Glow Discharge Source

Pulse Magnitude	1.5 – 2.0 kV
Pulse Width	10 – 20 μ s
Pulse Frequency	400 Hz
Source Pressure	2.5 – 5.0 torr Ar
Average Current	1.2 – 1.8 mA
Flow Rate	50 – 250 mL / min

Time-of-Flight Mass Spectrometer

Ion Lens 1	-500 V
Ion Lens 2	-550 V
Flight Tube	-1500 V
Reflectron Low	210 V
Reflectron High	1550 V
Noise Reduction	500 V
X-Steering	-1490 V
Y-Steering	-1630 V
Einzel Lens 1	-1340 V
Einzel Lens 2	-840 V
Modulation Positive	120 V
Modulation Negative	-133 V
Modulation Delay	40 μ s
Modulation Pulse Width	5 μ s
Repeller Bias	0 – -4 V
Repeller Pulse	1000 V
Repeller Pulse Width	1.2 μ s
Third Stage Pressure	0.4 – 0.9 μ torr
Integration Time	1 – 3 s

Ion Detection

Two detection modes are employed in TOFMS: analog and digital. In analog mode, the detected ion signal is collected and output directly as a voltage. In the other mode, termed digital counting, individual voltage pulses corresponding to ion signal are counted and converted into ion counts (i.e., number of ions striking the detector) per second. In most applications, the analog detection mode is used for monitoring high concentration (e.g., matrix) species. Integration in this mode simply averages multiple spectra for a specified amount of time, which can improve the S/N. Digital counting mode is generally used for trace analysis, in which the spectra are summed rather than averaged, which can yield enhanced ion signals and improved detection limits.

The unmodified, commercial TOFMS with the ICP source was capable of detecting ions in either of these detection modes. However, after converting the system to pulsed operation, the digital counting mode did not function properly. This can be illustrated by comparing two identical spectra, one collected in analog mode (Figure 5-12) and the other digitally converted and displayed (Figure 5-13). While the mass spectrum collected in analog mode exhibits well-defined peaks, the corresponding ion counting mass spectrum shows distorted peak shapes and incorrect isotopic ratios. The digital counting problem originates because of the low duty cycle of our pulsed GD system. The original instrument, operated with an ICP source, collects spectra at a frequency of 20 kHz. This means that 20,000 individual mass spectra are collected and averaged every second. Using our pulsed GD system, the spectral frequency is dictated by the pulse frequency of our discharge

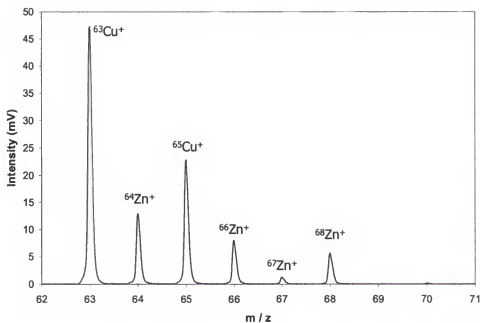


Figure 5-12. Mass spectrum collected in analog mode. Sample: NIST 1104 brass standard. Conditions: 2.0 kV, 1.5 mA, 3.0 torr, 120 mL/min, 400 Hz, 20 μs PW, -1500 V detector voltage, 3 s integration time.

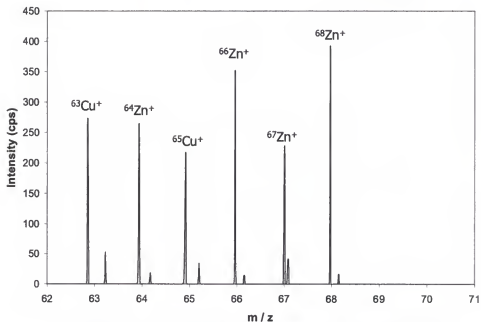


Figure 5-13. Mass spectrum collected in digital mode. Operating conditions as in Figure 5-12.

and the integration time of the MS, which is typically 400 Hz and 3 seconds, respectively. Thus, only 1200 individual mass spectra are collected and averaged every second, which is considerably less than collected with the unmodified ICP system. Therefore, the pulsed system is unable to collect a sufficient number of spectra to display the full peak shape using digital counting mode.

Although increasing the pulse frequency or the integration time may alleviate the spectral frequency deficiency of the pulsed system, neither option is practical. Increasing the pulse frequency beyond 1000 Hz yields an unstable plasma and the integration time required for sufficient spectral averaging would be too long for practical analyses.

Sensitivity

The mass spectrum of a NIST 494 copper standard is shown in Figure 5-14. Peaks are found for antimony, silver, and tin, which are present at 4.5, 50, and 70 ppm, respectively. The detection limit (DL - ppb) of the system can be calculated by:¹²⁶

$$DL = (k * N) / m \quad (\text{Eqn. 5-5})$$

where k is a confidence factor (often chosen as 3), N is the peak to peak noise, and m is the calibration slope. The slope is equivalent to the quotient of the ion signal and the total concentration of the trace element times the concentration of the particular isotope of interest. The $^{123}\text{Sb}^+$ isotope, which is approximately 43% of naturally occurring antimony, was used to calculate the detection limit of our GD-TOFMS. Using an ion signal of 0.12 mV and a peak-to-peak noise of 0.03 mV, as

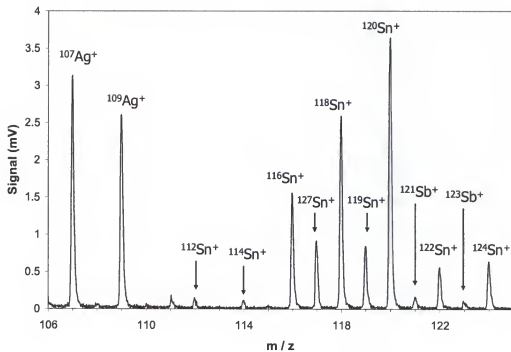


Figure 5-14. Mass spectrum of NIST 494 copper standard. Conditions: 2.0 kV, 1.3 mA, 3.6 torr, 200 mL/min, 400 Hz, 20 μ s PW, -2500 V detector voltage, 3 s integration time. Concentrations: Sn - 70 ppm, Ag - 50 ppm, Sb - 4.5 ppm.

shown in Figure 5-14, the limit of detection is calculated to be approximately 50 ppb. This DL has been calculated using the mass spectrum shown in Figure 5-14, which was collected in analog mode. The calculated DL (i.e., 50 ppb) is likely conservative since enhanced signals are found by integrating in the digital counting mode, which was not available.

Resolving Power

The resolving power (R) of a mass spectrometer, which is its ability to separate ions having small m/z differences, is defined as:

$$R = m / \Delta m \quad (\text{Eqn. 5-6})$$

where, m (AMU) is the mass of a particular ion, and Δm (AMU) is the discernable mass difference.¹²⁷ Equation 5-6 can be modified for the time-domain, t (s), inherent of TOFMS, as:

$$R = t / 2 \Delta t \quad (\text{Eqn. 5-7})$$

in which Δt (s) is the full-width at half-maximum (FWHM) of the peak. The mass resolving power of our pulsed GD-TOFMS system is shown for the copper, tin, and lead regions in Figure 5-15, Figure 5-16, and Figure 5-17, respectively. The resolving power increases as a function of m/z , as predicted by Equation 5-7.

Linear Dynamic Range

A marked limitation of TOFMS is its small linear dynamic range (LDR). Detecting a range of ion concentrations proves difficult because all ions are sampled simultaneously; therefore, the detector becomes saturated by elements at high

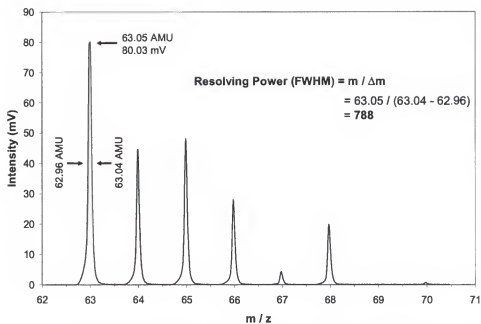


Figure 5-15. Resolving power of the TOFMS for the $^{63}\text{Cu}^+$ isotope. Sample: NIST 1104 brass standard (61.33% Cu). Conditions: 2.0 kV, 1.9 mA, 3.2 torr, 180 mL/min, 400 Hz, 20 μs PW, -1600 V detector voltage, 3 s integration time.

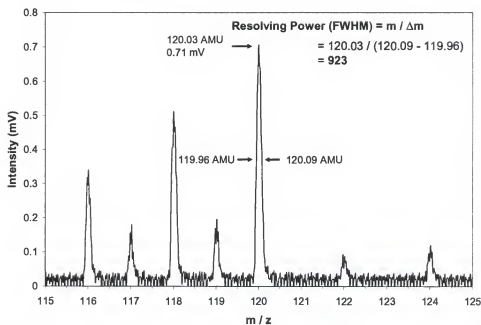


Figure 5-16. Resolving power of the TOFMS for the $^{120}\text{Sn}^+$ isotope. Sample: NIST 1104 brass standard (0.43% Sn). Same conditions as Figure 5-15.

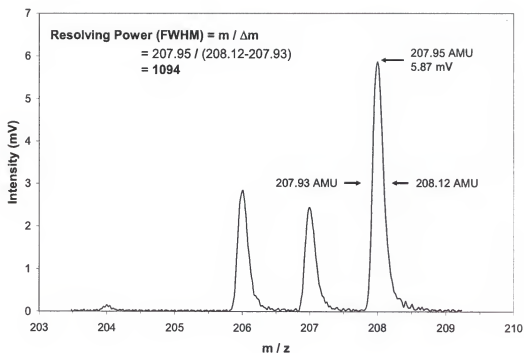


Figure 5-17. Resolving power of the TOFMS for the $^{208}\text{Pb}^+$ isotope. Sample: NIST 1104 brass standard (2.77% Sn). Same conditions as Figure 5-15 and Figure 5-16.

concentration (e.g., matrix) when measuring trace species at a high detector voltage. The linear dynamic range of our TOFMS can be calculated by dividing the maximum signal intensity prior to saturation by the minimum detectable signal. Figure 5-18 shows two MS segments collected for a NIST 1104 brass standard. The $^{63}\text{Cu}^+$ signal in the upper figure shows the maximum signal that can be collected before the detector is saturated, while the lower mass spectrum shows a $^{122}\text{Sn}^+$ signal that is resolved from the baseline. Using the definition of LDR, our TOFMS is estimated to have a dynamic range of approximately 3 orders of magnitude.

Isotopic Accuracy

The isotopic precision was also calculated for our TOFMS system. In TOFMS, all ions are sampled simultaneously, which removes drift and multiplicative noises from individual ion signals.³⁷ This simultaneous sampling makes the TOF well-suited for isotopic analysis. Referring to Figure 5-14, the measured tin 120/116, 118/116, and 120/118 ratios are 2.3₄, 1.6₆, and 1.4₀, respectively. These values are comparable to the nominal ratios of 2.242₉, 1.667₅, and 1.328₅, respectively.¹²⁸

Signal-to-Noise Considerations

The noise originating from our GD-TOFMS was also characterized, as shown in Figure 5-19. The detector and triggering system can significantly contribute to the overall noise of a pulsed spectrometer. However, based on the two profiles in Figure 19, which are quite similar, both of these sources of noise were eliminated as

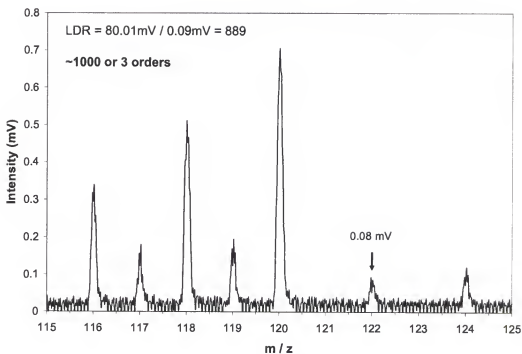
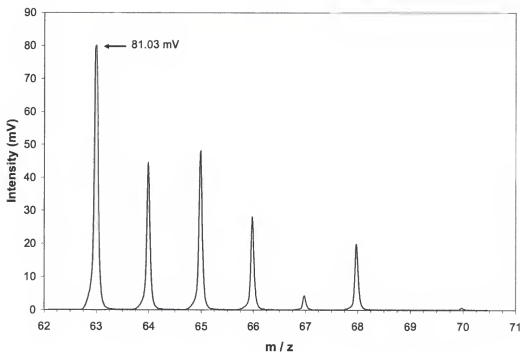


Figure 5-18. Linear dynamic range of the TOFMS. Sample: NIST 1104 brass standard. Conditions: 2.0 kV, 1.9 mA, 3.2 torr, 180 mL/min, 400 Hz, 20 μ s PW, -1600 V detector voltage, 3 s integration time.

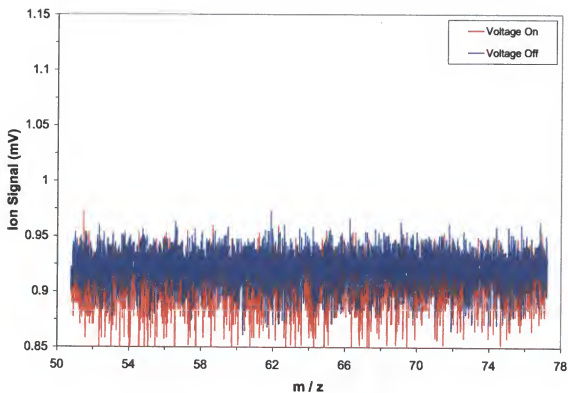


Figure 5-19. Mass spectra showing the inherent noise of the GD-TOFMS. Spectra collected with operating voltages and triggering off (blue) and on (red).

major contributors. The blue profile was collected with the detector voltage and triggering system turned off, whereas the red profile was collected with the detector voltage and triggering turned on. Therefore, the random fluctuations in Figure 19 indicate that the noise in our system is a type of random noise, such as fundamental noise, which cannot be eliminated. After deconvoluting the profiles in Figure 19, they could not be correlated in time with a particular frequency. This result also suggests fundamental noise, such as white (i.e., Gaussian) noise, which is independent of frequency.¹²⁹

CHAPTER 6
ION TRANSPORT DIAGNOSTICS IN A MICROSECOND PULSED GRIMM-TYPE
GLOW DISCHARGE TIME-OF-FLIGHT MASS SPECTROMETER

Introduction

The glow discharge (GD) is a versatile source for the direct analysis of solid materials, and glow discharge mass spectrometry (GDMS) has become an established technique for applications that require elemental analysis.^{28,118} GD sources typically employ a diode configuration in which the sample is placed on the end of a direct insertion probe (DIP). In such case, the sample is limited to a configuration that can be mounted on the DIP and contained within the source chamber. Problems attributed to the DIP configuration include sample placement, thermal effects, and redeposition on source components.⁷¹

The Grimm-type GD source has found wide-spread use in glow discharge atomic emission spectrometry (GD-AES) owing to certain inherent advantages of a Grimm-type source over a DIP source. In the Grimm source, the sample is mounted externally, allowing easy sample interchange and good precision in sample placement. The Grimm source also allows depth profiling due to its well-defined planar sputtering on the sample surface.⁶⁰

Despite its success as an atomic emission source, the Grimm source has found limited application for mass spectrometric analysis because of two primary limitations. First, unlike photons, which undergo self-transport, ions require assisted

transport from the plasma to the MS sampling orifice. Second, the MS vacuum system provides an interface problem not encountered with optical spectrometers. While the vacuum problem can be alleviated with the addition of a slide valve,³⁷ ion transport is more complex. Transfer efficiency is crucial to the success of the analysis, since it has a direct influence on detection limits and temporal separation of ions. Understanding the source parameters (i.e., operating conditions and source configurations) that influence ion transfer can lead to more efficient analyses.

The combination of a GD ion source and a time-of-flight mass spectrometer (TOFMS) was described previously in Chapter 5. In addition to allowing fast acquisition and high transmission, TOFMS affords collection of the entire mass spectrum with every pulse extraction. Since the TOFMS detects ions in a rapid pulse sequence, a pulsed ionization source or gated introduction of ions from a continuous source is required.

The GD in our research is operated in a microsecond pulsed power mode, as described in Chapter 3. The application of high, short-term power produces enhanced sputtering, atomization, excitation, and ionization, in addition to reduced sample heating. Inherently, the pulsed mode allows temporal decoupling of the two types of discharge species, (1) gaseous components (e.g., argon, trace water vapor, etc.) and (2) sputtered cathode material. This phenomenon affords time-resolved analyses not possible using a dc mode.³⁸ Using time-resolved separation, preferential detection of sample analyte ions is possible, while discriminating against background discharge gas ions.

The combination of a microsecond pulsed Grimm-type glow discharge source with a TOFMS is described. Emphasis is placed on the diagnosis of Grimm-type GD-TOFMS transport limitations. Overcoming this limitation opens new GD applications (e.g., depth profiling) that are more difficult using a DIP-type GD. Operating conditions and sampling configurations that play a significant role in ion transport efficiency are described.

Experimental

Glow Discharge Source and Time-of-Flight Mass Spectrometer

The glow discharge source employed in this research, an in-house designed Grimm-type configuration operated in the microsecond pulsed mode, was described previously in Chapter 5. The mass spectrometer, a commercial TOF instrument (Renaissance, LECO Corporation, St. Joseph, Michigan, USA), was also described in Chapter 5. Refer to Figure 5-6 and Figure 5-9 for a schematic of the GD source and TOFMS, respectively.

Sample Material

All samples are certified standard reference materials. Operating condition and temporal resolution studies of various source configurations used a NIST 1104 free-cutting brass standard (National Institute of Standards and Technology, Gaithersburg, Maryland, USA). Mass spectra collected with the varying source configurations employed a NIST 1122 beryllium-copper standard (National Institute of Standards and Technology, Gaithersburg, Maryland, USA). The temporal

resolution application used a CKD 239 cast-iron standard (Research Institute CKD, Prague, Czech Republic).

Results and Discussion

Background

The glow discharge produces atoms and ions by means of sputtering and collisional processes, as described in Chapter 2. Several models have been proposed to account for the observed experimental results.¹³⁰⁻¹³² The mass transfer of analyte atoms after release from the cathode sample is affected by a number of factors, including diffusion, migration, and convection.³⁹ Positive analyte ions (secondary ions) are returned to the cathode surface by the high field of the cathode dark space, so they do not enter into extended mass transfer consideration.

Diffusion results from concentration differences in the GD plasma, whereby large numbers of analyte atoms are released from the cathode during sputtering and move toward regions of lower concentration, with the rate of diffusion dependent on the differences in analyte concentration [$dc/dt = k(c_b - c_s)$], where c_b and c_s represent concentrations in the bulk plasma and cathode surface, respectively. In a dc system, a steady-state concentration gradient is established, extending from the cathode to the walls of the GD housing. In our pulsed system, a packet of atoms is injected periodically into the plasma with subsequent diffusion and dilution across the GD volume. A constantly changing concentration gradient is produced as the sputtered atoms move through the plasma, away from the cathode, until all are deposited on cell surfaces or removed through the pumping process, normally within

a few milliseconds and well before the next discharge pulse. Hang has calculated diffusion times of sputtered atoms based on a collaboration of theoretical models and mass spectral data for a microsecond pulsed GD.¹³³

Migration involves movement of charged particles by a potential gradient. Presumably this could affect the transport of analyte ions formed beyond the cathode dark space, but it is not likely a significant overall factor because the negative glow, which forms the greater part of a GD, is essentially field free.⁴⁷ It should be noted that migration is a term occasionally used in a general transport/diffusion manner.

Convection refers to a mechanical means of assisted mass movement, such as stirring. In the GD, "stirring" results from the fact that GD sources do not operate as sealed, static systems, but instead depend on a constant flow of renewing discharge gas, usually argon, to remove desorbed impurity gases, such as water vapor, hydrocarbons, etc. The rate of this gas flow and its position of entry (with respect to the cathode sputter volume) can influence redeposition of sputtered atoms onto the cathode and net mass transport across the GD plasma. In a sealed hollow cathode tube, as used in atomic absorption analysis, pure diffusion processes can be considered to control mass transfer. However in conventional flow-through GD sources, both diffusion and convection processes are important.

Parametric Study

Gas flow rate. Transport of sputtered material has generally been attributed to diffusion, although Hang and colleagues recognized that gas flow could contribute

to atom transport.¹³³ Bogaerts et al. recently reported a broad computational model to describe how the flowing discharge gas influences GD plasma characteristics.³⁹ We report here the effect of gas flow rate on ion signal intensities and temporal profiles. The influence of gas (Ar) flow on ion transport was studied independently of source pressure. When the gas flow is adjusted, source pressure can be compensated by adjustment of the auxiliary pumping line. The gas flow meter affords measurement of this gas flow.

The pulsed discharge permits separation of the two types of discharge species (discharge gas and sputtered analyte) allowing each to be studied independently. The gaseous species in the discharge are represented in Figure 6-1, which shows the response of $^{40}\text{Ar}^+$ signal as a function of delay (sampling) time over a range of flow rates at constant pressure. Argon ions, formed immediately upon discharge initiation, are detected within a 10 μs delay. The signal level at this delay time remains constant for the entire range of flow rates and up to approximately 30 μs after plasma initiation. Immediate detection of argon ions and a subsequent constant signal indicate these initially detected $^{40}\text{Ar}^+$ ions originate from argon atoms that are ionized in or near the sampling orifice expansion jet, where introduced gas flow rate is not a determining factor. At 30 μs delay, the argon ion signal increases sharply with increasing delay time, forming at approximately 50 to 60 μs a maximum that is not greatly influenced initially by flow rate. At higher gas flow rates, 100-120 mL/min, bandwidth of the argon signal becomes narrowed, indicating the more rapid "wash-out" of the ions at the higher flow rates. It is also possible that the ionization efficiency changes with flow rate, which could also contribute to the observed

profiles. Changing the flow rate has a slight effect on the temporal signal response ($^{40}\text{Ar}^+$ signal) as a function of delay time. The ion signals show approximately the same rising slope for all flow rates, corresponding to sampling of argon ionized near the skimmer cone and thus not significantly affected by flow rate. Higher flow rates have a relatively small effect on the time required for Ar ions to reach the MS sampling orifice. For example, the maximum Ar^+ signal at 120 mL/min appears only 10 μs earlier than the corresponding 40 mL/min maximum. The decrease in delay time with increasing flow rate should be more pronounced for sputtered sample atoms that must travel the entire cathode to sampling orifice distance.

Figure 6-2 shows the larger effect gas flow rate has on the transfer of sample ions ($^{63}\text{Cu}^+$) compared to gaseous species (e.g., $^{40}\text{Ar}^+$). Unlike gas ions, which are detected after a short delay (e.g., 10 μs), sample ions are not detected until approximately 40 μs after pulse initiation. This time difference arises from the longer distance required for sputtered species to migrate to the sampling region. Evident is a considerable time spread over which analyte ions are detected, which is influenced by where the ions are formed and what type of collisional path is experienced. Atoms formed within the time scale of a 10 μs discharge pulse, yield measured ions over a broadened profile of 200 μs or more. Copper ions detected at short delay times (e.g., 40 μs) experience less collisional resistance during their migration to the sampling orifice than ions at longer delays. The maximum Cu^+ signal in Figure 6-2 significantly increases as a function of argon gas flow, although the position of the maximum in terms of delay changes little. Moving from low to high flow rates, gas flow transports more analyte ions to the TOF and also shifts the Cu^+ profile from a

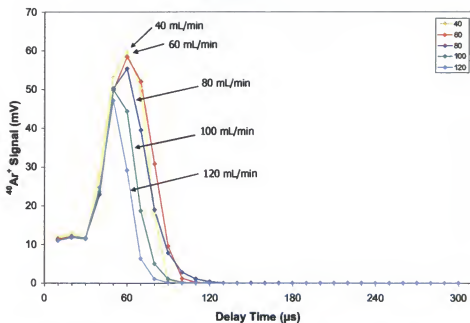


Figure 6-1. Plot of argon signal as a function of delay time for a range of flow rates at constant pressure. Operating conditions: 2.0 kV, 3.0 torr, 400 Hz pulse frequency, 20 μs pulse width, -1500 V detector voltage. Sample: NIST 1104 brass standard.

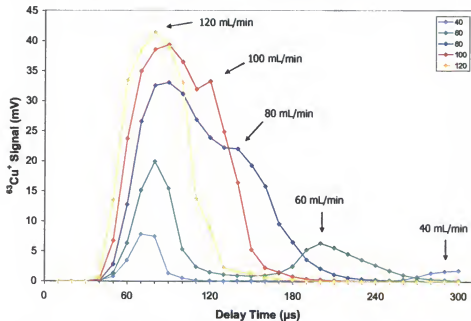


Figure 6-2. Plot of copper signal as a function of delay time for a range of flow rates at constant pressure. Conditions as in Figure 6-1.

double peak toward a single peak configuration. While the first peak maintains approximately the same delay time position with changing flow rate, the second peak exhibits a delay-time shift as a function of flow rate, which may be evidence of two ionization mechanisms, such as electron impact and Penning ionization.

The influence of flow rate on ion signal is considerably different for plasma ions (e.g., Ar^+) versus sample ions (Cu^+). While plasma gas ions are only slightly altered by flow rate changes, sample ions are significantly affected due to their longer migration distance. In any case, from a practical consideration, the discharge gas flow rate is crucial in optimizing detection limits and temporal resolution.

Pressure. The discharge pressure was studied, maintaining constant flow rate, to determine its influence on ion transport in a Grimm-type GD-TOFMS. Since pressure determines the mean free path of ions in the discharge, it would be expected to influence the ion transport efficiency. As in the case of flow rate, pressure should have a more pronounced effect on migration of sputtered species ions than gas discharge ions. Figure 6-3 shows the response of $^{40}\text{Ar}^+$ as a function of delay time for a range of discharge pressures at constant flow rate. As previously noted, argon ions resulting from ionization near the skimmer cone are detected at 10 μs . The argon ionization mechanism is unaffected by changing the discharge pressure, as indicated by similar contours up to 30 μs , similar to those obtained as a function of flow rate (Figure 6-1). Despite the similarity, the profiles in Figure 6-3 show different ion intensities as a function of pressure. Increasing pressure tends to shift the ion maximum to longer delay times, in keeping with greater collisional

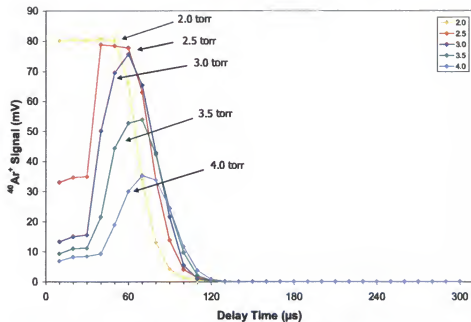


Figure 6-3. Plot of argon signal as a function of delay time for a range of pressures at constant flow rate. Operating conditions: 2.0 kV, 60 mL/min, 400 Hz pulse frequency, 20 μs pulse width, -1500 V detector voltage. Sample: NIST 1104 brass standard.

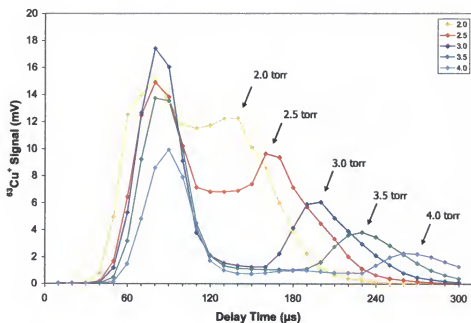


Figure 6-4. Plot of copper signal as a function of delay time for a range of pressures at constant flow rate. Conditions as in Figure 6-3.

effects. In addition, the ion maximum drops more than half at the higher pressures. A smaller mean free path (higher pressure) shifts the peak intensity to longer delay times since more collisions increase the ion residence time in the source. Thus, operating pressure plays a significant role in effective transport of gaseous species.

Figure 6-4 shows the response of $^{63}\text{Cu}^+$ as a function of delay time for various discharge pressures at a constant gas flow rate. The $^{63}\text{Cu}^+$ signal does not appear within the first 30 μs due to the transport time required. Pressure affects the delay time at which the $^{63}\text{Cu}^+$ signal is initially detected, unlike $^{40}\text{Ar}^+$, which is detected within 10 μs for all measured flow rates. Increased pressures result in longer delays due to heavy collisional resistance (smaller mean free path) prior to sampling, which leads to ion signal variance as a function of operating pressure. The $^{63}\text{Cu}^+$ profiles exhibit double peaks, as was observed as a function of flow rate. It is the second of the two peaks that is more significantly influenced by the pressure changes, as shown by a shifting of the (second) peak intensities to shorter delay times with increasing pressure. Extrapolation suggests a pressure of approximately 1.0 torr would yield peak convergence, but we could not confirm this, as the discharge at this flow rate was not stable at pressures below 2.0 torr.

Pressure has a significant effect on ion transport in this Grimm-type GD source. Proper selection of the operating pressure is important, since it can influence signal intensity and the optimum delay time at which ions are detected. Choosing a suitable pressure (e.g., 2.0 torr) allows measurement of analyte signal (e.g., $^{63}\text{Cu}^+$) at delay times corresponding to minimal background signal (e.g., $^{40}\text{Ar}^+$).

Other operating parameters. Additional operating parameters of the glow discharge, such as plasma voltage (Figure 6-5 and Figure 6-6), pulse width (Figure 6-7 and Figure 6-8), and pulse frequency (Figure 6-9 and Figure 6-10), were examined for their influence on ion transport. While it is important to control these conditions for optimizing ion signal, they do not significantly influence ion transfer. For example, higher ion signals are obtained by increasing the plasma voltage, but this is due to increased sputtering and subsequent ionization (i.e., higher average current) rather than more effective transport.

Source Design

In addition to discharge operating conditions (e.g., flow rate and pressure), the source configuration influences transport efficiency. Modifying the source can alter gas flow patterns that affect ion transfer and the amount of discharge gas and sample ion mixing. Three source configurations and their effect on ion transport efficiency are described.

Initial source design. Figure 6-11 shows a cross-section of a Grimm-type source that employs a conventional sampler and skimmer cone for sampling ions into the mass spectrometer. After evaluating a range of sampler orifice diameters, a 4 mm sampler provided the highest signal. In effect, this large orifice minimizes true sampler operation, but the favorable ion signal caused us to maintain the large sampler for all subsequent comparisons with other source configurations. As shown in Figure 6-11, plasma gas is introduced through a small orifice (approximately 1

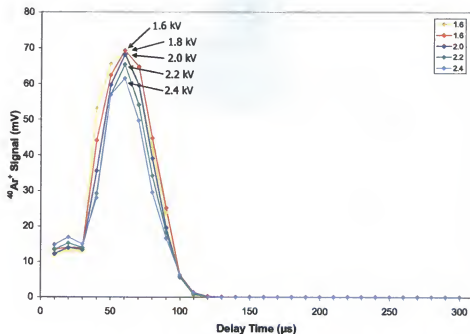


Figure 6-5. Plot of argon signal as a function of delay time for a range of voltages. Operating conditions: 3.0 torr, 60 mL/min, 400 Hz pulse frequency, 20 μ s pulse width, -1500 V detector voltage. Sample: NIST 1104 brass standard.

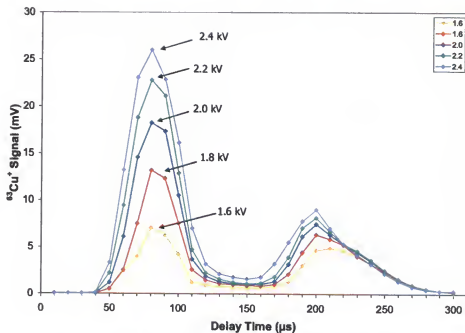


Figure 6-6. Plot of copper signal as a function of delay time for a range of voltages. Conditions as in Figure 6-5.

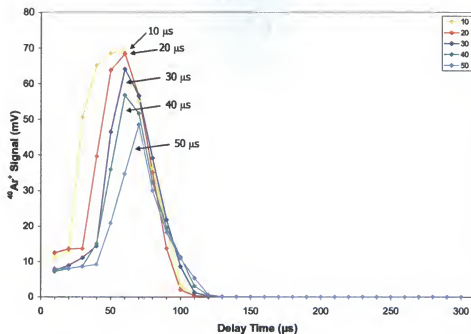


Figure 6-7. Plot of argon signal as a function of delay time for a range of pulse widths. Operating conditions: 2.0 kV, 3.0 torr, 60 mL/min, 400 Hz pulse frequency, -1500 V detector voltage. Sample: NIST 1104 brass standard.

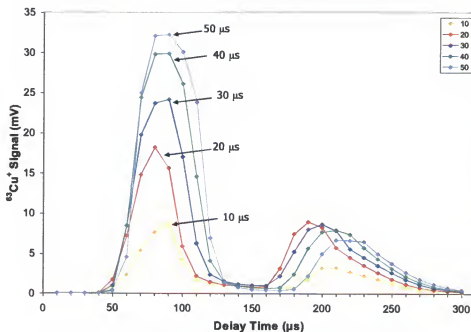


Figure 6-8. Plot of copper signal as a function of delay time for a range of pulse widths. Conditions as in Figure 6-7.

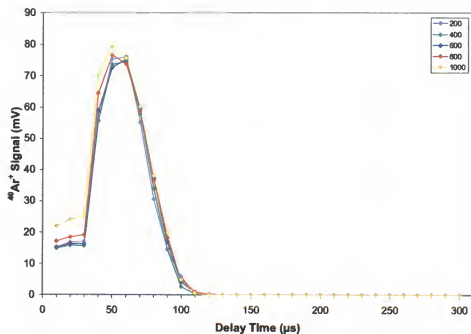


Figure 6-9. Plot of argon signal as a function of delay time for a range of pulse frequencies. Operating conditions: 2.0 kV, 3.0 torr, 60 mL/min, 20 μ s pulse width, -1500 V detector voltage. Sample: NIST 1104 brass standard.

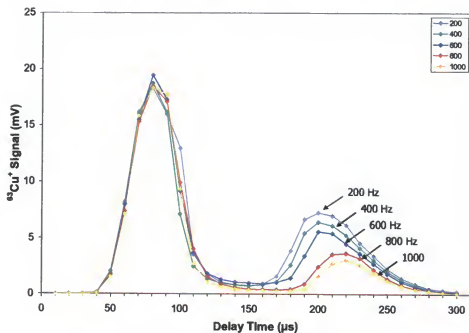


Figure 6-10. Plot of copper signal as a function of delay time for a range of pulse frequencies. Conditions as in Figure 6-9.

mm) in the source mount, before traveling through a narrow gap between the sampler and anode to reach the plasma cavity within the anode cylinder. The gas fills the anode cylinder, permitting formation of the discharge plasma, and is continuously exhausted through the sampler orifice. Thus, little in the way of directional flow near the cathode would be expected.

Figure 6-12 presents plots of $^{40}\text{Ar}^+$ and $^{63}\text{Cu}^+$ signal versus delay time for the source configuration shown in Figure 6-11. Argon ions are detected at 10 μs due to its ionization upon plasma initiation and immediate sampling. The Ar^+ signal exhibits a sharp fall from this initial high intensity to a minimum at approximately 60 μs before reversing and showing a second region of high intensity at 100 μs , after which it falls gradually to background by 210 μs . Two different waves of $^{40}\text{Ar}^+$ ions are produced, the first from the initial discharge breakdown, the second from some other ionization step, as yet unknown. Only a small copper ion signal is detected, beginning after 80 μs and extending to about 200 μs . At this flow rate ($>120\text{ mL/min}$), the $^{63}\text{Cu}^+$ profile does not exhibit a double peak. Compared to corresponding profiles in Figure 6-1 and Figure 6-3, the $^{40}\text{Ar}^+$ signal is maintained significantly longer with the configuration of Figure 6-11. The longer delay is a result of ineffective ion transfer using the gas flow pattern of the configuration in Figure 6-11. Ion transfer using this sampler/skimmer arrangement, a design previously employed in our laboratory with good success,^{14,119} has been generally attributed to diffusion. Mixing of argon and sample ions occurs because the argon ions are not efficiently transported to the sampling orifice at short delay times, resulting in an extended residence time and

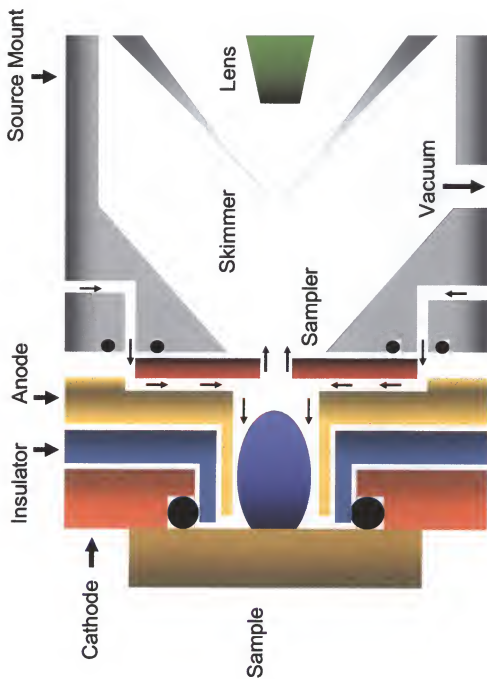


Figure 6-11. Schematic cross-section of the Grimm-type glow discharge ion source employing a flat sampler (4 mm i.d. orifice). Not drawn to scale.

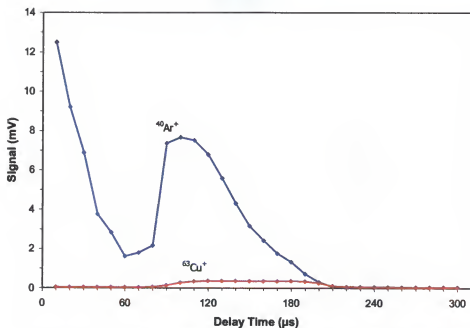


Figure 6-12. Plot of argon and copper ion signal versus delay time collected using conditions optimized for the source shown in Figure 6-11. Operating conditions: 2.0 kV, 2.8 torr, 200 mL/min, 400 Hz, 20 μ s, -1500 V. Sample: NIST 1104 brass standard.

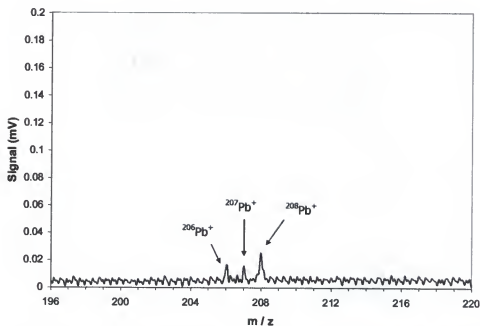


Figure 6-13. Lead isotope mass spectrum collected using the source configuration shown in Figure 6-11 and a copper standard containing 30 ppm Pb. Operating conditions: 2.0 kV, 2.7 torr, 160 mL/min, 400 Hz, 20 μ s, 200 μ s, -2200 V. Sample: NIST 1122 copper standard.

their detection at long delays. This "atomic" mixing of argon and sample ions prevents temporal resolution experiments.

In addition to temporal response, the detection limit of the configuration shown in Figure 6-11 was measured. Figure 6-13 shows a portion of the mass spectrum from a NIST 1122 standard containing 30 ppm lead. The poor lead signal is in keeping with results shown in Figure 6-12, which demonstrated a small matrix ($^{63}\text{Cu}^+$) signal. This weak signal is attributed to the inefficient ion transfer that is obtained with the configuration shown in Figure 6-11. This sampling configuration, consisting of a sampler and skimmer cone, has proven to work well with a DIP-type GDMS,^{14,119} illustrating inherent differences in ion transport using a Grimm-type GDMS. This transfer inefficiency must be overcome for the Grimm configuration to be an analytically useful MS source.

Gas directing sleeve design. The source configuration in the preceding discussion (Figure 6-11) was inefficient at transporting sample ions due to the ineffective flow pattern. Figure 6-14 shows a cross-section of the source in which the flat sampler has been replaced by a gas-directing sleeve device. This gas-directing sleeve device draws upon principles previously shown in a commercial GD source (Atom Source, Leeman Labs, Fishkill, New York, USA), which uses a jet-assisted GD for reducing matrix effects in atomic absorption measurements. In our model of the gas-directing sleeve configuration, the internal diameter of the sleeve is 4 mm, the same internal diameter of the flat sampler used in the previous configuration. The sleeve extends to approximately 0.2 mm from the end of the

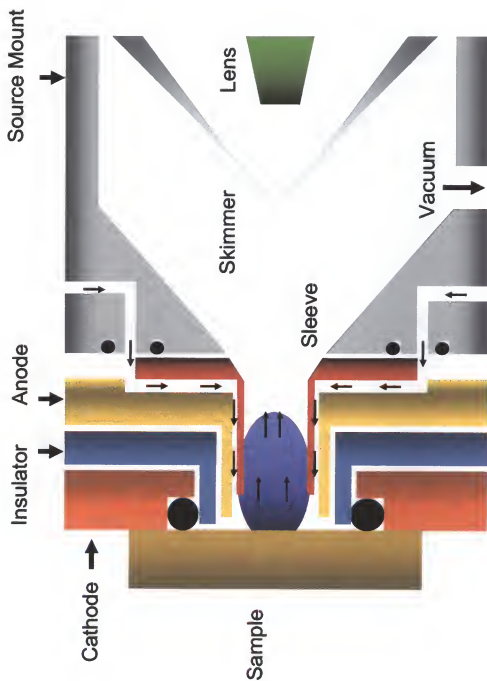


Figure 6-14. Schematic cross-section of the Grimm-type glow discharge ion source with a gas-directing sleeve in place of a flat sampling device. Not drawn to scale.

anode and is smaller in diameter than the anode, leaving a gap for gas to flow. As in the previous design, gas is introduced through the sample mount orifice and flows between the anode and sampler (i.e., sleeve). The sleeve forces the gas to travel through the gap and across the sample surface before flowing toward the skimmer cone. Directing the gas flow with this device was aimed to improve ion transfer.

The improvement obtained with this source is illustrated in Figure 6-15, which shows profiles of $^{40}\text{Ar}^+$ and $^{63}\text{Cu}^+$ versus delay time, indicating the temporal resolution attainable using the gas directing sleeve. Here we see only one peak for each species, with the $^{40}\text{Ar}^+$ signal now reduced in intensity and becoming well separated from the analyte signal. More analytical significance is seen from the enhanced $^{63}\text{Cu}^+$ signal that results from this directed gas flow, indicating a more efficient transport of analyte from the cathode surface to the ion sampling orifice. The enhanced transport suggests a conversion from diffusion- to convection-dominated processes.

The maximum $^{63}\text{Cu}^+$ signal of Figure 6-15 shows enhanced signal-to-background signals by use of the gas-directing sleeve. Figure 6-16 is a mass spectrum of NIST 1122 collected using the configuration shown in Figure 6-14. The better analytical signal is due to high, directed gas flow across the sample surface, which increases ion transport to the skimmer cone. It also seemed possible that this mode allowed less sample redeposition by sweeping the gas across the sample surface. Weight loss measurements were used to test this redeposition hypothesis. If the gas-directing sleeve decreases sample redeposition, weight losses per unit time should be higher for equivalent discharge conditions. However, multiple trials

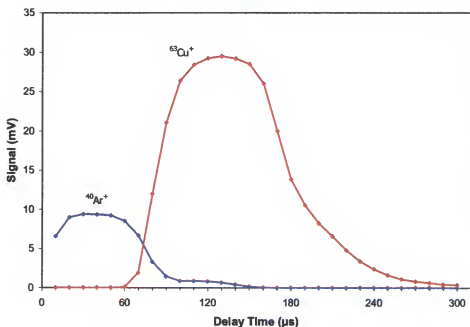


Figure 6-15. Plot of argon and copper ion signal versus delay time collected using conditions optimized for the source configuration shown in Figure 6-11. Operating conditions: 2.0 kV, 2.6 torr, 150 mL/min, 400 Hz, 20 μs , -1500 V. Sample: NIST 1104 brass standard.

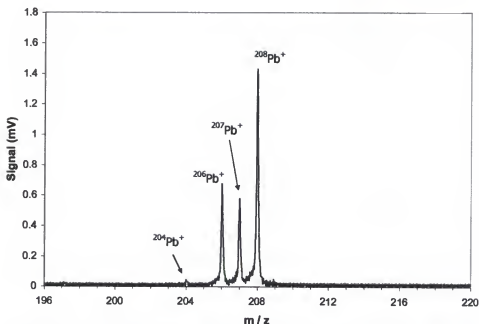


Figure 6-16. Lead isotope mass spectrum of lead isotopes collected using the source configuration shown in Figure 6-14 with a copper standard containing 30 ppm Pb. Operating conditions: 2.0 kV, 2.5 torr, 155 mL/min, 400 Hz, 20 μs , 150 μs , -2200 V. Sample: NIST 1122 copper standard.

using a 70:30 Cu:Zn brass foil (Alfa AESAR, Ward Hill, Massachusetts, USA) showed little difference, with average weight losses of 0.743 ± 0.001 mg and 0.738 ± 0.009 mg for the normal sampler and sleeve configuration, respectively. Thus, the increased signal found with a gas-directing sleeve appears to arise from more efficient ion transport, not from less redeposition.

Sampler/Sleeve combination design. Despite the improvements obtained, the effect on overall sampling distance was a concern in replacing the sampler with the gas-directing sleeve. Using a sampler and skimmer configuration (Figure 6-11), sample ions must travel approximately 6 mm prior to the initial sampling point provided by the flat sampler. The ions then travel another 7 mm before they are extracted by the skimmer cone. Changing to the gas-directing sleeve configuration (Figure 6-14) removes the GD sampler, meaning that the sample material must travel the total 13 mm without an intermediate sample extraction point. Although ion signal enhancement was achieved using the gas-directing sleeve, it seemed to us likely that the transport efficiency could be increased by adding an intermediate sampling point.

Figure 6-17 shows a Grimm configuration employing a hybrid of the two previous source designs. This configuration uses a gas-directing sleeve (4 mm i.d.) and flat sampler (3 mm i.d.). Although other sizes were evaluated, a 3 mm sampler yielded the highest transport efficiency with the sleeve-type source.

Figure 6-18 presents a plot of $^{40}\text{Ar}^+$ and $^{63}\text{Cu}^+$ signal versus delay time collected using the configuration shown in Figure 6-17. This profile has two key

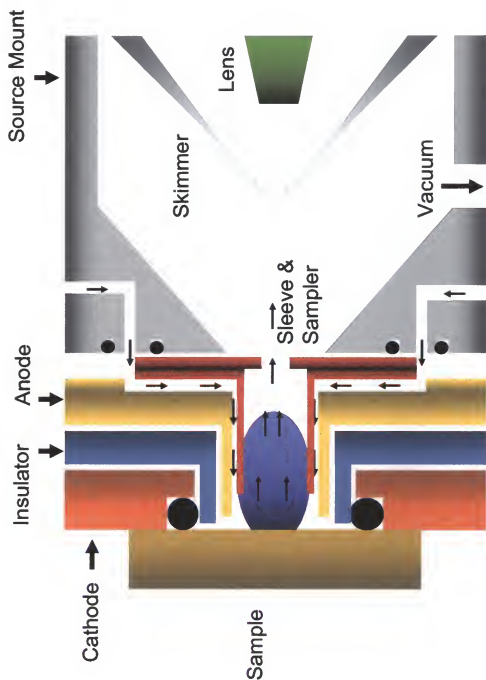


Figure 6-17. Schematic cross-section of the Grimm-type glow discharge ion source employing a gas-directing sleeve and flat sampler hybrid configuration. Not drawn to scale.

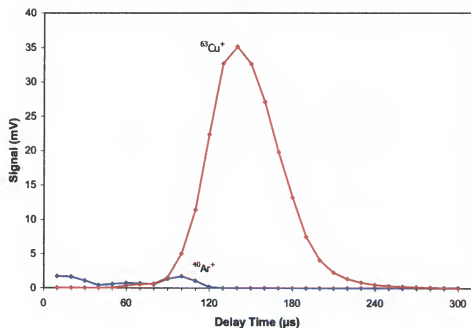


Figure 6-18. Plot of argon and copper ion signal versus delay time collected using conditions optimized for the source shown in Figure 6-17. Operating conditions: 2.0 kV, 2.8 torr, 190 mL/min, 400 Hz, 20 μs , -1500 V. Sample: NIST 1104 brass standard.

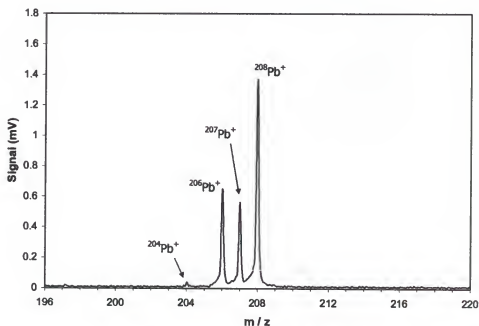


Figure 6-19. Lead isotope mass spectrum of lead isotopes collected using the source configuration shown in Figure 6-17 with a copper standard containing 30 ppm Pb. Operating conditions: 2.0 kV, 2.8 torr, 135 mL/min, 400 Hz, 20 μs , 175 μs , -2200 V. Sample: NIST 1122 copper standard.

differences from the profiles obtained using only the gas directing sleeve (Figure 6-15). A much more favorable analyte-to-argon ratio is seen, and temporal separation at 140 μs yields a spectrum highly dominated by the analyte ions. Figure 6-18 indicates that a delay time compromise is not necessary, since the delay yielding the maximum $^{63}\text{Cu}^+$ signal corresponds to an $^{40}\text{Ar}^+$ signal that has already fallen to baseline.

While the ability to perform temporal resolution with a microsecond pulsed GD-TOFMS has been shown,³⁸ the level of discrimination against the background interfering ions in this profile is noteworthy. The low $^{40}\text{Ar}^+$ signal intensity can prove significant when the detector voltage is increased for trace analysis, whereby small amounts of background gas can interfere with sample detection. Addition of the sampler leads to only a small enhancement ($\sim 15\%$) in sensitivity, as shown in Figure 6-19.

Application of Temporal Resolution

The configuration shown in Figure 6-17, which employs a gas-directing sleeve and flat sampler afforded temporal resolution as demonstrated in Figure 6-18 by effectively resolving matrix signal (e.g., $^{63}\text{Cu}^+$) from the plasma gas (e.g., $^{40}\text{Ar}^+$). While these profiles demonstrate temporal resolution, they do not provide a legitimate situation since these two species are not isobaric interferences. Furthermore, the measurements were collected at a low detector voltage (~ 1500 V) to prevent detector saturation. Increasing the detector voltage often reveals trace amounts of the background gas at extended delay times due to the increased

sensitivity. Figure 6-20 shows mass spectra taken at various delay times for a CKD 239 cast-iron standard reference material containing 380 ppm Mg. To achieve optimal temporal resolving power, these spectra were collected using the gas-directing sleeve and sampler configuration (Figure 6-18). Before increasing the detector voltage for trace analysis, the $^{40}\text{Ar}^+$ and copper species were deflected (i.e., removed prior to detection) due to their high concentration in the plasma. At short delay times a large signal (off-scale) is found at m/z 20, which corresponds to $^{40}\text{Ar}^{+2}$. Background gas ions of $^{12}\text{C}_2^+$, $^{12}\text{C}_2\text{H}^+$, and $^{12}\text{C}^{14}\text{N}^+$ appear at m/z values of 24, 25, and 26, respectively, likely a result of oil contamination. Figure 6-21 shows the mass spectrum collected at a delay of 10 μs . This figure represents a spectrum collected from a continuous, dc power mode. In this mode, background gas ions and sample ions cannot be separated temporally. Note the baseline shift and detector ringing due to the large concentration of $^{40}\text{Ar}^{+2}$. Referring back to Figure 6-20, the signal from these background ions decreases as the delay time is increased. Figure 6-22 shows a mass spectrum at 60 μs , in which the carbon-containing background species have been temporally resolved, and only a small amount of $^{40}\text{Ar}^{+2}$ remains. Increasing the delay has also alleviated the baseline shift and detector ringing inherent with short (<40 μs) delay times. As the delay time is increased further, Mg^+ peaks appear at m/z values of 24, 25, and 26. The mass spectrum collected at 170 μs is shown in Figure 6-23. A nominal isotopic pattern was obtained for Mg, indicating that minimal interferences (e.g., carbon-containing species) are contributing to the Mg peaks. A small peak at m/z 23 also appears at long delay times, likely due to a trace amount of ionized Na. As the delay time is

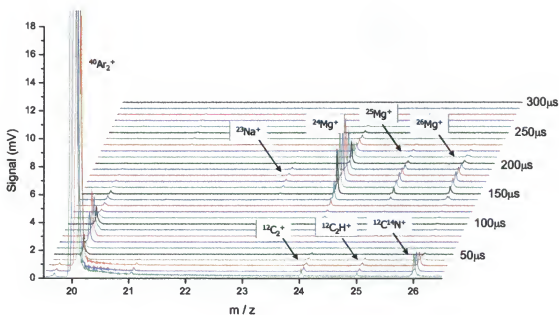


Figure 6-20. Mass spectra showing the temporal detection of trace Mg (380 ppm) using the source configuration shown in Figure 6-17. Operating conditions: 2.0 kV, 2.8 torr, 135 mL/min, 400 Hz, 20 μ s, -2200 V. Sample: CKD 239 cast-iron standard.

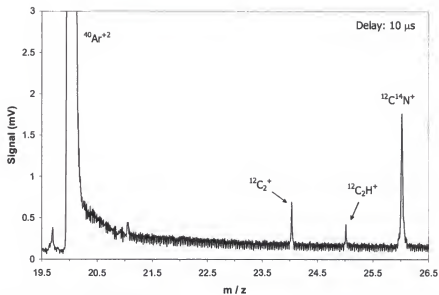


Figure 6-21. Single mass spectrum from waterfall plot shown in Figure 6-20 at a delay time of 10 μ s. Spectrum shows appearance of interfering background ions.

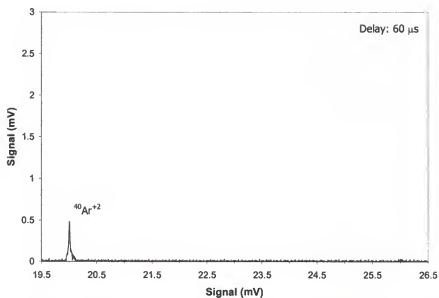


Figure 6-22. Single mass spectrum from waterfall plot shown in Figure 6-20 at a delay time of 60 μ s. Spectrum shows the background ions at m/z 24, 25, and 26 have diminished.

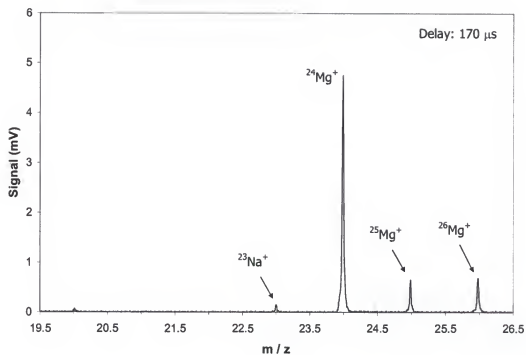


Figure 6-23. Single mass spectrum from waterfall plot shown in Figure 6-20 at a delay time of 170 μ s. Spectrum shows the proper isotopic distribution of Mg.

increased, the Mg ion signal eventually falls to background. This experiment illustrates the ability of a microsecond pulsed Grimm-type GD-TOFMS to detect trace amounts of sample material by temporally discriminating against background isobaric interferences through proper source configuration and operating condition selection.

Concluding Remarks

A microsecond pulsed Grimm-type glow discharge source has been coupled to a commercial time-of-flight mass spectrometer. The Grimm source allowed fast sample interchange and precise control over sample placement. Transport efficiency has been evaluated with various operating conditions and source configurations. Flow rate and pressure are found to significantly influence ion transport. Proper choice of source parameters allows trace analysis with the ability to temporally detect sample ions that prove difficult using a direct current glow discharge source. An example is shown for the trace analysis of magnesium.

CHAPTER 7

DIRECT PIN SAMPLE ANALYSIS USING A CONVENTIONAL GRIMM-TYPE GLOW DISCHARGE SOURCE AND TIME-OF-FLIGHT MASS SPECTROMETER

Introduction

The glow discharge (GD) has become an established mass spectrometric (MS) source for the analysis of solid samples.^{36,37,134,135} Typical glow discharge sources, particularly commercial versions, employ a direct insertion probe (DIP) configuration to introduce samples into the mass spectrometer.⁷⁹ This configuration, as described in Chapter 3, can readily analyze pin- and disc-samples placed on the end of the probe; however, the DIP configuration suffers from problems with sample placement, thermal effects, and redeposition on source components.⁷¹ GD applications that require analyzing layers through planar sputtering, such as depth profiling,^{60,87,88} are difficult using a probe configuration.

An alternative to the DIP is a Grimm-type GD configuration, which has found widespread use in glow discharge atomic emission spectrometry (AES).⁸²⁻⁸⁵ The Grimm configuration (Chapter 3) does not suffer from sample placement problems because the sample is mounted externally on the source, rather than on the end of a probe.^{80,86} The plasma in a Grimm source is confined to a symmetrical well-defined area by the anode, providing planar sputtering of the sample. Thus, depth profiling of sample layers is readily achieved. The sample is pressed against an O-ring on the cathode plate, which ensures adequate sealing and proper vacuum conditions.

While the Grimm source works well for flat, relatively large samples, other sample shapes are less adaptable. For example, pin and wire samples that have a smaller diameter than the sealing O-ring cannot be readily analyzed with a Grimm-type source. Analysis of these sample types can be achieved by replacing the Grimm source by a DIP. Exchanging these source configurations is tedious, time-consuming, and impractical for analyses with alternating sample types (e.g., pin and flat samples). Additionally, both sources require different operating conditions. For example, typical operating pressures are 2 - 6 torr and 0.5 - 1.5 torr for the Grimm- and DIP-configuration, respectively.

An alternative method for analyzing pin samples on a Grimm-type source has been suggested, as represented in Figure 7-1.¹³⁶ Typical pin and wire samples have a smaller diameter than the sealing O-ring. Many pins or wires can be bundled to increase the overall sample diameter. This sample bundle is then pressed into the cavity of a metal sample holder and abraded to form a flat surface, as shown in the upper schematic of Figure 7-1. This bundled, flat surface mimics a smooth surfaced that is adaptable to a Grimm source, as shown in the lower schematic of Figure 7-1. However, this method is viable only if sufficient sample material (e.g., pins) is available for bundling, which proves impractical for analyses in which samples are a premium. Other concerns include: minimizing residual air trapped between the bundled wires, eliminating atmospheric leaks during analysis, and restricting sputtering to the sample surface. If the sample surface is larger than the sealing O-ring, atmospheric leaks can lead to plasma instability and enhanced levels of gaseous interferences (e.g., oxides). Conversely, if the sample surface has a similar

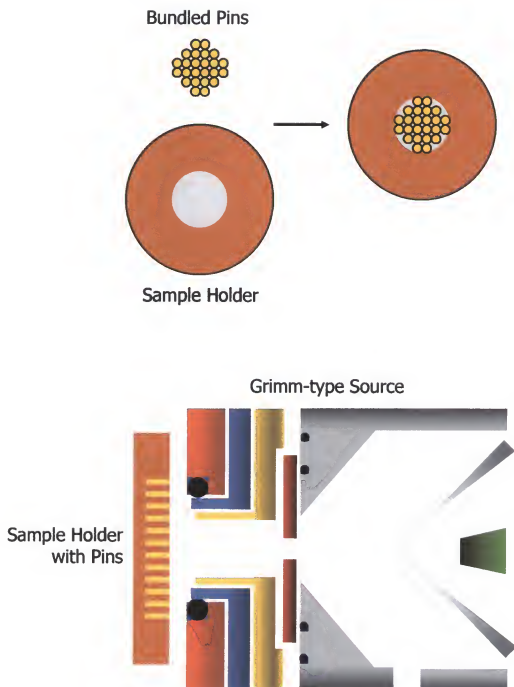


Figure 7-1. Representation of the commercial method for analyzing pin samples with a Grimm-type source.¹³⁶

diameter to the anode, sputtering of the sample holder can introduce superfluous elemental signals.

The Grimm source in the current research is coupled to a time-of-flight mass spectrometer (TOFMS), which is becoming an increasingly useful tool for the GD.^{13,14,37,137,138} As described in Chapter 5, a TOF collects mass spectra in a pulse sequence, which requires a transient introduction of ions into the mass spectrometer. Our microsecond pulsed GD inherently produces ion packets that are introduced into the TOF with each pulse. Chapter 3 described the advantages of pulsed mode operation, including enhanced sputtering, atomization, excitation, and ionization, in addition to reduced sample heating.^{38,104,139,140} One particular advantage of a pulsed GD-TOF is the ability to perform time-resolved analyses that are not possible using the dc mode of operation.^{37,38,141}

We have developed a sample holder for the direct analysis of pin samples on a Grimm GD configuration. Easy sample interchange and good precision - inherent advantages of the Grimm source - are conserved with this sample holder. Additionally, extensive sample preparation steps are not necessary when this sample holder is employed. Fundamental design considerations of the sample holder are shown. Operating conditions of the pin sample holder are similar to Grimm-type flat-sample analysis rather than traditional pin analysis with a probe configuration. Advantages of the pulsed GD-TOFMS, such as temporal resolution and precise isotopic measurements, are shown. The sample holder is a practical alternative to exchanging source configurations to analyze pin- and flat-samples,

and it offers advantages over existing methods of pin analysis with a Grimm-type source.

Experimental

Glow Discharge Source and Time-of-Flight Mass Spectrometer

The glow discharge source employed in this research, an in-house designed Grimm-type configuration operated in the microsecond pulsed mode, was described previously in Chapter 5. The mass spectrometer, a commercial TOF instrument (Renaissance, LECO Corporation, St. Joseph, Michigan, USA), was also described in Chapter 5. Refer to Figure 5-6 and Figure 5-9 for a schematic of the GD source and TOFMS, respectively.

Pin Sample Holder

A picture of the sample holder and components is shown in Figure 7-2. A schematic of the pin sample holder and Grimm-type source is also shown in Figure 7-3. Around the outside of the sample holder, a small rim was machined that corresponded to a raised edge on the cathode surface, allowing reproducible sample placement. The conductive brass base of the sample holder allowed electrical contact with the cathode plate. Macor, an insulating material, was inserted into the middle of the sample holder to ensure that only the pin sample was sputtered during analysis. Installation of an O-ring under the macor minimized leaks into the source. A spring, removed from a spent electronic circuit board, was inserted into the macor, serving two purposes: to secure the pin samples and ensure sufficient electrical

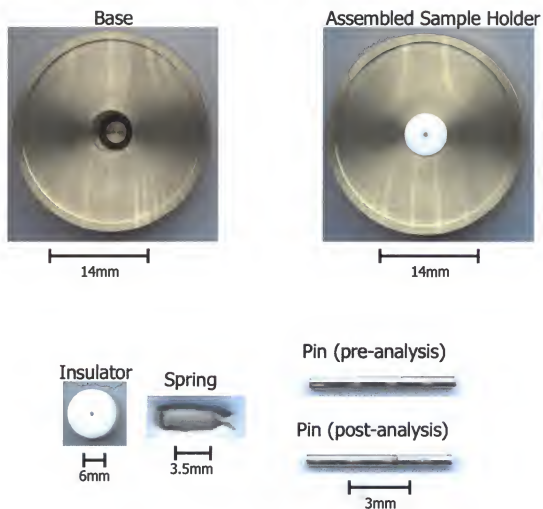


Figure 7-2. Photos of the sample holder and components.

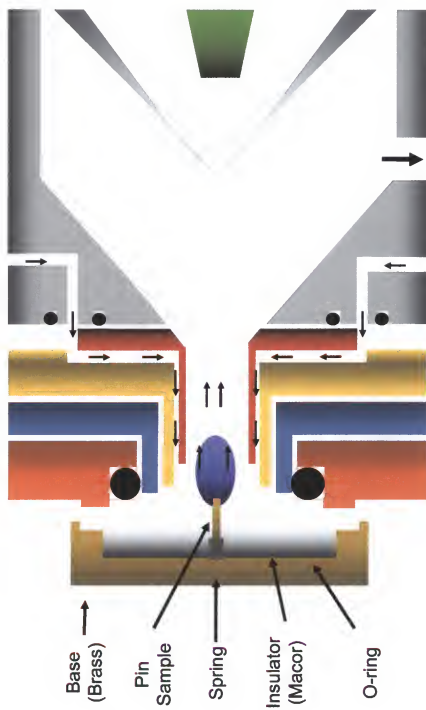


Figure 7-3. Schematic of the pin sample holder and Grimm-type source.

contact between the sample holder and pin. The pin sample, machined to the same diameter as the macor shield, is inserted into the top of the macor and secured with the spring.

Despite the small size of the pin samples used in these experiments (~1 mm diameter), cooling techniques were not required, since the pins cooled during the off-time of the pulsed plasma by heat dissipation through the sample holder.

Sample Material

Pin samples used for measuring sputtering rates were machined from brass rods (Alloy 360, McMaster-Carr, Atlanta, Georgia, USA). Certified brass foils (Puratronic, Alfa Aesar, Ward Hill, Massachusetts, USA) were used for determining the sputtering rate of the Grimm configuration. An analytical microbalance (Model: M2P, Sartorius Corp., Edgewood, New York, USA) was used for weight measurements. The pin and Grimm samples used for matrix and background signal comparisons were machined from an oxygen-free copper rod (Alloy 101, McMaster-Carr, Atlanta, Georgia, USA), as were the samples used for the molecular interference and pin length studies. A NIST 494 copper rod (National Institute of Standards and Technology, Gaithersburg, Maryland, USA) was used for detection limit calculations.

Results and Discussion

Sample Holder Design

A representation of the sample holder used in these experiments is shown in Figure 7-3. A macor sleeve and spring is used to secure the pin or wire sample; however, the previous sample holder iteration (not shown) used a copper plate to secure the pin sample. Two related problems were encountered using a conductive material to secure the pin: plasma instability and sample holder sputtering. The plasma was often unstable due to the apparent formation of two plasmas, one on the pin sample and the other on the plate surface. After sputtering, a crater equivalent to the diameter of the anode orifice was apparent on the sample plate. Also, the exposed portion of the pin exhibited a color distinctly different from a non-sputtered portion. The plate required sanding after each analysis to re-establish a flat surface.

Cylindrical pins can be directly inserted into the sample holder, shown in Figure 7-3. The previous sample holder iteration suffered from an unusual pin shape required. This design required the pins to be machined into a stair-step design, in which the base of the pin was held by the aforementioned copper plate. This pin configuration was limited by the precise machining step necessary.

Source/Plasma Configuration

A fundamental question concerning the use of our pin sample holder is the type of discharge formed; a Grimm-type discharge that is defined by the anode, or a diode-type discharge, which is often obtained with a DIP configuration. One might expect a Grimm-type discharge since the sample holder is mounted to a Grimm

source; however, a macor shield is installed at the base of the pin. Therefore, the resulting plasma should not be a Grimm-type discharge. Indeed, a diode-type discharge is attained with our sample holder, since sputtering is found on the sides and end of the pin sample. The high potential placed on the pin forms the plasma, which is confined by the diameter of the anode (or sleeve). Therefore, despite using a Grimm configuration, the sample holder and source cannot be termed a Grimm-type source since a diode-type discharge results.

A study was attempted to determine the amount of sputtering at the end and surface of the pin. A small piece of non-conductive macor was affixed to the end of the pin to restrict sputtering to the pin surface. Then, a small macor sleeve was machined to fit around the surface of the pin to restrict sputtering to the end of the pin. However, both configurations yielded an unstable discharge, so independent sputtering measurements were unsuccessful.

Despite the pins exhibiting diode plasma characteristics, stable operating conditions were similar to that of a Grimm source. Operating pressures for pin samples were 2 – 6 torr, which are similar to flat sample analysis with a Grimm-type configuration, rather than pin analysis with a DIP (e.g., 0.5 – 1.5 torr).

Sputtering Rate Comparison

The sputtering rate and current density of the pin samples were compared to the corresponding values for flat sample (i.e., Grimm) analysis. Table 7-1 summarizes sputtering characteristics for pin and Grimm samples. The average current of the plasma is proportional to pin length. After determining the average

Table 7-1. Sputtering characteristics for brass pin samples and brass Grimm (flat) samples. Weight loss measurements are based on three sample runs with the standard deviation included to show uncertainty. Sputtering conditions: 2000 V, 3 Torr Ar, 20 ms pulse width, 400 Hz frequency, and sputtering time of 30 min.

Sample	Weight Loss (ΔW) / mg	Avg. Weight Loss / mg	Sputtering Rate (\dot{q}) / ng pulse ⁻¹	Avg. Sputtering Rate/ng pulse ⁻¹	Current Density (J) / ma mm ⁻²
7mm Pin #1	1.081 ± 0.003	1.1070 ± 0.0009	1.500 ± 0.003	1.53 ± 0.03	0.07
7mm Pin #2	1.104 ± 0.001		1.533 ± 0.003		
7mm Pin #3	1.122 ± 0.001		1.558 ± 0.003		
7mm Pin #4	1.1225 ± 0.0001		1.559 ± 0.003		
Average Current: 1.5 _g mA					
Surface Area: 22.8 mm ²					
Grimm #1	0.7162 ± 0.0004	0.7310 ± 0.0003	0.994 ± 0.003	1.02 ± 0.04	0.13
Grimm #2	0.7200 ± 0.0001		1.002 ± 0.003		
Grimm #3	0.7792 ± 0.0008		1.082 ± 0.003		
Grimm #4	0.7087 ± 0.0001		0.984 ± 0.003		
Average Current: 1.5 _g mA					
Surface Area: 12.6 mm ²					

current for flat samples with the Grimm configuration ($\sim 1.5_9$ mA), pin samples were cut to a length (7 mm) that yielded a similar average current ($\sim 1.5_8$ mA) for the same operating conditions. This current normalization allowed direct comparison of the sputtering characteristics corresponding to the two sample types. Each sample was weighed three times to allow standard deviation calculations. The sputtering rate, q (ng/pulse), which was described in Chapter 4, was calculated using:⁶⁰

$$q = \Delta W / (t * f) \quad (\text{Eqn. 7-1})$$

where ΔW (ng) is the amount of sample lost due to sputtering, t (s) is the sputtering time, and f (Hz) is the pulse frequency. Equation 7-1 is often called the net sputter rate, since it takes into account the redeposition effects of the glow discharge process.⁶⁰

As shown in Table 7-1, the average weight loss for the pin samples was higher than the corresponding values for flat samples. The corresponding sputtering rate for pin samples is approximately 50% higher than for Grimm (i.e., flat) samples. Recall, both samples were analyzed with the same operating conditions and the average current was normalized *via* the pin length. The difference between the two sputtering rates (e.g., 1.54 and 1.02 ng/pulse) is attributed to the significantly larger sputtered surface area of the pins compared to the Grimm samples (e.g., 22.8 versus 12.6 mm²). Also, the sample shape likely plays a significant role in the amount of redeposition, which influences the measured sputtering rate. Previous studies in our laboratory have shown that pin samples analyzed using a DIP show rounded edges as a result of reduced redeposition. Due to different surface areas for pin and flat samples, a calculation of current per unit area should give a better

comparison of the two sample types. The current density, J (mA/mm²), of the two sample types was calculated using:

$$J = i / SA \quad (\text{Eqn. 7-2})$$

where i (mA) is the average current of the plasma and SA (mm²) is the surface area of the sample. Despite achieving a higher average sputtering rate, the current density of the pin samples was smaller than the corresponding value for the Grimm samples: 0.07 mA/mm² versus 0.13 mA/mm², respectively.

Matrix Ion Signal

For the pin sample holder to show analytical utility, ion signal intensities should not be compromised for the analysis of pin and wire samples. But, based on the current density calculations shown in the preceding section, the ion signal is predicted to be considerably smaller for pin-type samples. Figure 7-4 and Figure 7-5 show mass spectra collected for both sample configurations (pin- and flat-samples); both samples were machined from the same copper material. The Grimm spectrum in both figures has been horizontally offset for clarity. The average current was normalized for the two sample configurations to allow direct comparison of the mass spectra.

Matrix ion signals (i.e., ⁶³Cu⁺ and ⁶⁵Cu⁺) are higher for flat samples analyzed with a Grimm source, compared to pin samples of the same sample material, analyzed with the sample holder. This ion signal difference, anticipated from the previous current density calculations, is illustrated in Figure 7-4. Assuming comparable ion transport efficiencies for the two sample types, the higher ion signal

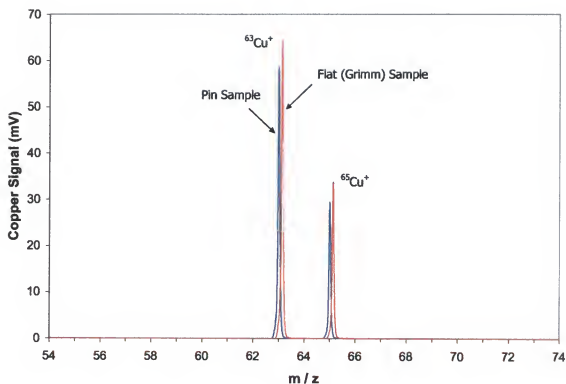


Figure 7-4. Copper signal comparison for a flat and pin sample sputtered at the same average current. Operating conditions (both): 1.3 mA, 3.0 torr, 180 mL/min, 400 Hz pulse frequency, 20 μ s pulse width, -1500 V detector voltage. Voltage: 2.0 kV (pin) and 1.7 kV (flat). Sample: Oxygen-free copper.

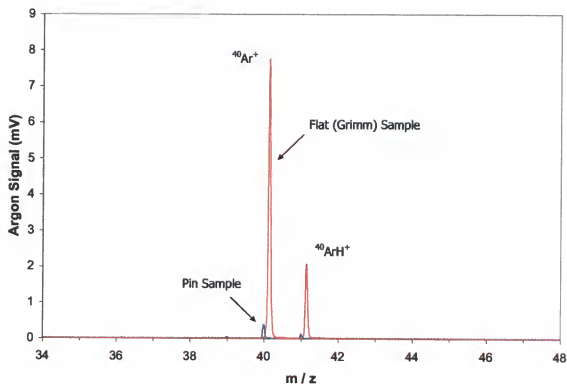


Figure 7-5. Argon signal comparison for a flat and pin sample sputtered at the same average current. Conditions as in Figure 7-4.

results from an increased production of charge carriers (i.e., ions) per unit area with the Grimm-type source. However, the signal is only approximately 10% higher for flat samples, which is considerably smaller than the calculated difference between the current densities (~50%); therefore, the higher current density likely results from a higher population of background ions (i.e., $^{40}\text{Ar}^+$ and $^{40}\text{ArH}^+$) for flat sample analysis with the Grimm source.

The background gas signals were also compared for the two sample types (Figure 7-5). As predicted in the preceding discussion, a higher background ion signal was obtained for flat samples. This result is preferential for pin samples since low background ion signals are desired because these species (e.g., argides, oxides, etc.) can be isobaric interferes. The signal difference between the two sample types for background species is approximately 90%, which is much larger than the corresponding difference in matrix ion signals. Thus, the larger current density of the Grimm type plasma likely originates from a higher formation and subsequent ionization of background species, such as argon.

Detection Limit and Isotope Ratios

The preceding ion signal comparison demonstrated that pin sample analysis with our sample holder provides matrix ion signal intensities similar to those corresponding to flat (i.e., Grimm) samples (see Figure 7-4). Thus, detection limits for the two sample types should be similar also. Figure 7-6 shows a mass spectrum of a NIST 494 standard. Using the $^{123}\text{Sb}^+$ isotope, which is approximately 43% of

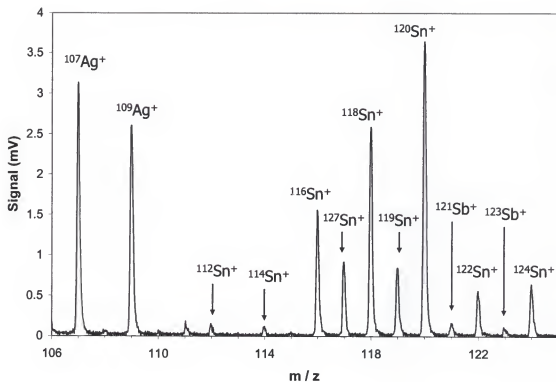


Figure 7-6. Mass spectrum of a pin sample machined from a NIST 494 copper standard. Conditions: 2.0 kV, 1.3 mA, 3.6 torr, 200 mL/min, 400 Hz, 20 μs PW, -2500 V detector voltage, 3 s integration time. Concentrations: Sn - 70 ppm, Sb - 4.5 ppm.

naturally occurring antimony, the limit of detection is calculated to be approximately 50 ppb.

The isotopic precision was also calculated for the pin source. The simultaneous sampling of TOF makes it well-suited for isotope analysis, as described in Chapter 5. Referring to Figure 7-6, the measured tin 120/116, 118/116, and 120/118 ratios are 2.3₄, 1.6₆, and 1.4₀, respectively. These values are comparable to the nominal ratios of 2.242₉, 1.667₅, and 1.328₅, respectively.¹²⁸

Molecular Interferences

King and others have reported on polyatomic interferences found in GDMS.^{133,142-144} While these interferences can hinder the detection of sample ions, temporal resolution methods have largely circumvented these hindrances.³⁸ Not surprisingly, pin samples analyzed with our sample holder often exhibited mass spectral interferences similar to those previously reported for other GD sources. Figure 7-7 shows mass spectra collected with pin- and flat-samples, both machined from the same copper ingot. The Grimm spectrum in Figure 7-7 has been shifted horizontally for clarity. The pin sample spectrum shows polyatomic copper species that are increased by approximately 85% compared to the corresponding Grimm spectrum. For example, the signal for the most abundant copper dimer ($^{63}\text{Cu}_2^+$) is 1.5 mV and 0.2 mV for the pin and flat sample, respectively. The copper dimer peak assignments and ratios shown in Figure 7-7 were verified against software capable of modeling polyatomic species based on isotopic abundances (Isopro 3.0, Sunnyvale, California, USA), as shown in Figure 7-8.

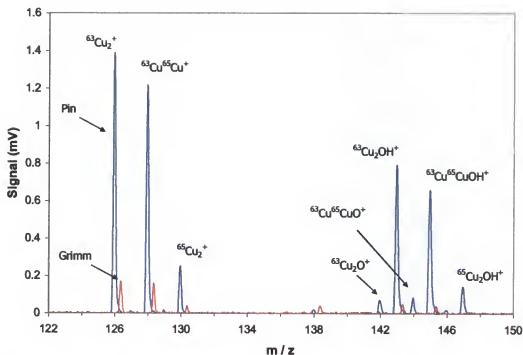


Figure 7-7. Signal comparison for a flat and pin sample sputtered at the same average current. Operating conditions (both): 1.3 mA, 3.0 torr, 180 mL/min, 400 Hz pulse frequency, 20 μ s pulse width, -2200 V detector voltage. Voltage: 2.0 kV (pin) and 1.7 kV (flat). Sample: Oxygen-free copper.

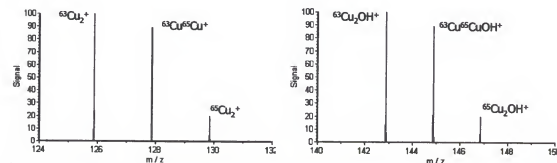


Figure 7-8. Theoretical mass spectra verifying the copper dimer peak assignments in Figure 7-7.

Mass spectra collected of pin samples using our sample holder also exhibited additional interferences that were not found with flat sample analysis using a Grimm source. Figure 7-9 shows mass spectra collected with the pin and Grimm source for an O₂-free copper sample. The spectrum corresponding to flat sample analysis by the Grimm source is void of peaks within this 18 AMU region, whereas the pin spectrum exhibits many polyatomic copper peaks. The assignments of these copper trimer species were verified, as shown in the theoretical mass spectra of Figure 7-10.

The copper-oxide interferences shown in Figure 7-9 can hinder the detection of trace lead. Figure 7-11 shows a mass spectrum of a NIST 494 copper pin sample containing 26 ppm lead. The polyatomic copper-oxide peak at m/z 207 ($^{63}\text{Cu}_2^{65}\text{CuO}^+$) overlaps the lead isotope; also, the hydrides of these polyatomic copper-oxides (Cu_xOH^+) could interfere with other lead isotopes.

Operating conditions of the pin discharge were studied for their effect on these polyatomic species. The pressure within the source was the only operating parameter that significantly affected their signal levels. Figure 7-12 shows mass spectra collected over a range of delay (sampling) times for a copper pin sample. These spectra, collected at a source pressure of 3.0 torr, exhibit the copper oxide interferences shown previously in Figure 7-11. Increasing the pressure within the source minimizes these interferences, as shown in Figure 7-13 for spectra collected at 4.5 torr. Spectra are displayed as a function of delay time to ensure the polyatomic species have been suppressed rather than shifted to longer sampling delay times as a function of increasing pressure.

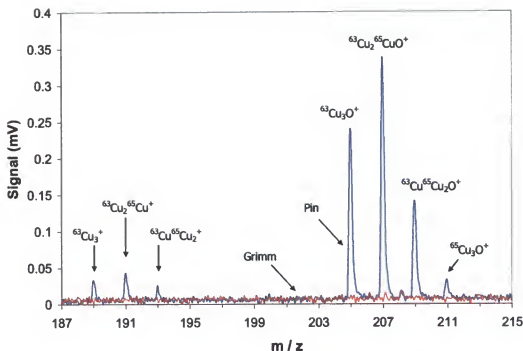


Figure 7-9. Signal comparison for a flat and pin sample sputtered at the same average current. Conditions as in Figure 7-7.

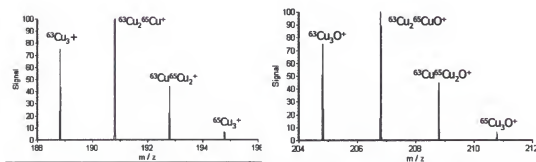


Figure 7-10. Theoretical mass spectra verifying the copper trimer peak assignments in Figure 7-9.

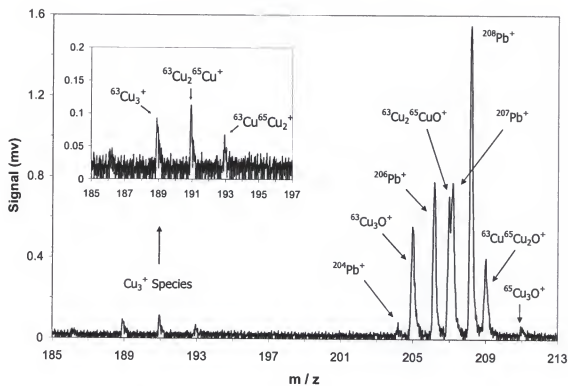


Figure 7-11. Mass spectrum showing the hindrance of lead detection due to copper trimer isobaric interferences. Conditions as in Figure 7-7.

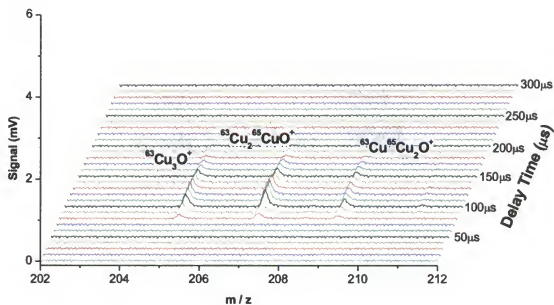


Figure 7-12. Mass spectra collected at 3.0 torr showing copper polyatomic species. Operating conditions: 2.0 kV, 3.0 torr, 180 mL/min, 400 Hz pulse frequency, 20 μs pulse width, -2200 V detector voltage. Sample: Oxygen-free copper (3 mm pin).

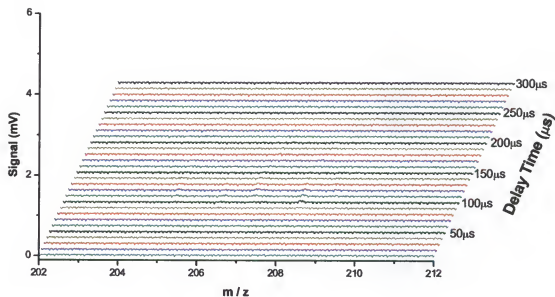


Figure 7-13. Mass spectra collected at 4.5 torr showing reduction of copper polyatomic species with higher operating pressures. Operating conditions: 2.0 kV, 4.5 torr, 180 mL/min, 400 Hz pulse frequency, 20 μ s pulse width, -2200 V detector voltage. Sample: Oxygen-free copper (3 mm pin).

The results in the preceding discussion indicate that high operating pressures reduce polyatomic interferences. This pressure (e.g., 4.5 torr) is practical only if the matrix (sample) signal is not simultaneously reduced. Increasing the source pressure could result in less sample ion extraction due to a reduced mean free path, and subsequently a smaller matrix ion signal. Figure 7-14 and Figure 7-15 show mass spectra of matrix signal (e.g., copper) collected at 3.0 and 4.5 torr, respectively. The copper ion signal levels are similar for both operating pressures, suggesting similar Cu^+ extractions for both pressure regimes. Thus, increasing the pressure leads to more effective dissociation of the polyatomic interferences, rather than less ion extraction.

The operating pressure affects the temporal response of the sputtered ion signal. The maximum $^{63}\text{Cu}^+$ signal shifts from 140 μs to 170 μs for a pressure increase from 3.0 to 4.5 torr, as seen in Figures 7-14 and 7-15. This increased sampling time is due to more collisions at higher pressures (i.e., smaller mean free paths). Since the overall signal is not significantly affected, the pin sample holder is preferentially operated at high pressures (compared to the Grimm) to minimize polyatomic interferences.

Temporal Resolution

An advantage of the pulsed GD source is its inherent decoupling of the two types of discharge species: gaseous discharge components (e.g., argon, trace water vapor, etc.) and sputtered cathode material (e.g., copper). This phenomenon allows separation of discharge gas species from sputtered sample ions when the pulsed

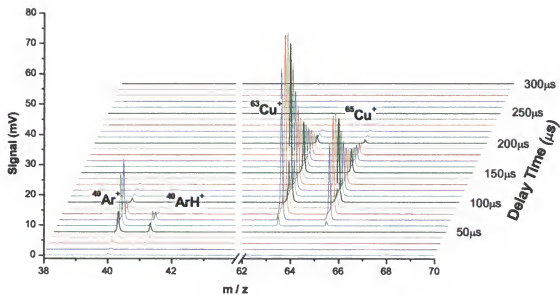


Figure 7-14. Mass spectra collected at 3.0 torr showing argon and copper ion signals. Conditions as in Figure 7-12, except detector voltage (-1500 V rather than -2200 V).

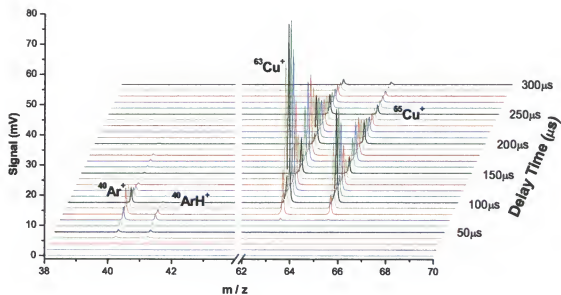


Figure 7-15. Mass spectra collected at 3.0 torr showing argon and copper ion signals. Conditions as in Figure 7-14, except detector voltage (-1500 V rather than -2200 V).

ionization source is coupled to a TOFMS. The effectiveness of this temporal resolution was shown in Chapter 6 by detecting magnesium in the presence of background contaminants. The ability of the pin sample holder to temporally resolve ions was compared to these previous studies, as shown in Figures 7-14 and 7-15. Our pin sample holder allows temporal resolution that is comparable to that previously shown with flat- and pin-sample analysis using a Grimm and diode configuration, respectively.^{37,141} Figure 7-14 shows that background discharge gas species (e.g., $^{40}\text{Ar}^+$ and $^{40}\text{ArH}^+$) subside by a delay time of 150 μs , yet sample ions (e.g., $^{63}\text{Cu}^+$ and $^{65}\text{Cu}^+$) are sustained beyond this sampling time.

Pin Length

Hang and colleagues studied the effect of cathode-to-orifice (C-O) distance for pin samples using a DIP.¹³³ Mass spectra were collected as a function of distance from the sample to the skimmer orifice. The sample length remained unchanged for all measurements since the distance was changed *via* axial probe movement. Increasing the C-O distance resulted in longer diffusion times and smaller sample ion signals. The diffusion time and signal levels for discharge gas ions were unaffected by distance changes.

Cathode-to-orifice distances have also been studied for pin samples using our sample holder. Figure 7-16 shows maximum ion signal as a function of pin length for a series of copper pin samples. Discharge gas species are represented by $^{40}\text{Ar}^+$ signal, while sample ions are represented by $^{63}\text{Cu}^+$. The profiles in Figure 7-16 appear to contradict the trends discussed by Hang and colleagues. For example,

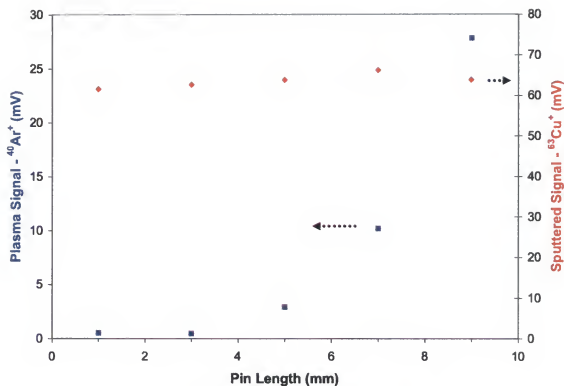


Figure 7-16. Ion signal as a function of pin length. Operating conditions: 2.0 kV, 3.0 torr, 180 mL/min, 400 Hz pulse frequency, 20 μs pulse width, -1500 V detector voltage. Sample: Oxygen-free copper.

Figure 7-16 shows that copper is only marginally affected by C-O distance (i.e., pin length), while argon signal decreases as the C-O distance is decreased. The contrast between the Hang's experimental results and those shown here is explained by sample length. The C-O distance in Figure 7-16 is changed by altering the pin length. The average current increases linearly as a function of pin length due to a higher population charge carriers, as shown in Figure 7-17. In the experiments by Hang, the sample length was unchanged; only the probe position was changed to vary C-O distances.

The results of Figure 7-16 demonstrate that short pins are preferential for analyses in which isobaric interferences are a concern. Since the argon signal is suppressed at shorter pin lengths and the copper signal is relatively uniform, pin lengths approximately 1 to 3 mm should be used. This result is promising for analyses in which only small amounts of sample material are available.

Pin Sample Application

The Grimm source is valuable for depth profiling due to its planar sputtering of the sample surface. Likewise, the microsecond pulsed GD has shown advantages for depth profiling applications. This operational mode applies a short term, repetitive pulse to strip atoms from successive sample layers. The ability to control the pulse width and pulse frequency is a benefit not available in direct current (dc) operation. Thin films that would be removed immediately with dc operation show extended sputter removal times with a microsecond-pulsed GD.

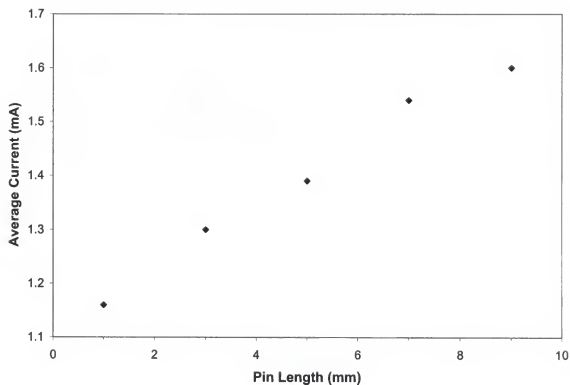


Figure 7-17. Plot showing linear dependence of average current on pin length. Operating conditions: 2.0 kV, 3.0 torr, 180 mL/min, 400 Hz pulse frequency, 20 μ s pulse width, -1500 V detector voltage. Sample: Oxygen-free copper.

Depth profiling of non-flat samples is not a routine application for the DIP configuration, unlike the established ability of the Grimm source (e.g., planar sputtering, quick sample interchange, etc.). However, depth profiling is readily applicable to pin samples using our sample holder. Figure 7-18 and Figure 7-19 show mass spectra as a function of sputter time for a 3 mm segment of a paper clip. Figure 7-18 shows the nickel and iron isotope region, and Figure 7-19 represents the cadmium isotopic region. The mass spectrum of Figure 7-18 reveals the standard isotopic pattern of Ni. Small ion signals corresponding to iron are found at 54, 56, and 58 AMU. The spectrum in Figure 7-19 shows the nominal isotopic pattern for major Cd isotopes at two minutes. As sputtering proceeds, the iron signal increases with a corresponding decrease in nickel signal, as shown in Figure 7-18. The cadmium ion signal shown in Figure 7-19 decreases after reaching a maximum at 3 minutes. With continuous sputtering, the nickel and cadmium isotopes have fallen to nearly baseline, while the iron signals achieve maximum values. A two-dimensional profile was also constructed using data extracted from these two plots (Figure 7-18 and Figure 7-19), as shown in Figure 7-20.

The microsecond pulsed mode allowed a slow, controlled removal rate of the sample. This revealed the paper clip had a thin, chemically resistant Ni-Cd coating deposited onto the iron substrate. More importantly, this example demonstrates that depth profiling of pin samples is possible. Our pin sample holder allows thin layer analysis, as routine as for flat sample analysis with a Grimm-type source.

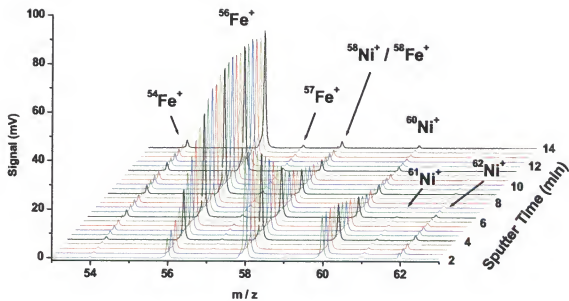


Figure 7-18. Mass spectra collected as a function of sputtering time for a 3 mm portion of a paper clip. Operating conditions: 2.0 kV, 3.0 torr, 180 mL/min, 400 Hz pulse frequency, 20 μ s pulse width, -1500 V detector voltage.

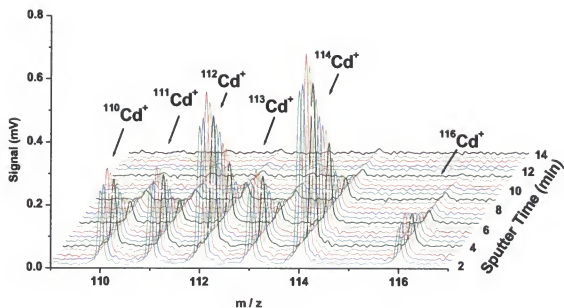


Figure 7-19. Mass spectra collected as a function of sputtering time for a 3 mm portion of a paper clip. Operating conditions: 2.0 kV, 3.0 torr, 180 mL/min, 400 Hz pulse frequency, 20 μ s pulse width, -2200 V detector voltage.

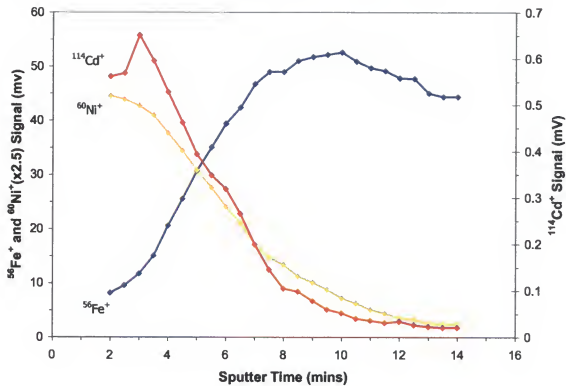


Figure 7-20. Two-dimensional profile of selected isotopes for the paper clip analysis shown in Figure 7-18 and Figure 7-19.

Concluding Remarks

We have described a new sample holder that allows direct analysis of pin samples on a Grimm-type source. Easy sample interchange and good precision - inherent advantages of the Grimm source - are also characteristic of this sample holder. Operating conditions of the pin sample holder are similar to those employed for Grimm-type flat-sample analysis rather than traditional pin analysis with a probe configuration (e.g., DIP). The figures of merit for this source, such as detection limit and isotopic precision, are comparable to standard Grimm and diode glow discharge configurations. Polyatomic interferences are higher compared to those found with a Grimm source, but high operating pressures helped dissociate these polyatomic species. Depth profiling of a pin sample, consisting of a thin Ni-Cd coating on a steel substrate, shows promise as a complementary application of our sample holder. The pulsed glow discharge mode allowed temporal resolution comparable to previous GD configurations.

CHAPTER 8 THIN FILM ANALYSIS WITH A MICROSECOND PULSED GLOW DISCHARGE TIME-OF-FLIGHT MASS SPECTROMETER

Introduction

The glow discharge (GD) has developed into a mature technique for atomic emission spectrometry (AES), and glow discharge mass spectrometry (GDMS) has long supplanted spark source mass spectrometry as the leading technique for trace elemental analysis of solid samples. Glow discharge atomic emission spectrometers (GD-AES) have found their niche as an established method for probing spatial information (i.e., depth profiling) of solid samples, as illustrated in Chapter 4 and other references.^{60,83,87,88} Glow discharge mass spectrometers, on the other hand, have been generally limited to bulk analyses, due to their established source configuration. A direct insertion probe (DIP) is employed in most GDMS experiments,^{71,77,82} in which a pin or disc sample is placed on the end of a probe, as described in Chapter 3 (see Figure 3-2). Planar sputtering is not readily achieved with a probe configuration, which can impede depth profiling applications.

The Grimm-type GD source, an alternative to the DIP configuration, has become an established configuration for GD-AES.^{80,82,84,85} The design and operation of the Grimm source (see Figure 3-3) has been described throughout this dissertation. Two prominent advantages of this source configuration include precise sample placement and external sample mounting, which are not available with a probe configuration. The confined nature of a Grimm-type plasma affords planar

sputtering, and given the proper operating conditions, depth profiling applications can be realized. Indeed, these profiling capabilities have largely contributed to the success of GD-AES, which exclusively utilizes a Grimm-type configuration.

Despite the popularity of depth profiling *via* GD, only a handful of publications have described the feasibility of GDMS for acquiring spatial and depth information.^{110,112,145-147} Existing techniques that prove well-suited for this application, such as GD-AES, can be considered one factor in this lack of appeal. Convection effects, which are typically not a significant concern in emission spectroscopy, can hinder the ability of the mass spectrometer to distinguish ions originating from separate sample layers. Another contributor is the established source configuration for GDMS - the DIP - which does not afford planar sputtering. Converting the source from a DIP to a Grimm-type configuration is one remedy, though this combination has found little appeal as a GDMS source. High ion transport efficiency, which is crucial to the success of mass spectrometry, has been difficult to obtain with this source.

Chapter 6 described ion transport diagnostics for a microsecond pulsed Grimm-type GD source and time-of-flight mass spectrometer (TOFMS) system. Operating parameters (e.g., flow rate and pressure) and the configuration of the Grimm source were found to influence ion transfer efficiency. Optimizing these conditions provided ion signals that were comparable to DIP-based mass spectrometers. This ion transport study proved beneficial for the evaluation of Grimm-type GDMS depth profiling described in this chapter.

Chapter 4 described the use of a microsecond pulsed GD-AES system for thin film analysis. The transient nature of the discharge provided a slow, controlled removal rate, which allowed the analysis of thin films in the nm-regime. This benefit was only achieved after properly choosing operating conditions (e.g., pressure and voltage) that gave flat, well-defined sputter craters. The results from this study also proved beneficial for the evaluation of GDMS depth profiling.

In the current dissertation, we evaluate the feasibility of thin layer analysis using a microsecond pulsed Grimm-type GD-TOFMS. We establish this goal by merging our established GD-TOFMS ion transport conditions (Chapter 6) with GD-AES operating parameters that yield good depth resolution (Chapter 4). Depth profiling experiments in other laboratories have reported the analysis of thin films down to 1 μm with a GD-TOFMS.¹⁴⁵ Most GDMS depth profiling applications have employed a GD operated in the continuous, direct current (dc) mode.^{110,112,145-147} We show that the use of a microsecond pulsed GD, operated under optimized conditions, allows reproducible profiling of coatings less than 10 nm. Also shown is the analysis of multiple-layered samples (e.g., spent computer hard discs) and the ability to obtain quantitative depth information.

Experimental

Glow Discharge Source and Time-of-Flight Mass Spectrometer

The glow discharge source employed in this research, an in-house designed Grimm-type configuration operated in the microsecond pulsed mode, was described previously in Chapter 5. The mass spectrometer, a commercial time-of-flight

instrument (Renaissance, LECO Corporation, St. Joseph, Michigan, USA), was also described in Chapter 5. Refer to Figure 5-6 and Figure 5-9 for a schematic of the GD source and TOFMS, respectively.

A special feature of the software (LECO Renaissance version 1.16, LECO Corporation, St. Joseph, Michigan, USA), transient signal collection, was employed. Essentially, this operational feature allowed successive mass spectra to be collected with a spectral frequency dependent on the integration time. Employing this collection mode allows the GD-TOFMS to obtain depth information in a manner analogous to GD-AES operation. A profile was obtained by plotting the maximum ion signal of each isotope for successive mass spectra as a function of sputtering time. Using this protocol reveals intensity-time profiles similar to those shown in Chapter 4, which were collected with GD-AES.

Sample Material

Silicon samples used in this experiment were commercial N-type, prime grade wafers (Silicon Sense, Nashua, New Hampshire, USA) with a diameter of 525 ± 25 μm and resistance of $0.02 - 0.06$ $\text{ohm}\cdot\text{cm}$. High-purity gold (Anatech Ltd., Orange, Massachusetts, USA) was used for depositing thin layers onto the silicon wafers. The multi-layered sample was a spent computer hard disc (Quantum Corp., Milpitas, California, USA).

Results and Discussion

Sample Fabrication

Depth profiling standards with micron-deposited coatings are commercially available (Kocour Co., Chicago, Illinois, USA) and are commonly used to test the constraints of a continuous, dc GD. The microsecond pulsed GD, however, has shown the ability to analyze nm-sized coatings, which are not commercially available. Hence, we fabricated our own pseudo-standards to examine the depth profiling abilities of our microsecond pulsed GD-TOFMS.

Depth profiling samples were manufactured using a commercial sputtering deposition system (Hummer 6, Anatech Ltd., Orange, Massachusetts, USA). This instrument was used to deposit a controlled amount of high-purity gold on silicon wafers, which provided a polished surface well-suited for uniform deposition. The amount of gold deposited onto the silicon wafer was controlled *via* deposition time. The sputtering system did not provide the ability to control the thickness of deposition directly; therefore, a correlation between deposition time and gold thickness was established, as described in the next section.

Gold Thickness

Scanning electron microscope. Correlating the gold thickness and deposition time was first established using a scanning electron microscope (SEM). Gold was deposited onto the silicon surface and a commercial field emission SEM (Model: JSM-6330F, JEOL USA, Peabody, Massachusetts, USA) was used to estimate the thickness of the gold coating. Figure 8-1 shows an SEM profile of a

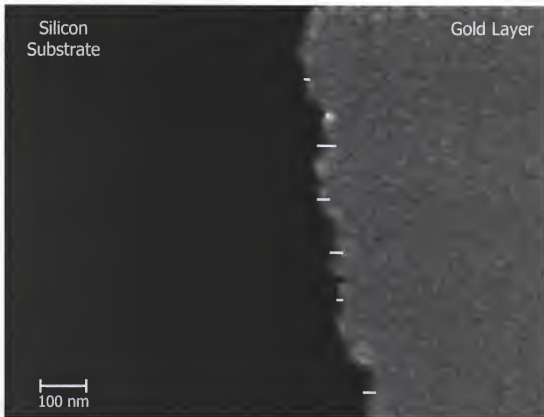


Figure 8-1. SEM of gold deposited onto a silicon substrate. Plasma deposition conditions: 15 mA and 60 mtorr for 15 minutes. SEM conditions: 15.0 kV and 100,000x magnification.

silicon substrate after 15 minutes of gold deposition (100,000x magnification). The sample was affixed to a slanted mounting block which allowed the collection of SEM profiles at an angle, as shown in Figure 8-1. The dark segment of this SEM shows a portion of the silicon substrate that is void of gold deposition, while the lighter section represents the reflective gold surface.

The thickness of the gold layer was measured at six arbitrary positions across the edge of the gold surface, as shown by horizontal white lines in Figure 8-1. The average length of the six lines was 3.48 ± 0.72 mm, which converts to approximately 26.8 ± 5.5 nm based on the conversion scale (i.e., 13 mm = 100 nm). Recall, this average thickness (i.e., 26.8 nm) corresponds to 15 minutes of gold deposition; therefore, the rate deposition rate is approximately 1.8 nm per minute of deposition.

Weight measurements. The deposition rate estimated with SEM measurements (1.8 nm / minute) was verified with a second technique. First, five small pieces of clean silicon (i.e., no gold deposition) were weighed with a microbalance (Model: M2P, Sartorius Corp., Edgewood, New York, USA), as shown in Table 8-1. The wafers were then deposited with gold for ten minutes and re-weighed. The weight of gold deposited was then calculated based on the pre- and post-weight measurements. The mass of gold deposited onto the silicon surface (ΔW - mg) can be converted to thickness (T - nm) using:

$$T = \Delta W / (\rho_{Au} * SA) \quad (\text{Eqn. 8-1})$$

Table 8-1. Weight loss measurements for gold deposited onto a silicon substrate. Deposition conditions: 15 mA, 60 mtorr, 10 minute deposition.

Sample (SA / mm ²)	Pre-Dep. Wt. / mg	Avg. Wt. / mg	Post-Dep. Wt. / mg	Avg. Wt. / mg	Wt. Change (ΔW) / mg	Gold Thickness (T) / nm
Silicon 1 (80.35)	93.019	93.0203 \pm 0.0015	93.052	93.0530 \pm 0.0014	0.033	21.0
	93.022		93.054			
	93.020		93.051			
Silicon 2 (110.71)	129.469	129.4700 \pm 0.0010	129.521	129.5225 \pm 0.0021	0.052	24.5
	129.471		129.524			
	129.470		129.520			
Silicon 3 (63.04)	74.548	74.5493 \pm 0.0015	74.579	74.5775 \pm 0.0021	0.028	23.1
	74.549		74.576			
	74.551		74.577			
Silicon 4 (68.49)	75.721	75.7200 \pm 0.0026	75.750	75.7515 \pm 0.0021	0.032	23.8
	75.717		75.753			
	75.722		75.756			
Silicon 5 (74.91)	88.065	88.0640 \pm 0.0010	88.100	88.1005 \pm 0.0007	0.036	25.2
	88.064		88.101			
	88.063		88.098			

where, ρ_{Au} (g/mL) is the density of gold and SA (mm^2) is surface area. Using Equation 8-1, the average thickness of gold for the five samples is approximately 23.5 ± 1.6 nm, which converts to 2.4 ± 0.2 nm of gold deposited per minute of sputtering.

The estimated deposition rates were similar for the SEM profiles (1.8 nm) and weight measurements (2.4 nm). The small discrepancy between the two values is characteristic of such thin layers and likely arises from a combination of (1) non-uniform deposition and (2) measurement uncertainties. In summary, the results from the two techniques were averaged (~ 2.0 nm/min) and used to estimate the gold thicknesses listed throughout this chapter.

Parametric Studies

Pulse voltage. The effect of pulse voltage on intensity-time profiles has been investigated for a microsecond pulsed GD-AES system.⁹⁰ Temporal profiles collected at low voltages (e.g., 800 V) were plagued by broad transitions on the rising and falling edges of the surface coating, while high pulse voltages (e.g., 2 kV) yielded temporal profiles that were too narrow (i.e., the coating was stripped too rapidly). The result of these temporal profiles is the formation of poor sputter craters and unoptimized depth profiling, as discussed in Chapter 4 (see Figure 4-3 and Figure 4-4). Only intermediate pulse voltages (e.g., 1.2 – 1.4 kV) provided optimum temporal profiles and well-defined crater profiles.

A similar voltage study was examined with our microsecond pulsed GD-TOFMS. Figure 8-2 shows a temporal profile collected at a pulse voltage of 1.2 and

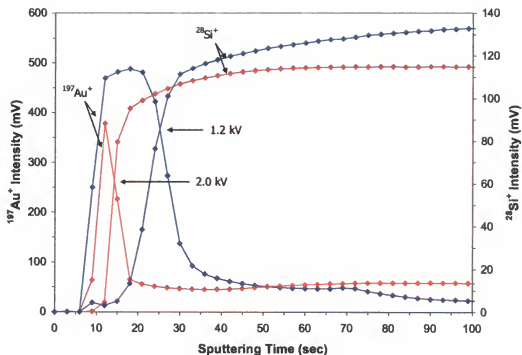


Figure 8-2. Intensity-time plots obtained at an operating voltage of 1.2 and 2.0 kV for an 8 nm gold film deposited onto a silicon substrate. Operating conditions: 0.7 mA (1.2 kV) and 1.5 mA (2.0 kV), 3.0 torr, 250 mL/min, 400 Hz, 20 μs PW, -1600 V detector voltage, 3 s integration time.

2.0 kV for a thin layer of gold (~8 nm) deposited onto silicon. The results were similar to those observed previously with a pulsed GD-AES experiment.⁹⁰ At low operating voltages (e.g., 1.2 kV), the sputter rate is minimized and a broad profile corresponding to gold is found, as shown in Figure 8-2. Operating at high pulse voltages (e.g., 2.0 kV) provides an elevated sputtering rate and rapid removal of the gold layer. For the analysis of thin films, the temporal profile of the coating (e.g., gold) should be expansive, but not so much as to prematurely expose the underlying silicon wafer. Optimum temporal profiles were obtained for intermediate pulse voltages between 1.4 and 1.6 kV.

Source Pressure. The argon gas pressure is also an important parameter in depth profiling experiments. The pressure determines (1) the mean free path within the glow discharge cell and (2) the discharge current under constant pulse voltage conditions. Yang et al. reported that operating pressures between 3.0 to 4.0 torr provided the best depth resolution for GD-AES experiments.⁹⁰

The effect of pressure was examined with our GD-TOFMS system, as shown in Figure 8-3. The rising and falling slopes in this figure are not significantly affected by altering the source pressure, which is in accord with previous AES results.⁹⁰ The effect of pressure in Figure 8-3 is only minor, as evidenced by the overlapping crossing points at 2.5 and 5.0 torr in Figure 8-3. This result contradicts findings with AES, which exhibit a considerable dependency on source pressure (i.e., significant crossing point differences). Elevated currents are obtained by increasing the source

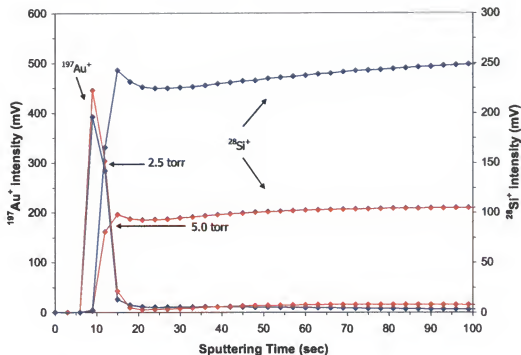


Figure 8-3. Intensity-time plots obtained at an argon pressure of 2.5 and 5.0 torr for an 8 nm gold film deposited onto a silicon substrate. Operating conditions: 1.6 kV, 1.8 mA (2.5 torr) and 2.5 mA (5.0 torr), 250 mL/min, 400 Hz, 20 μs PW, -1600 V detector voltage, 3 s integration time.

pressure at constant voltage. The increased current provides a high energy plasma with enhanced sputtering rates, despite a simultaneous increase in sample redeposition due to shorter mean free paths. At these elevated pressures, layer interfaces are realized prematurely in accord with enhanced sputtering rates, as found in AES measurements.⁹⁰ This effect for operating pressures is not seen in Figure 8-3, however, which shows similar crossing points for both operating pressures (e.g., 2.5 and 5.0 torr). The difference in the AES and MS experimental results is due to the effect mean free path and ion transport can have on these techniques. Ions must be transported to a sampling region in MS, unlike AES which relies on 'self-transporting' photons. Operating our TOFMS with elevated pressures (e.g., 5.0 torr) results in extended ion migration times, and consequently expanded temporal profiles. Offsetting this profile expansion are higher currents and sputtering rates (at elevated pressures), which reduces the temporal profile width by enhanced depletion. Therefore, the narrow temporal profile that should be obtained at high operating pressures (as obtained in AES), is offset by the extended migration times. Profiles that exhibit similar crossing points in MS for all stable operating pressures are the result.

Pulse Frequency. An advantage of the microsecond pulsed GD is the ability to control the amount of sputtering by altering the pulse frequency, as described in Chapter 3. Previous AES results have shown that the pulse frequency can be changed to alter the amount sample removed without affecting the resultant crater profile.⁶⁰ Figure 8-4 shows the effect of pulse frequency obtained with our GD-

TOFMS. Operating at high pulse frequencies (e.g., 500 Hz) leads to rapid gold sputtering and a narrow temporal profile similar to that obtained at a high pulse voltage (Figure 8-2). Reducing the pulse frequency to 200Hz slows the sputtering and provides an expanded gold profile, as shown in Figure 8-4. An intermediate pulse frequency of 400 Hz provided a good compromise.

Pulse Width. Another operating parameter of the microsecond pulsed GD that provides control over the sputtering rate is the pulse width of the applied voltage, as described in Chapter 3. Figure 8-5 shows the effect pulse width (10 and 50 μ s) has on thin film temporal profiles. Like operating at high pulse frequencies, using an extended pulse width (e.g., 50 μ s) increases the amount of sputtering and shortens the temporal profile of the coating. Conversely, shorter pulse widths (e.g., 10 μ s) yield expanded profiles due to reduced sputtering.

Thickness Limit

The minimum coating thickness that we can profile with our microsecond pulsed GD-TOFMS was determined. Previous depth profiling measurements using GDMS have shown the successful analysis of coatings down to apparently 1 μ m.¹⁴⁵ Figure 8-6 shows nine profiles collected from the analysis of an 8 nm gold layer deposited onto a silicon substrate. A photo of the analyzed silicon wafer is presented in Figure 8-7, which shows the nine positions analyzed. The crossing point precision in Figure 8-7 was 17.5 ± 0.4 s, which is quite good for such thin sample layers. This result indicates the technique is capable of analyzing coatings

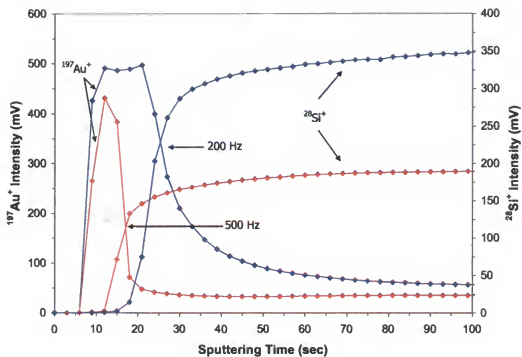


Figure 8-4. Intensity-time plots obtained at a pulse frequency of 200 and 500 Hz for an 8 nm gold film deposited onto a silicon substrate. Operating conditions: 1.6 kV, 0.4 mA (200 Hz) and 1.3 mA (500 Hz), 3.0 torr, 250 mL/min, 20 μs PW, -1600 detector voltage, 3 s integration time.

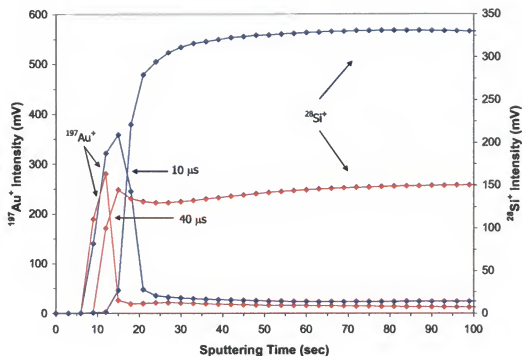


Figure 8-5. Intensity-time plots obtained at a pulse width of 10 and 40 μs for an 8 nm gold film deposited onto a silicon substrate. Operating conditions: 1.6 kV, 1.1 mA (10 μs) and 3.2 mA (40 μs), 3.0 torr, 250 mL/min, 400Hz, -1600 V detector voltage, 3 s integration time.

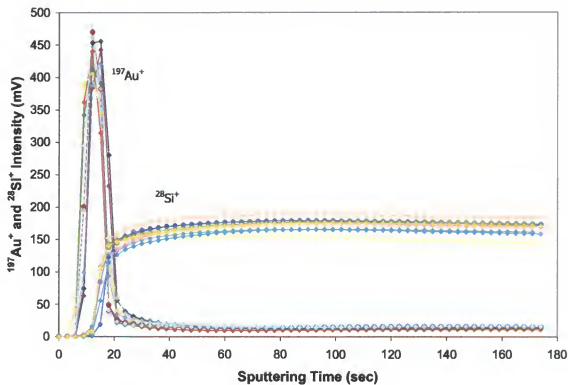


Figure 8-6. Nine intensity-time plots obtained for an 8 nm gold film deposited onto a silicon substrate. Operating conditions: 1.6 kV, 1.1 mA, 3.0 torr, 250 mL/min, 400 Hz pulse frequency, 10 μs pulse width, -1600 detector voltage, 3 s integration time.

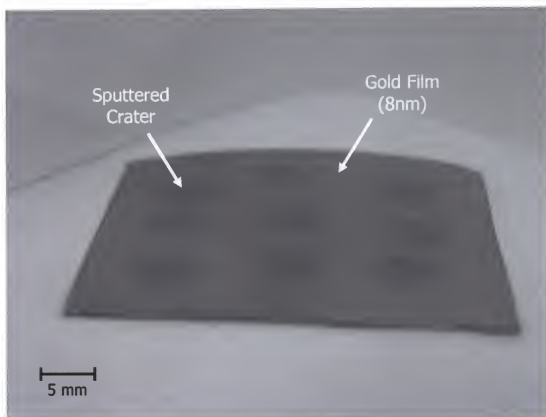


Figure 8-7. Photo showing nine successive depth profiling craters of a thin gold coating (8 nm) deposited onto a silicon wafer.

approximately 8 nm thick. The analysis of layers less than 8 nm were less reproducible, as shown in the next section.

Calibration Curve

Figure 8-8 is a calibration curve showing the lower range of thin layers (4 – 12 nm) that can be measured with our microsecond pulsed GD-TOFMS. Three replicates of each analysis were performed to allow uncertainty measurements. The precision becomes poor at gold layers less than 8 nm, as shown by the large error bars associated with 4 and 6 nm. The calibration curve in Figure 8-8 allows conversion of the previous intensity-time profiles into profiles displaying elemental concentration as a function of sputtered depth.

Quantitative Conversion

The gold-silicon profiles presented up to this point represent intensity-time profiles. However, the information desired is generally extracted from a quantified version of these profiles. Quantification is achieved by converting (1) elemental intensities to concentration, and (2) sputtered time to sputtered depth. After conversion, the concentration of a thin layer in the sample can be monitored at varying depths of the sample. Quantitative methods have been described for atomic emission measurements employing a direct current (dc),¹⁰⁸ radio-frequency (rf),¹⁰⁹ and microsecond pulsed glow discharge source.⁶⁰ The data collected with our GD-TOFMS can also be quantified by using the calibration curve shown in Figure 8-8.

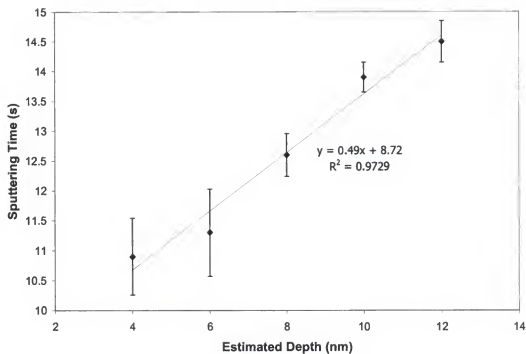


Figure 8-8. Calibration curve obtained for the analysis of five gold coatings varying in thickness. Triplicate measurements were collected for each depth as shown by the error bars.

The first step in this quantitative conversion is to collect a raw plot, such as the intensity-time plot shown in Figure 8-9 for a 10 nm gold coating deposited onto a silicon wafer. This plot shows gold and silicon ion intensity as a function of sputtering time. The next step is to convert the sputtered time values to units of sputtering depth. Conversion is accomplished by using a modified version of the calibration curve equation (as seen in Figure 8-8):

$$d = (t - 8.72) / 0.49 \quad (\text{Eqn. 8-2})$$

where d (nm) is the calculated sputtered depth and t (s) is the sputter time. Each value of sputter time is converted to its corresponding depth using Equation 8-2. The result of this conversion is shown in Figure 8-10, which shows a profile of ion intensity as a function of depth.

The final step in quantitation is to convert the intensity values to concentration, which is done by normalizing all of the intensities with respect to the highest intensity value, as described previously in Chapter 4. The result of this conversion for the gold-silicon sample is shown in Figure 8-11. The estimated depth of this gold layer is 12.8 nm, which is similar to the nominal gold thickness of 10 nm. This quantified plot provides more valuable information than the time-intensity plot, as it allows elemental concentration to be monitored as the sample is being analyzed (i.e., sputtered).

Simultaneous mass spectra collection

The depth profiles that have been shown throughout this chapter are based on a transient collection of mass spectra, as described previously in the

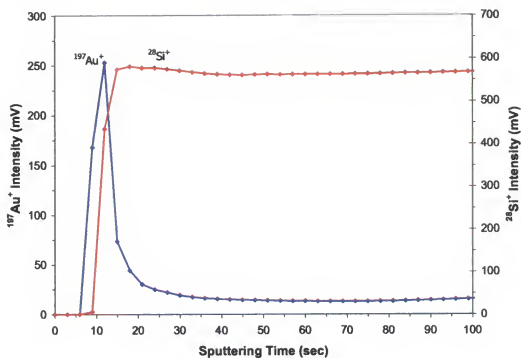


Figure 8-9. Qualitative intensity-time plot obtained for a 10 nm gold film deposited onto a silicon substrate. Operating conditions: 1.6 kV, 1.0 mA, 3.0 torr, 250 mL/min, 10 μs pulse width, 400 Hz pulse frequency, -1600 V detector voltage, 3 s integration time.

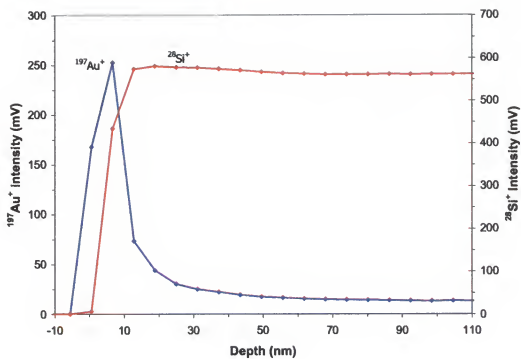


Figure 8-10. Intensity-depth plot from Figure 8-9 of a 10 nm gold film deposited onto a silicon substrate.

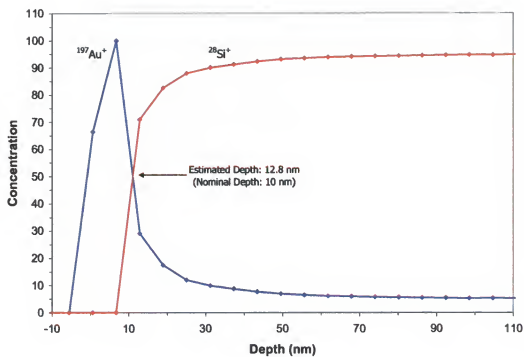


Figure 8-11. Concentration-depth plot from Figure 8-9 of a 10 nm gold film deposited onto a silicon substrate.

experimental section. The individual collection of mass spectra provides an opportunity that is not available to GD-AES depth profiling measurements. Each point comprising a full depth profile corresponds to one mass spectrum. After completion of the analysis, each individual mass spectrum can be retrieved for additional information pertaining to the sample. For example, trace impurities that can contaminate sample layers are easily seen with the individual mass spectra.

Figure 8-12 shows a temporal profile obtained for the analysis of a copper layer deposited onto a zinc substrate. A particular point can be chosen on this profile and a mass spectrum corresponding to this time of the analysis can be displayed. For example, a point was chosen in Figure 8-12 after approximately 100 seconds of sputtering, as indicated by the arrow. The corresponding mass spectrum was retrieved (as shown in the subset), which shows a high copper ion signal (i.e., $^{63}\text{Cu}^+$ and $^{65}\text{Cu}^+$) with no signal corresponding to zinc. It should be noted that a small background (~ 0.9 mV) is always detected with this operational mode, which accounts for the small peaks corresponding to the zinc isotopes. Conversely, if a point later in the profile is selected (e.g., ~ 58 minutes), as shown in Figure 8-13, the corresponding mass spectrum displays the nominal zinc isotopic pattern with minimal (if any) contribution from copper.

Multiple sample layers

The GD-TOFMS system was also capable of analyzing samples containing multiple thin layers, such as computer hard discs. Though hard disc information is proprietary, the layers comprising these discs can be identified. Figure 8-14 shows

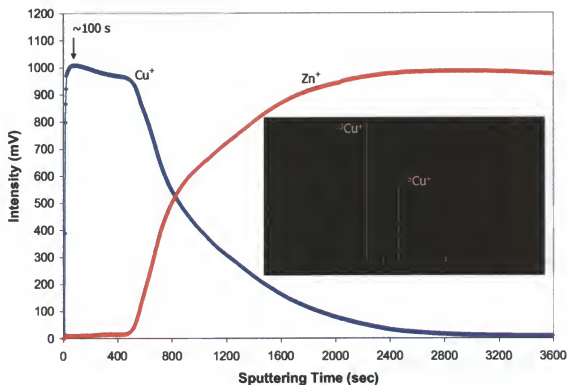


Figure 8-12. Intensity-time profile and mass spectrum corresponding to approximately 100 seconds of sputtering for a copper layer deposited onto a zinc substrate. Operating conditions: 2.0 kV, ~3.8 mA, 3.0 torr, 150 mL/min, 800 Hz pulse frequency, 30 ms pulse width, -1600 V detector voltage, and 3 s integration time.

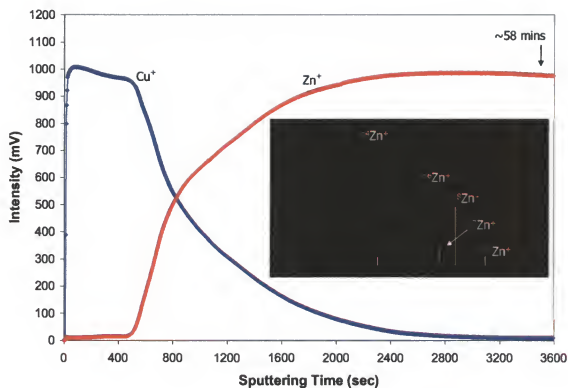


Figure 8-13. Intensity-time profile and mass spectrum corresponding to approximately 58 minutes of sputtering for a copper layer deposited onto a zinc substrate. Operating conditions as in Figure 8-12.

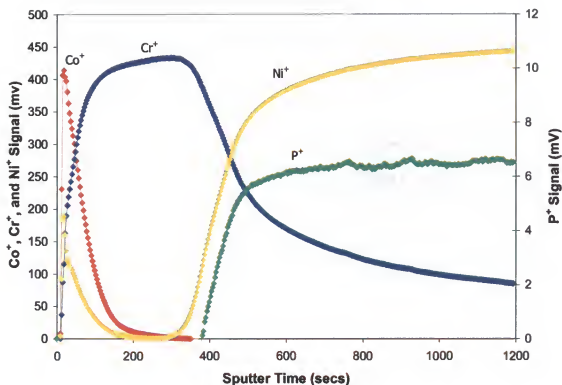


Figure 8-14. Intensity-time profile for a computer hard disc. Operating conditions: 2.0 kV, 3.4 mA, 3.5 torr, 200 mL/min, 800 Hz frequency, 20 μ s pulse width, -1600 V detector voltage, and 3 s integration time.

the multiple layers comprising a standard computer hard disc. It should be noted that the conditions used to analyze this hard disc were slightly different than those employed in the previously described thin gold layer analyses. The voltage, pressure, and pulse frequency were all increased to achieve an elevated sample removal rate since the layers comprising the hard disc were relatively thick (e.g., μm -regime) compared to the gold/silicon samples. Altering these parameters appeared to affect the depth resolution slightly, as shown by the chromium ion signal in Figure 8-14, which does not rapidly subside to background. Regardless, the data in Figure 8-14 reveals all of the expected elemental layers based on previous results in our laboratory.⁹⁰ This example also shows that our microsecond pulsed GD-TOFMS has the ability to analyze relatively thick, multiple layers given the proper operating conditions.

Additional Application

As mentioned in a previous section, depth profiling standards are not abundant, especially those suited for our microsecond pulsed GD. Therefore, alternative samples containing thin layers must be manufactured – or found. One type of sample that was surprisingly found to contain thin coatings was American pennies. For example, a 1982 penny was analyzed with our GD-TOFMS system, as shown in Figure 8-15. A large copper signal is obtained, which was not surprising based on the fact that these coins are often termed 'copper pennies'. The photo inset collected after sputtering also confirms that the penny is made of copper. Interestingly, pennies manufactured after 1982 are not true 'copper' pennies.

Instead, these pennies consist of a zinc substrate and a thin copper coating, as shown in Figure 8-16. Note the increasing zinc signal as the penny is sputtered and the white zinc substrate in the photo inset.

Concluding Remarks

Pulsed glow discharge time-of-flight mass spectrometry is shown to be an effective technique for depth profiling. Using a Grimm-type source instead of a direct insertion probe provides planar sputtering, which allows depth information to be probed. Operating conditions were established by merging established ion transport conditions, which were obtained previously using our GD-TOFMS, with operating parameters yielding good depth resolution for GD-AES measurements. Gold layers as thin as 8 nm deposited onto a silicon substrate were reproducibly analyzed with our system. Time-intensity profiles of thin gold films were successfully quantified and converted to information-rich concentration-depth profiles. Given the appropriate choice of operating conditions, the GD-TOFMS can be used to monitor thin layers as well as thick, multi-layered samples, such as computer hard discs.

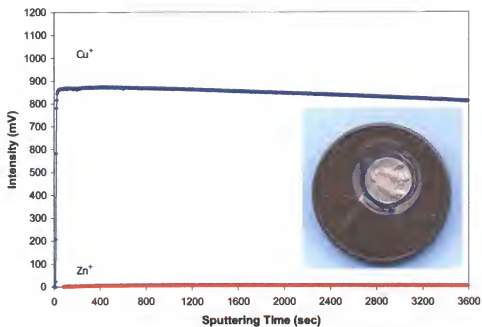


Figure 8-15. Intensity-time profile for a penny manufactured in 1982.

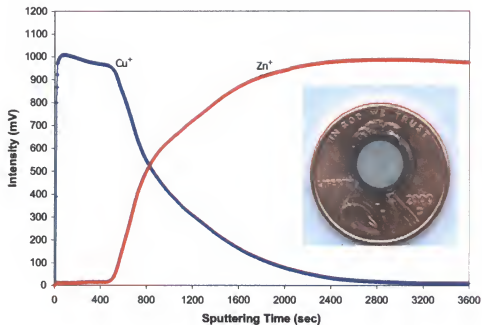


Figure 8-16. Intensity-time profile for a 'copper' penny manufactured in 2000.

CHAPTER 9 CONCLUDING REMARKS

This dissertation has focused on developments of the glow discharge (GD) source, encompassing fundamental studies and applications in atomic emission spectrometry (AES) and time-of-flight mass spectrometry (TOFMS). The GD is an electrical plasma long known for its ability to create atomic populations representative of solid samples; applying a transient pulse to this technique presents exciting new features and applications that can be evaluated. The projects presented in this dissertation are linked by one key facet – employment of a Grimm-type GD source configuration operated in the microsecond pulsed mode. While most of the projects in this dissertation are in the field of atomic mass spectrometry, one should not overlook the initial GD-AES study, which provided reason to implement the Grimm-type source in subsequent MS projects.

The first project was quantitative depth profiling of thin films using microsecond pulsed GD-AES. The pulsed GD provided precise control of the sample removal rate and the planar sputtering of the Grimm-type source stripped atomic layers in a linear fashion. Utilizing these advantages, thin films (~25 nm) were analyzed that otherwise prove difficult using a dc GD source. The protocol established allowed thin film profiling for determining the constituents and relative concentrations of elemental layers at varying depths within a sample. Examples

included analyzing paint coatings in the automobile industry and profiling defective computer hard discs to assess their faulty behavior.

After completing this atomic emission study, research efforts were shifted to MS studies with the microsecond pulsed GD source. A commercial inductively coupled plasma (ICP) TOFMS was converted to a GD-TOFMS system. A Grimm-type GD ion source was chosen, which has found limited use for mass spectrometric applications, despite its effectiveness as an atomic emission source. The sluggish development of the Grimm-source in the field of MS is attributed to ion transport concerns.

After evaluating the performance of the GD-TOFMS system, a study was undertaken to examine the ion transport efficiency between a Grimm-type source and TOFMS. Operating conditions and sampling configurations of the source were significant factors in controlling ion transfer. Proper selection of these parameters afforded transport efficiencies comparable to other GD-TOFMS source configurations (e.g., probe). In addition to circumventing ion transport difficulties, the success of this project provided the opportunity to explore future applications with our GD-TOFMS.

A marked limitation of the Grimm source is its lack of versatility – only flat samples that mount externally on the source can be analyzed. The analysis of samples with non-flat surfaces, such as pins and wires, typically requires a probe configuration. Accordingly, our next project was devising a method that would add versatility to our Grimm-type source. This was accomplished by developing a sample holder that mounts externally onto the Grimm-type source, allowing the

direct analysis of alternative sample types (e.g., pins). Easy sample interchange and reproducible sample placement - inherent advantages of the Grimm source - were not compromised with this sample holder.

The success of the previous GD-AES depth profiling project led us to evaluate the feasibility of analyzing thin films with our GD-TOFMS. Depth profiling has not been considered a practical application for GDMS. Convection effects can hinder the ability to measure ions originating from separate sample layers. The lack of Grimm-type source utilization in MS is another contributing factor. The analysis of thin films was realized by the foundations of previous projects. The established conditions yielding efficient ion transport for our GD-TOFMS (Chapter 6) were merged with conditions of our GD-AES that provided good depth resolution (Chapter 4). The depth profiling abilities of our MS system exceeded expectations by successfully analyzing layers less than 10 nm. The success of this project has shown that GDMS can adequately profile thin layer samples, given the proper source configuration and operating conditions.

The deceptive simplicity of the glow discharge should not be overlooked. Many fundamental studies and applications of this established technique have yet to be realized. Perusing the literature reveals that the current drive in GD research is finding ways to utilize this technique for probing molecular information. One noteworthy possibility is the desorption of molecular species by operating the GD at frequencies that approach a pulsed laser. One should not overlook the established niche of the GD though, as new elemental applications will inevitably emerge.

Regardless of the ultimate goal, glow discharges will continue to be a rich area of future endeavors.

REFERENCES

1. Aston, F.W. *Phil. Mag.*, **1919**, 38, 707.
2. Dempster, A.J. *Phys. Rev.*, **1918**, 11, 316.
3. *Rays of Positive Electricity and Their Application to Chemical Analyses*, Thomson, J.J., Longmans, Green and Co.: London, **1913**.
4. *Isotopes* 2nd Ed., Aston, F.W., Longmans, Green and Co.: New York, **1924**.
5. Solyom, D.A.; Hieftje, G.M. *J. Anal. Atom. Spectrom.*, **2002**, 17, 329.
6. *Quadrupole Mass Spectrometry and Its Applications*, Dawson, P.H., Elsevier Scientific: New York, **1976**.
7. Bruhn, C.G.; Bentz, B.L.; Harrison, W.W. *Anal. Chem.*, **1978**, 50, 373.
8. Yost, R.A.; Enke, C.G. *J. Amer. Chem. Soc.*, **1978**, 100, 2274.
9. McLuckey, S.A.; Goeringer, D.E.; Glish, G.L. *J. Am. Soc. Mass Spectrom.*, **1991**, 2, 11.
10. Duckworth, D.C.; Goeringer, D.E.; McLuckey, S.A. *J. Am. Soc. Mass Spectrom.*, **2000**, 11, 1072.
11. Shohet, J.L.; Phillips, W.L.; Lefkow, A.; Taylor, J.W.; Bonham, C.; Brenna, J.T. *Plasma Chem. and Plasma Proc.*, **1989**, 9, 207.
12. Barshick, C.M.; Eyler, J.R. *J. Am. Soc. Mass Spectrom.*, **1992**, 3, 122.
13. Hang, W.; Yang, P.Y.; Wang, X.R.; Yang, C.L.; Su, Y.X.; Huang, B.L. *Rapid Comm. Mass Spectrom.*, **1994**, 8, 590.
14. Harrison, W.W.; Hang, W. *J. Anal. Atom. Spectrom.*, **1996**, 11, 835.
15. Kadentsev, V.I.; Kaymarazov, A.G.; Chizhov, O.S.; Cerny, M.; Trnka, T.; Turecek, F. *Biomed. Mass Spectrom.*, **1982**, 9, 130.

16. Karas, M.; Bahr, U.; Hillenkamp, F. *Int. J. Mass Spectrom. Ion Processes*, **1989**, 92, 231.
17. Marcus, R.K., Introduction, in *Glow Discharge Spectroscopies*, Marcus R.K., Editor, Plenum Press: New York, **1993**, Chapter 1.
18. Douglas, D.J.; Houk, R.S. *Prog. Anal. Atom. Spectrom.*, **1985**, 8, 1.
19. McHugh, J.A., in *Methods of Surface Analysis*, Czanderna, A.W., Editor, Elsevier: Amsterdam, **1975**, Chapter 6.
20. Adams, F. *Spectrochim. Acta, Part B*, **1983**, 38B, 1379.
21. Fenner, N.C.; Daly, N.R. *Rev. Sci. Instrum.*, **1966**, 37, 1068.
22. Castle, B.C.; Visser, K.; Smith, B.W.; Winefordner, J.D. *Appl. Spectrosc.*, **1997**, 51, 1017.
23. Arrowsmith, P. *Anal. Chem.*, **1987**, 59, 1437.
24. Baker, S.A.; Dellavecchia, M.J.; Smith, B.W.; Winefordner, J.D. *Anal. Chim. Acta*, **1997**, 355, 113.
25. Browner, R.F.; Boom, A.W.; Smith, D.D. *Anal. Chem.*, **1982**, 54, 1411.
26. Hannay, N.B.; Ahearn, A.J. *Anal. Chem.*, **1954**, 26, 1056.
27. Harrison, W.W. *J. Anal. Atom. Spectrom.*, **1988**, 3, 867.
28. Coburn, J.W.; Kay, E. *Appl. Phys. Lett.*, **1971**, 18, 435.
29. Coburn, J.W.; Taglauer, E.; Kay, E. *J. Appl. Phys.*, **1974**, 45, 1779.
30. McNally, J.R.; Harrison, G.R.; Rowe, E. *J. Opt. Soc. Am.*, **1947**, 37, 93.
31. Birks, F.T. *Spectrochim. Acta*, **1956**, 8, 167.
32. Omenetto, N.; Smith, B.W.; Winefordner, J.D. *Spectrochim. Acta, Part B*, **1988**, 43B, 1111.
33. Gilmutdinov, A.K.; Chakrabarti, C.L.; Hutton, J.C.; Mrasov, R.M. *Surf. Interf. Anal.*, **1992**, 7, 1047.
34. Loving, J.T.; Harrison, W.W. *Anal. Chem.*, **1983**, 54, 1526.
35. Bengtson, A. *Spectrochim. Acta, Part B*, **1985**, 40B, 631.

36. Coburn, J.W.; Harrison, W.W. *Appl. Spectrosc. Rev.*, **1981**, 17, 95.
37. Yang, C.L.; Mohill, M.; Harrison, W.W. *J. Anal. Atom. Spectrom.*, **2000**, 15, 1255.
38. Harrison, W.W.; Yang, C.L.; Oxley, E.S. *Anal. Chem.*, **2001**, 73, 480A.
39. Bogaerts, A.; Okhrimovskyy, A.; Gijbels, R. *J. Anal. Atom. Spectrom.*, **2002**, March, On-line Edition.
40. Wagatsuma, K., Basic Principles of the Direct Current Discharge, in *Glow Discharge Optical Emission Spectrometry*, Payling R., Jones, D.G., Bengtson, A., Editors, John Wiley & Sons Ltd.: New York, **1997**, Chapter 4.
41. Broekaert, J.A.C. *J. Anal. Atom. Spectrom.*, **1987**, 2, 537.
42. Mahan, C.A. *J. Anal. Atom. Spectrom.*, **1997**, 12, 247.
43. Becker, J.S.; Dietze, H.J. *Int. J. Mass Spectrom.*, **2000**, 197, 1.
44. *Glow Discharge Processes: Sputtering and Plasma Etching*, Chapman, B.N., Wiley: New York, **1980**.
45. Rosenberg, D.; Wehner, G.K. *J. Appl. Phys.*, **1962**, 33, 1842.
46. *Atomic Energy Levels*, Moore, C.E., NBS Circular, **1941**, 467.
47. Fang, D.C.; Marcus, R.K., Fundamental Plasma Processes, in *Glow Discharge Spectroscopies*, Marcus R.K., Editor, Plenum Press: New York, **1993**, Chapter 2.
48. Hyman, H.A. *Phys. Rev. A*, **1979**, 20, 855.
49. Carman, R.J. *J. Phys. D*, **1989**, 22, 55.
50. Fang, D.C.; Marcus, R.K. *Spectrochim. Acta, Part B*, **1990**, 45B, 1053.
51. Fang, D.C.; Williams, R.R.; Marcus, R.K. *J. Anal. Atom. Spectrom.*, **1990**, 5, 569.
52. Bogaerts, A.; Gijbels, R. *Spectrochim. Acta, Part B*, **1998**, 53B, 1.
53. Bogaerts, A.; Gijbels, R. *Plasma Phys. Rep.*, **1998**, 24, 573.

54. Bogaerts, A.; Gijbels, R. *J. Anal. Atom. Spectrom.*, **1998**, 13, 945.
55. Bogaerts, A.; Gijbels, R. *Spectrochim. Acta, Part B*, **2001**, 56B, 551.
56. *Cold Cathode Discharge Tubes*, Weston, G.F., Iliffe: London, **1968**.
57. Schroerer, J.M.; Rhodin, T.N.; Bradley, R.C. *Surf. Sci.*, **1973**, 34, 571.
58. Stuart, R.V.; Wehner, G.K. *J. Appl. Phys.*, **1964**, 35, 1819.
59. Harrison, W.W.; Bruhn, C.G. *Anal. Chem.*, **1978**, 50, 16.
60. Oxley, E.; Yang, C.; Harrison, W.W. *J. Anal. Atom. Spectrom.*, **2000**, 15, 1241.
61. Boumans, P.W.J. *Anal. Chem.*, **1972**, 44, 1219.
62. Ingeneri, K. *Characterization of the Microsecond Pulsed Glow Discharge: A Novel Spectroscopic Source*, Ph.D. Dissertation, University of Florida, **2000**.
63. Smith, R.L.; Serxner, D.; Hess, K.R. *Anal. Chem.*, **1989**, 61, 1103.
64. Steers, E.B.M.; Fielding, R.J. *J. Anal. Atom. Spectrom.*, **1987**, 2, 239.
65. Steers, E.B.M.; Leis, F. *J. Anal. Atom. Spectrom.*, **1989**, 4, 199.
66. Vriens, L. *Phys. Lett.*, **1964**, 8, 260.
67. Hess, K.R.; Harrison, W.W. *Anal. Chem.*, **1988**, 60, 691.
68. Smyth, K.C.; Bentz, B.L.; Bruhn, C.G.; Harrison, W.W. *J. Amer. Chem. Soc.*, **1979**, 101, 797.
69. Eckstein, E.W.; Coburn, J.W.; Kay, E. *Int. J. Mass Spectrom. Ion Phys.*, **1975**, 17, 129.
70. Vieth, W.; Huneke, J.C. *Spectrochim. Acta, Part B*, **1991**, 46B, 137.
71. King, F.L.; Harrison, W.W., *Glow Discharge Mass Spectrometry*, in *Glow Discharge Spectroscopies*, Marcus R.K., Editor, Plenum Press: New York, **1993**, Chapter 5.
72. Schuler, H.; Gollnow, H. *Z. Phys.*, **1935**, 93, 611.

73. *Inorganic Mass Spectrometry*, Harrison, W.W.; Adams, F.; Gijbels, R.; Van Grieken, R., Editors, Wiley: New York, **1988**.
74. Mandelstam, S.L.; Nedler, V.V. *Spectrochim. Acta, Part B*, **1961**, *17*, 885.
75. Harrison, W.W.; Yang, C.L.; Oxley, E.S., The Mass Spectrometry of Glow Discharges, in *Glow Discharge Plasmas in Analytical Spectroscopy*, Marcus, R.K.; Broekaert, J.A.C., Editors, John Wiley & Sons Ltd.: New York, In press.
76. Yang C.L.; Harrison W.W. *Spectrochim. Acta, Part B*, **2001**, *56B*, 1195.
77. Mattson, W.A.; Bentz, B.L.; Harrison W.W. *Anal. Chem.*, **1976**, *48*, 489.
78. Harrison, W.W.; Barshick, C.M.; Klingler, J.A.; Ratliff, P.H.; Mei, Y. *Anal. Chem.*, **1990**, *62*, 943A.
79. VG 9000 Product Literature, TJA Solutions, Franklin, Massachusetts, USA.
80. Grimm, W. *Spectrochim. Acta, Part B.*, **1968**, *23B*, 443.
81. Broekaert, J.A.C., Atomic Emission Spectrometry, in *Glow Discharge Spectroscopies*, Marcus R.K., Editor, Plenum Press: New York, **1993**, Chapter 4.
82. Bengtson, A.; Yang, C.L.; Harrison, W.W. *J. Anal. Atom. Spectrom.*, **2000**, *15*, 1279.
83. Yang, C.L.; Ingeneri, K.; Harrison, W.W. *J. Anal. Atom. Spectrom.*, **1999**, *14*, 693.
84. Bogaerts, A; Gijbels, R. *J. Anal. Atom. Spectrom.*, **1998**, *13*, 721.
85. Wagatsuma, K.; Suzuki, S. *Fresenius J. Anal. Chem.* **1997**, *358*, 581.
86. Payling, R., An Overview of GD-OES, in *Glow Discharge Optical Emission Spectrometry*, Payling, R., Jones, D.G., Bengtson, A., Editors, John Wiley & Sons Ltd.: New York, **1997**, Chapter 1.
87. Bengtson, A.; Danielsson, L. *Thin Solid Films*, **1985**, *124*, 231.
88. Wetzig, K.; Baunack, S.; Hoffmann, V.; Oswald, S.; Prassler, F. *Fresenius J. Anal. Chem.* **1997**, *358*, 25.

89. Yang, C.L.; Ingeneri, K.; Mohill, M.; Harrison, W.W. *Anal. Chem.*, **1999**, *71*, 5328.
90. Yang, C.L.; Ingeneri, K.; Mohill, M.; Harrison, W.W. *J. Anal. Atom. Spectrom.*, **2000**, *15*, 73.
91. Bogaerts, A.; Wagner, E.; Smith, B.W.; Winefordner, J.D.; Pollman, D.; Harrison, W.W.; Gijbels, R. *Spectrochim. Acta, Part B*, **1998**, *52B*, 205.
92. Bogaerts, A.; Gijbels, R. *Fresenius J. Anal. Chem.*, **1996**, *355*, 853.
93. Bogaerts, A.; Gijbels, R.; Goedheer, W.J. *Anal. Chem.*, **1996**, *68*, 2296.
94. Bogaerts, A.; Guenard, R.D.; Smith, B.W.; Winefordner, J.D.; Harrison, W.W.; Gijbels, R. *Spectrochim. Acta, Part B*, **1997**, *52B*, 219.
95. Dogan, M.; Laqua, K.; Massmann, H. *Spectrochim. Acta, Part B*, **1972**, *27B*, 65.
96. Milton, D.M.P.; Hutton, R.C. *Spectrochim. Acta*, **1993**, *48B*, 39.
97. Wehner, G.K. *J. Appl. Phys.*, **1955**, *26*, 1056.
98. Winchester, M.R.; Duckworth, D.C.; Marcus, R.K., Analysis of Nonconducting Sample Types, in *Glow Discharge Spectroscopies*, Marcus R.K., Editor, Plenum Press: New York, **1993**, Chapter 7.
99. Harrison, W.W.; Hang, W. *Fresenius J. Anal. Chem.*, **1996**, *355*, 803.
100. Piepmeier, E.H.; de Galan, L. *Spectrochim. Acta, Part B*, **1975**, *30B*, 263.
101. Harrison, W.W.; Mattson, W.A. *Proc. of 23rd ASMS Conf. on Mass Spectrom. And Allied Topics*, Houston, Texas, **1975**, N11.
102. Lewis, C.L.; Oxley, E.S.; Pan, C.K.; Steiner, R.E.; King, F.L. *Anal. Chem.*, **1999**, *71*, 230.
103. Steiner, R.E.; Lewis, C.L.; Majidi, V. *J. Anal. Atom. Spectrom.*, **1999**, *14*, 1537.
104. Harrison, W.W. *J. Anal. Atom. Spectrom.*, **1998**, *13*, 1051.
105. Yan, X.; Hang, W.; Smith, B.W.; Winefordner, J.D.; Harrison, W.W. *J. Anal. Atom. Spectrom.*, **1998**, *13*, 1033.

106. Walden, W.O.; Harrison, W.W.; Smith, B.W.; Winefordner, J.D. *J. Anal. Atom. Spectrom.*, **1994**, 9, 1039.
107. Belle, C.J.; Johnson, J.D. *Appl. Spectrosc.*, **1973**, 27, 118.
108. Payling, R.; Jones, D.G.; Gover, S.A. *Surf. Interf. Anal.*, **1993**, 20, 959.
109. Prassler, F.; Hoffmann, V.; Schumann, J.; Wetzig, K. *J. Anal. Atom. Spectrom.*, **1995**, 10, 677.
110. Jakubowski, N; Stuewer, D. *J. Anal. Atom. Spectrom.*, **1992**, 7, 951
111. Quentmeier, A. *J. Anal. Atom. Spectrom.*, **1994**, 9, 355.
112. Raith, A.; Hutton, R.C.; Huneke, J.C. *J. Anal. Atom. Spectrom.*, **1993**, 8, 867.
113. Rose, E.; Mayr, P. *Mikrochim. Acta*, **1989**, 1, 197.
114. Parker, M.; Hartenstein, M.L.; Marcus, R.K. *Anal. Chem.*, **1996**, 68, 4213.
115. Bengtson, A. *Spectrochim. Acta, Part B*, **1994**, 49B, 411.
116. Takadoum, J.; Pivin, J.C.; Ponscorbeau, J.; Berneron, R.; Charbonnier, J.C. *Surf. Interf. Anal.*, **1984**, 6, 174.
117. Ponscorbeau, J.; Cazet, J.P.; Moreau, J.P.; Berneron, R.; Charbonnier, J.C. *Surf. Interf. Anal.*, **1986**, 9, 21.
118. Harrison, W.W.; Magee, C.W. *Anal. Chem.*, **1974**, 46, 461.
119. Hang, W.; Baker, C.; Smith, B.W.; Winefordner, J.D.; Harrison, W.W. *J. Anal. Atom. Spectrom.*, **1997**, 12, 143.
120. Myers, D.P.; Hieftje, G.M. *Microchem. J.*, **1993**, 48, 259.
121. Myers, D.P.; Li, G.; Yang, P.; Hieftje, G.M. *J. Am. Soc. Mass Spectrom.*, **1994**, 5, 1008.
122. *Time-of-Flight Mass Spectrometry: Instrumentation and Applications in Biological Research*, Cotter, R.J., American Chemical Society: Washington, DC, **1997**.
123. Tian, X.D.; Ernteborg, H.; Adams, F.C. *J. Anal. Atom. Spectrom.*, **1999**, 14, 1807.

124. Myers, D.P.; Ray, S.J.; Hieftje, G.M., Inorganic Time-of-Flight Mass Spectrometry, in *Inorganic Mass Spectrometry: Fundamentals and Applications*, Barshick, C.M.; Duckworth, D.C.; Smith, D.H., Editors, Marcel Dekker: New York, **2000**, Chapter 12.
125. Mamyrin, B.A.; Shmikk, D.V. *Zhurnal Eksperimentalnoi Teoreticheskoi Fiziki*, **1979**, 76, 1500.
126. *Spectrochemical Analysis*, Ingle, J.D., Crouch, S.R., Editors, Prentice Hall: New Jersey, **1988**, Chapter 6.
127. Guilhaus, M. *J. Mass Spectrom.*, **1995**, 30, 1519.
128. *CRC Handbook of Chemistry and Physics 76th Ed.*, Lide, D.R., Editor, CRC Press: Boca Raton, **1995**.
129. *Spectrochemical Analysis*, Ingle, J.D., Crouch, S.R., Editors, Prentice Hall: New Jersey, **1988**, Chapter 5.
130. Ferreira, N.P.; Human, H.G.C. *Spectromchim. Acta*, **1981**, 36B, 215.
131. Van Straaten, M.; Vertes, A.; Gijbels, R. *Spectrochim. Acta*, **1991**, 46B, 283.
132. Van Straaten, M.; Gijbels, R. *Anal. Chem.*, **1992**, 64, 1855.
133. Hang, W.; Harrison, W.W. *Anal. Chem.*, **1997**, 69, 4957.
134. Harrison, W. W.; Hess, K. R.; Marcus, R. K.; King, F. L. *Anal. Chem.* **1986**, 58, 341A.
135. Majidi, V.; Moser, M.; Lewis, C.; Hang, W.; King, F.L. *J. Anal. Atom. Spectrom.* **1999**, 15, 19.
136. *LECO SA-2000 Quick Reference Training Guide*, LECO Corporation, **2001**, 62.
137. Steiner, R.E.; Lewis, C.L.; King, F.L. *Anal. Chem.*, **1997**, 69, 1715.
138. Heintz, M. J.; Myers, D. P.; Mahoney, P. P.; Li, G. Q.; Hieftje, G. M. *Appl. Spectrosc.*, **1995**, 49, 945.
139. Bogaerts, A; Gijbels, R. *J. Anal. Atom. Spectrom.*, **2001**, 16, 239.

140. Jackson, G.P.; Lewis, C.L.; Doorn, S.K.; Majidi, V.; King, F.L. *Spectrochim. Acta, Part B*, **2001**, 56B, 2449.
141. Harrison, W.W.; Hang, W.; Yan, M.; Ingeneri, K.; Schilling, C. *J. Anal. Atom. Spectrom.*, **1997**, 12, 891.
142. King, F.L.; McCormack, A.L.; Harrison, W.W. *J. Anal. Atom. Spectrom.*, **1988**, 3, 883.
143. Jakubowski, N.; Stuewer, D.; Vieth, W. *Anal. Chem.* **1987**, 59, 1825.
144. Jakubowski, N.; Stuewer, D.; Toelg, G. *Int. J. Mass Spectrom. Ion Proc.*, **1986**, 71, 183.
145. Su, Y.X.; Yang, P.Y.; Zhou, Z.; Wang, X.R.; Li, F.M.; Huang, B.L.; Ren, J.S.; Chen, M.; Ma, H.B.; Zhang, G.S. *Spectrochim. Acta, Part B*, **1998**, 53, 1413.
146. Hall, D.J.; Sanderson, N.E. *Surf. Interf. Anal.*, **1988**, 11, 40.
147. Kay, E. *Abstr. Pap. Amer. Chem. Soc.*, **1976**, 89.
148. Coburn, J.W. *Abstr. Pap. Amer. Chem. Soc.*, **1974**, 92.

BIOGRAPHICAL SKETCH

Eric Oxley was born in Teays Valley, West Virginia, on January, 18, 1976. Ironically, he was born during Super Bowl X, which may give insight into his passion for sports - especially football. Eric grew up in a small town of Milton, West Virginia, where he attended school - from Milton Elementary all the way through Milton High School. After graduating from high school, Eric ventured away from home and became a Mountaineer by attending West Virginia University, in Morgantown, WV. In May, 1998, he received a Bachelor of Science degree in chemistry and accepted a summer internship position at Eastman Chemical, in Kingsport, Tennessee. Eric affirms that this enjoyable, but challenging, industrial experience gave him the desire to pursue an analytical research and development position. After the internship, he continued his education in chemistry as part of the analytical chemistry division of the graduate program at the University of Florida, in Gainesville, FL. For the past four years, he has greatly enjoyed working under the tutelage of Professor W.W. Harrison. In July, 2002, Eric obtained the degree of Doctor of Philosophy. Eric has achieved his career goal by accepting a research and development position at LECO Corporation in St. Joseph, Michigan.

I certify that I have read this study and that in my opinion it conforms to acceptable standards of scholarly presentation and is fully adequate, in scope and quality, as a dissertation for the degree of Doctor of Philosophy.



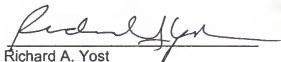
Willard W. Harrison, Chair
Professor of Chemistry & Dean
Emeritus

I certify that I have read this study and that in my opinion it conforms to acceptable standards of scholarly presentation and is fully adequate, in scope and quality, as a dissertation for the degree of Doctor of Philosophy.



James D. Winefordner
Graduate Research Professor of
Chemistry

I certify that I have read this study and that in my opinion it conforms to acceptable standards of scholarly presentation and is fully adequate, in scope and quality, as a dissertation for the degree of Doctor of Philosophy.



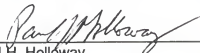
Richard A. Yost
Professor of Chemistry

I certify that I have read this study and that in my opinion it conforms to acceptable standards of scholarly presentation and is fully adequate, in scope and quality, as a dissertation for the degree of Doctor of Philosophy.



Martin T. Vala
Professor of Chemistry

I certify that I have read this study and that in my opinion it conforms to acceptable standards of scholarly presentation and is fully adequate, in scope and quality, as a dissertation for the degree of Doctor of Philosophy.



Paul H. Holloway
Professor of Materials Science and
Engineering

This dissertation was submitted to the Graduate Faculty of the Department of Chemistry in the College of Liberal Arts and Sciences and to the Graduate School and was accepted as partial fulfillment of the requirements for the degree of Doctor of Philosophy.

August 2002

Dean, Graduate School